

# Alignment of molecules induced by long and short laser pulses

PhD thesis

Mikael D. Poulsen

April, 2005

Department of Chemistry  
University of Aarhus, Denmark



# Publications

Most of the work presented in this thesis<sup>1</sup> is (or will be) published in:

- [1] M. D. Poulsen, E. Skovsen, and H. Stapelfeldt  
*Photodissociation of laser aligned iodobenzene: Towards selective photoexcitation*  
J. Chem. Phys., **117** (2002), 2097–2102
  
- [2] E. Péronne, M. D. Poulsen, C. Z. Bisgaard, H. Stapelfeldt, and T. Seideman  
*Nonadiabatic Alignment of Asymmetric Top Molecules: Field-Free Alignment of Iodobenzene*  
Phys. Rev. Lett. **91** (2003), 043003
  
- [3] E. Péronne, M. D. Poulsen, C. Z. Bisgaard, H. Stapelfeldt, E. Hamilton, and T. Seideman  
*Nonadiabatic alignment of iodobenzene*  
Phys. Rev. A **70** (2004), 063410

---

<sup>1</sup>Except for the results presented in sect. 4.5.2 and sect. 6.4

- 
- [4] C. Z. Bisgaard, M. D. Poulsen, E. Péronne, S. S. Viftrup, and H. Stapelfeldt  
*Observation of Enhanced Field-Free Molecular Alignment by Two Laser Pulses*  
Phys. Rev. Lett. **92** (2004), 173004
- [5] M. D. Poulsen, E. Péronne, H. Stapelfeldt, C. Z. Bisgaard, S. S. Viftrup, E. Hamilton, and T. Seideman  
*Nonadiabatic alignment of asymmetric top molecules: Rotational revivals*  
J. Chem. Phys. **121** (2004), 783–791
- [6] T. Ejdrup, M. D. Poulsen, C. Z. Bisgaard, S. S. Viftrup, H. Stapelfeldt, E. Hamilton, and T. Seideman  
*Laser induced alignment of symmetric top molecules*  
Manuscript in preparation
- [7] M. D. Poulsen, T. Ejdrup, H. Stapelfeldt, E. Hamilton, and T. Seideman  
*Alignment of molecules by a long and a short laser pulse*  
Manuscript in preparation

# Contents

|   |           |
|---|-----------|
| <b>Preface</b>  | <b>ix</b> |
| <b>Outline</b>  | <b>xi</b> |
| <b>1 Introduction</b>   | <b>1</b>  |
| 1.1 Why control molecular orientation? . . . . .              | 1         |
| 1.2 Methods to control molecular orientation . . . . .        | 3         |
| 1.2.1 Orientation and alignment by electric field . . . . .   | 4         |
| 1.2.2 Collision induced alignment . . . . .                   | 10        |
| 1.3 Advantages and disadvantages of laser induced alignment . | 11        |
| <b>2 Theory of alignment</b>                                  | <b>13</b> |
| 2.1 Definition of Alignment . . . . .                         | 13        |
| 2.1.1 Molecular coordinates . . . . .                         | 13        |
| 2.1.2 Linear alignment . . . . .                              | 15        |
| 2.1.3 3-D alignment . . . . .                                 | 17        |
| 2.2 Quantum Mechanical theory of alignment . . . . .          | 18        |
| 2.2.1 Angular dependence of the interaction . . . . .         | 19        |
| 2.2.2 Time dependence of the interaction . . . . .            | 22        |
| 2.2.3 Methods of calculation . . . . .                        | 26        |

---

|          |   |           |
|----------|---|-----------|
| 2.3      | Classical theories of alignment . . . . .                                 | 28        |
| 2.3.1    | Boltzmann distribution . . . . .  | 28        |
| 2.3.2    | Classical kicked rotor . . . . .  | 30        |
| <b>3</b> | <b>Experimental Setup</b>   | <b>31</b> |
| 3.1      | The molecular beam . . . . .  | 32        |
| 3.1.1    | Gas flow system . . . . .   | 32        |
| 3.1.2    | Vacuum chambers . . . . .   | 34        |
| 3.2      | Laser pulses . . . . .  | 35        |
| 3.2.1    | Alignment and probe pulses . . . . .                                      | 35        |
| 3.2.2    | Optical setup . . . . .   | 37        |
| 3.3      | Data acquisition and treatment . . . . .                                  | 42        |
| 3.3.1    | Ion imaging . . . . .   | 42        |
| 3.3.2    | Abel inversion . . . . .  | 44        |
| <b>4</b> | <b>Adiabatic alignment of iodobenzene</b>                                 | <b>48</b> |
| 4.1      | Idea . . . . .  | 49        |
| 4.2      | Resonantly enhanced multi photon ionization of iodine . . .               | 51        |
| 4.3      | Photodissociation of iodobenzene . . . . .                                | 52        |
| 4.3.1    | The $n \rightarrow \sigma^*$ dissociation channel . . . . .               | 53        |
| 4.3.2    | The $\pi \rightarrow \pi^*$ dissociation channel . . . . .                | 55        |
| 4.3.3    | Promptness of the dissociation . . . . .                                  | 55        |
| 4.4      | Linear alignment . . . . .  | 56        |
| 4.4.1    | Ion images . . . . .  | 56        |
| 4.4.2    | Kinetic energy distributions . . . . .                                    | 58        |
| 4.4.3    | Angular distributions . . . . .   | 59        |
| 4.4.4    | Obtaining $f_{mol}(\theta)$ and $\langle \cos^2 \theta \rangle$ . . . . . | 61        |
| 4.4.5    | Assumptions made for obtaining $\langle \cos^2 \theta \rangle$ . . . . .  | 63        |
| 4.5      | Controlling the photodissociation . . . . .                               | 66        |

---

|          |  |           |
|----------|--|-----------|
| 4.5.1    | Control using linear Alignment . . . . .                 | 66        |
| 4.5.2    | Improving the control with 3-D alignment . . . . .       | 69        |
| 4.6      | Conclusion . . . . .                                     | 71        |
| <b>5</b> | <b>Non-adiabatic alignment – short time dynamics</b>     | <b>73</b> |
| 5.1      | Alignment with one pulse . . . . .                       | 75        |
| 5.1.1    | Experiment . . . . .                                     | 75        |
| 5.1.2    | Ion images and $\langle \cos^2 \theta \rangle$ . . . . . | 77        |
| 5.1.3    | Dependence on intensity and rotational temperature       | 79        |
| 5.1.4    | Alignment pulse duration . . . . .                       | 82        |
| 5.2      | Alignment with two pulses . . . . .                      | 86        |
| 5.2.1    | Idea . . . . .   | 86        |
| 5.2.2    | Experiment . . . . .                                     | 87        |
| 5.2.3    | Alignment dynamics . . . . .                             | 87        |
| 5.2.4    | Pulse to pulse delay . . . . .                           | 90        |
| 5.2.5    | Intensity ratio, $I_1/I_2$ . . . . .                     | 91        |
| 5.2.6    | Discussion . . . . .                                     | 91        |
| 5.3      | Conclusion . . . . .                                     | 92        |
| <b>6</b> | <b>Non-adiabatic alignment – Rotational revivals</b>     | <b>94</b> |
| 6.1      | Experiment . . . . .                                     | 96        |
| 6.2      | Symmetric top molecules . . . . .                        | 97        |
| 6.2.1    | Ion images . . . . .                                     | 97        |
| 6.2.2    | Revival spectra . . . . .                                | 98        |
| 6.2.3    | Duration of the alignment pulse . . . . .                | 105       |
| 6.3      | Asymmetric top molecules of $C_{2v}$ type . . . . .      | 108       |
| 6.3.1    | Revival spectra . . . . .                                | 108       |
| 6.3.2    | Molecular asymmetry . . . . .                            | 113       |
| 6.4      | Asymmetric top molecules of general type . . . . .       | 116       |

---

|          |   |            |
|----------|---|------------|
| 6.4.1    | Angle of detection . . . . .                                | 117        |
| 6.4.2    | Ion images . . . . .  | 119        |
| 6.4.3    | Revival spectra . . . . .                                   | 120        |
| 6.5      | Conclusion . . . . .  | 124        |
| <b>7</b> | <b>Combining adiabatic and non-adiabatic alignment</b>      | <b>126</b> |
| 7.1      | Coulomb explosion probe . . . . .                           | 126        |
| 7.2      | Experiment . . . . .  | 128        |
| 7.3      | Comparing adiabatic and non-adiabatic alignment . . . . .   | 129        |
| 7.3.1    | Ion images . . . . .  | 129        |
| 7.3.2    | $\langle \cos^2 \theta_{2D} \rangle$ measurements . . . . . | 130        |
| 7.4      | Combining adiabatic and non-adiabatic alignment . . . . .   | 132        |
| 7.4.1    | Short time dynamics . . . . .                               | 132        |
| 7.4.2    | Rotational revivals . . . . .                               | 136        |
| 7.5      | Conclusion . . . . .  | 136        |
| <b>8</b> | <b>Outlook</b>  | <b>138</b> |
| 8.1      | Experimental improvements . . . . .                         | 139        |
| 8.1.1    | New pulsed valve . . . . .                                  | 139        |
| 8.1.2    | Velocity mapping using slice imaging . . . . .              | 139        |
| 8.1.3    | Crossed laser beams . . . . .                               | 141        |
| 8.1.4    | Programmable pulse shaper . . . . .                         | 141        |
| 8.2      | New experiments . . . . .                                   | 142        |
| 8.2.1    | Improving alignment . . . . .                               | 142        |
| 8.2.2    | Combining alignment and orientation . . . . .               | 143        |
| 8.2.3    | Applications of alignment . . . . .                         | 145        |
| 8.2.4    | Alignment in the liquid phase . . . . .                     | 146        |
| 8.3      | Final words . . . . .                                       | 147        |

---

|          |   |            |
|----------|---|------------|
| <b>A</b> | <b>Molecular data</b>                                       | <b>149</b> |
| A.1      | Symmetric top molecules . . . . .                           | 150        |
| A.2      | Asymmetric top molecules of $C_{2v}$ -type . . . . .        | 151        |
| A.3      | Asymmetric top molecules of general type . . . . .          | 152        |
| <b>B</b> | <b>Laser beam parameters</b>                                | <b>153</b> |
| <b>C</b> | <b>Dissociation probabilities of iodobenzene</b>            | <b>157</b> |
| C.1      | Dissociation probability and the Beer-Lambert law . . . . . | 157        |
| C.2      | Angular dependence of the dissociation . . . . .            | 159        |
| C.2.1    | The $n \rightarrow \sigma^*$ channel . . . . .              | 160        |
| C.2.2    | The $\pi \rightarrow \pi^*$ channel . . . . .               | 161        |
|          | <b>Summary</b>  | <b>163</b> |
|          | <b>Bibliography</b>   | <b>166</b> |

# Preface

This thesis is submitted to the Faculty of Science at the University of Aarhus, in order to fulfill the requirements for the PhD degree. The work presented in the thesis has been carried out in the years 2000–2004 in the Femtogroup at the Department of Chemistry under the supervision of Henrik Stapelfeldt.

## Acknowledgements

That my five years in the femtogroup have been such an exciting experience is largely due to the excellent people I have had the pleasure of working with. In my first experimental work I benefited greatly from collaboration with Esben Skovsen, together with whom I enjoyed many cups of coffee and hard rock working in the lab. Later I had a very fruitful teamwork with Emmanuel Péronne. We were joined in our efforts by Christer Z. Bisgaard and Simon Viftrup. Together we have shared many late hours of data acquisition and big boxes of candy. Recently I have also had the pleasure of working with Tine Ejdrup.

I also need to thank Jan Thøgersen for his invaluable help whenever the lasers behaved strangely. The mechanics workshop at the Department of Chemistry and Per Strand in particular have always been very helpful

designing ingenious technical solutions. Credits are also due to Jeppe Olsen and Tina D. Poulsen for helping me getting started with the polarizability calculations.

Our collaborators abroad Tamar Seideman and Edward Hamilton are gratefully acknowledged for many fruitful and enlightening discussions. I am very grateful to Christer Z. Bisgaard for proofreading the entire manuscript and giving numerous insightful comments. I am also very grateful to Tina D. Poulsen for improving my scientific English and correcting my grammar.

I am deeply grateful to my supervisor Henrik Stapelfeldt, who has constantly helped and guided me through my years as a Ph.D. student. He is definitely a very recommendable supervisor.

Finally but definitely not the least I need to thank my children, Sara and Rasmus, for the unmeasurable joy they bring and my wife, Malene, for her constant love, patience, support, and a gentle push when needed.

# Outline

## **Chapter 1: Introduction**

In the first chapter, I will motivate our work and explain why control of molecular motion is important. To bring our work into a broader context, other methods of controlling molecular rotation are briefly reviewed and compared to our method, laser induced alignment.

## **Chapter 2: Theory**

In this chapter the molecular coordinates and the different types of alignment are defined. The quantum mechanical theory of alignment and two classical theories applying to special cases are presented.

## **Chapter 3: Experimental Setup**

This chapter gives a description of the experimental apparatus used in our experiments.

## **Chapter 4: Adiabatic alignment of iodobenzene – control of the photo dissociation**

In this chapter the photo dissociation of iodobenzene is explained in detail and our method for obtaining the  $\langle \cos^2 \theta \rangle$  measure of alignment is described.

Our results on adiabatic (long pulse) alignment and the use of alignment to control the photo dissociation are presented.

**Chapter 5: Non-adiabatic alignment – post pulse behavior**

This chapter deals with the short time alignment dynamics of iodobenzene molecules subject to one or two short non-adiabatic alignment pulses. The presented results show how the alignment depends on the rotational temperature of the molecules and the intensity and duration of the alignment pulse. Enhanced alignment obtained by using two rather than one alignment pulse is demonstrated.

**Chapter 6: Non-adiabatic alignment – rotational revivals**

This chapter is concerned with the alignment dynamics induced by a short non-adiabatic alignment pulse on a longer timescale. Rotational revival spectra are presented for both symmetric and asymmetric top molecules.

**Chapter 7: Combining adiabatic and non-adiabatic alignment**

In this chapter the alignment obtained with a long (adiabatic) pulse is compared to the alignment obtained with a short (non-adiabatic) pulse. It is shown that by combining adiabatic and non-adiabatic pulses the induced alignment is enhanced beyond the alignment obtained with either pulse alone.

**Chapter 8: Outlook**

This last chapter is concerned with our future research in the field of laser induced alignment.

## Appendices

*Appendix A: Molecular data* lists relevant data for the molecules studied in the experiments.

*Appendix B: Laser beam parameters* describes how the various laser beam parameters are defined and how we measure them.

*Appendix C: Dissociation probabilities of iodobenzene* presents the mathematical derivation of the expressions for the dissociation probabilities of iodobenzene used in chapter 4.



# Chapter 1

## Introduction

### 1.1 Why control molecular orientation?

Controlling the orientation of molecules in space has been a long standing goal in spectroscopy as well as in chemistry in general.

The crucial role of molecular orientation in chemistry is readily understood by looking at a basic chemical reaction such as the  $S_N2$  reaction<sup>1</sup>[8] between  $\text{OH}^-$  and  $\text{CH}_3\text{Br}$  shown in fig. 1.1. When separated by long distances the reagent molecules are two separate entities (fig. 1.1 a). However, if the molecules come close enough they might start to react and form a transition state (fig. 1.1 b). From the transition state the reaction can proceed to form the product molecules, in this case  $\text{CH}_3\text{OH}$  and  $\text{Br}^-$  (fig. 1.1 c).

From the example shown in fig. 1.1 it is evident that for a chemical reaction to occur, the distance between the molecules must be small enough. Besides distance the relative orientation of the reagent molecules is also crucial for the probability that a transition state is formed. In the example,

---

<sup>1</sup> $S_N2$  stands for nucleophilic substitution reaction of 2nd order

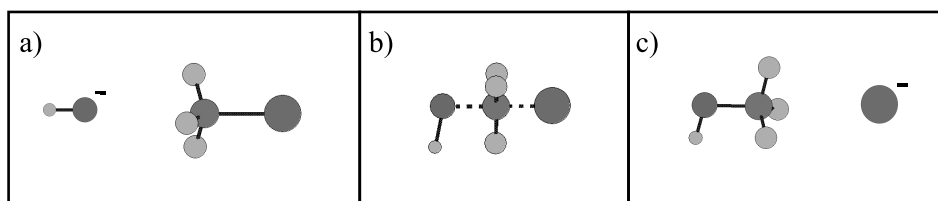


Figure 1.1: The chemical reaction between  $\text{OH}^-$  and  $\text{CH}_3\text{Br}$  forming  $\text{CH}_3\text{OH}$  and  $\text{Br}^-$ . a) The reagent molecules, b) transition state, c) product molecules.

$\text{OH}^-$  must approach  $\text{CH}_3\text{Br}$  with the O atom first and react opposite the Br atom. This dependence on the relative orientation is not restricted to  $\text{S}_{\text{N}}2$  reactions but is a general feature of almost all chemical reactions.<sup>2</sup> In many cases the relative orientation also determines which transition state is formed and thus which chemical reaction will occur.

Replacing one of the two reagent molecules in the chemical reaction with one or more photons, the reaction becomes photochemistry or spectroscopy. In this case the relative orientation of the reagents, ie. the polarization of the photon(s) relative to the orientation of the molecule is also important. The probability of the different processes that can occur: absorption, Raman-scattering, multi-photon ionization, etc. all depend on the relative orientation of molecule and photon polarization.

Different types of absorptions may depend differently on the molecular orientation, as for example parallel and perpendicular electronic transitions in a linear molecule. A means to control molecular orientation can thus be used to favor one absorption channel against another. If the absorption leads to bond breakage, it is called a photochemical reaction, the control of molecular orientation is therefore a means to control photochemical re-

<sup>2</sup>The only exception is the combination of two atomic species to form a diatomic molecule

actions.

For many spectroscopic methods a uniform distribution of molecules blurs or hides information about the molecular structure that would be obtainable if the molecules had a specific orientation in space. An example is photo electron spectroscopy. The trajectories of electrons ejected from a molecule reveal information about the structure of the molecular orbitals. However, if the molecules are uniformly distributed, orientational averaging conceals the effect.

## 1.2 Methods to control molecular orientation

There are many ways to control the (translational) motion and orientation (rotational motion) of molecules.

One obvious way to control molecular motion is to crystallize the sample thereby severely confining both the translational and rotational degrees of freedom. Using x-ray diffraction the fixed molecular orientation in a crystal can be used to gain information about the molecular structure, a technique known as crystallography.

If the goal is control of bimolecular chemical reactions such as the one shown in fig. 1.1 the most applicable method to control molecular motion is attachment to a surface. Besides fixing the translational motion attachment to a surface usually causes all the molecules to have the same specific orientation relative to the surface. The surface may be a metal catalyst, a polymer or a boundary between two liquid phases.

Crystallization or surface attachment drastically change the spectroscopic properties of molecules. For spectroscopy one often wish a molecule to remain free of external perturbations while controlling the orientation. To put our work on laser induced alignment of molecules into a broader con-

text, I will briefly review the related methods of controlling the rotational motion of free molecules. The orientation of free molecules can be controlled either through an applied external field or through collision induced alignment.

### 1.2.1 Orientation and alignment by electric field

The most common method of controlling the orientation of free molecules is to use an external electric<sup>3</sup> field. An applied electrical field interacts with the dipole or induced dipole moments of the molecule.

The effect of an external electric field on molecules with a permanent dipole moment is illustrated in fig. 1.2. The applied field induces a torque on the polar molecules (fig. 1.2 a). If the induced torque is large enough to overcome the rotational energy of the molecules, the molecules are oriented along the direction of the electric field (fig. 1.2 b). An applied field can also affect molecules without a permanent dipole moment. If the field is strong enough it induces a dipole moment in the molecules and cause the induced dipoles to align along the field direction. In this case there is no up-down selection, only confinement of a molecular axis, and we use the term *alignment* instead of *orientation* (fig. 1.2 c).

The external electric field can be supplied either from electrodes with an applied DC or AC voltage or from a laser pulse. It is also possible to combine the two. The methods using charged electrodes include brute force orientation, hexapole focusing, and AC electrokinetics. The methods using laser fields include resonant and nonresonant laser induced alignment and optical spanner and tweezers.

---

<sup>3</sup>In principle a magnetic field could also be used. Magnetic forces are however for most molecules far too weak to be useful in practice

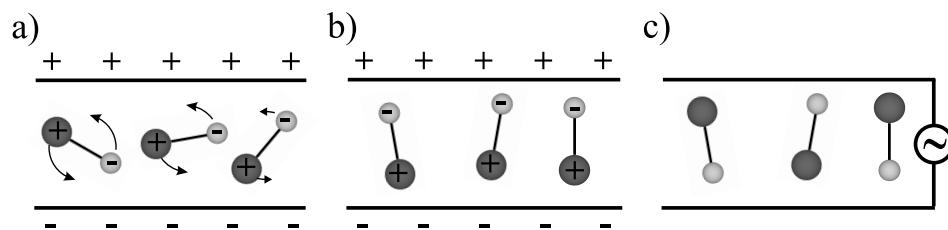


Figure 1.2: a) Molecules with a permanent dipole moment placed in an external field will experience a torque. b) The torque causes the molecules to orient according to the field. c) Molecules can also be aligned via an induced dipole moment created by the applied field, in this case there is no up-down selectivity

### Brute force orientation

“Brute force orientation” experiments utilize a pair of highly charged capacitor plates with a narrow spacing between them[9]. The electric fields affects molecules with permanent dipole moments as illustrated in fig. 1.2. Typical field strengths are 10-20 MV/m and the generated fields are too weak to align via an induced molecular dipole moment. If the interaction between the permanent dipole moment and the static field is strong enough to overcome the rotational motion, the molecules will orient along the direction of the electric field. To obtain significant orientation at the relatively modest field strengths available, the molecules have to be cooled to a rotational temperature of a few Kelvin. Therefore a supersonic expansion is used to create a beam of cold gas phase molecules[10], which is directed between the capacitor plates. The important parameters for obtaining well oriented molecules are: Low rotational temperature, high electric field strength and high molecular dipole moment.

The degree of orientation achieved in brute force experiments is relatively weak. Kong and coworkers calculated that for ICN molecules rota-

tionally cooled to 1.5 K subject to an orientation field of 5 MV/m 84% will “point the right way”, be within  $90^\circ$  of the field axis and 40% will be within  $45^\circ$  of the field axis[11] (for a uniform molecular distribution 15% is within  $45^\circ$  of a given axis)

Kong and coworkers used brute force orientation to find the direction of transition dipoles by polarization spectroscopy[12, 13]. Molecules were dissociated by a laser pulse polarized either parallel or perpendicular to the external field. The ratio of the photoproduct yields with parallel and perpendicular polarizations (the polarization ratio) was measured. The polarization ratio can be translated to an angle between permanent dipole and transition dipole given that the distribution of molecular orientations is known.

### Hexapole focusing

Besides creating a uniform linear electric field between two capacitor plates other electrode configurations resulting in inhomogeneous electric fields are also useful for orientation. One common configuration is the hexapole, which consists of six circular rods placed in a hexagon and charged with voltages that alternate in sign (see fig. 1.3).

Hexapole focusing is applicable to symmetric tops, asymmetric tops with a dipole moment along the A or C axis, linear polyatomic molecules excited in bending vibrations, and diatomics with electronic angular momentum[14].

A molecular beam originating from a supersonic expansion is travelling down the center of the hexapole. Some of the molecules will follow the centerline closely (fig 1.3 i). These molecules are usually blocked. Molecules which initially diverge from the centerline with a small angle are affected by the inhomogeneous field. Symmetric top molecules with  $KM < 0$  are attracted towards the centerline. The “half wavelength” of the trajectories

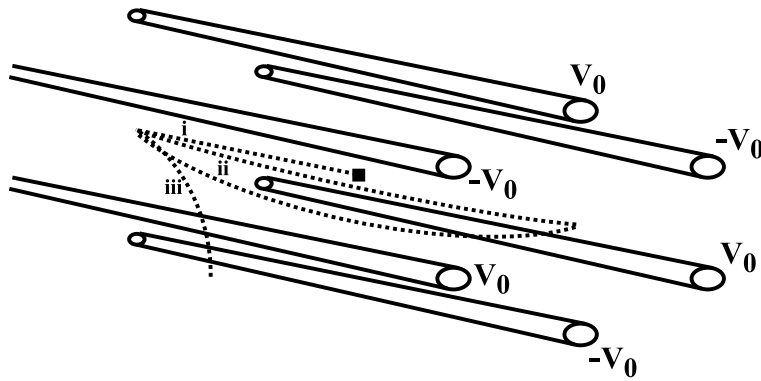


Figure 1.3: Hexapole focusing of symmetric top molecules. The molecular beam travels in the electric field generated by six rods charged with voltages of alternating sign. i: Molecules travelling in the center of the hexapole are blocked. ii: Molecules in same rotational state with  $KM < 0$  initially diverging from the center axis follow trajectories with the same “half wavelength”. iii: Molecules with  $KM > 0$  are ejected out of the hexapole.

depend on the rotational state. Molecules in the same rotational state will focus at the same spot (fig. 1.3 ii) independent of their initial angle of divergence provided they have the same translational speed. Symmetric top molecules with  $KM > 0$  are ejected out of the hexapole (fig. 1.3 iii). Since different rotational states focus at different positions down the centerline a hexapole can be used to select a single rotational state, given that the number of different states is low, i.e. the rotational temperature is low.

Apart from selection of single rotational states hexapoles are also used for orientating molecules. The state selection is due to different rotational states having different orientation of the permanent dipole relative to the electric field. Therefore a hexapole focuses molecules with the same orientation at the same position along the center axis.

An example of the use of hexapole orientation is the work of Harland and Brooks[15], in which they bombarded hexapole orientated  $\text{CF}_3\text{Br}$  molecules with alkali metal atoms to study the orientational dependence of the electron transfer from the atoms to  $\text{CF}_3\text{Br}$ .

### AC electrokinetics

If the subject of interest is macromolecules or micrometer particles in solution rather than single gas phase molecules, AC fields are normally used. In a DC field any net charge of the molecule or particle will attract the subject to one electrode (electrophoretic force)[16]. A common method for aligning and stretching macromolecules or particles is to use an inhomogeneous field created by an array of electrodes with an applied AC voltage, a technique known as dielectrophoresis. The AC field interacts with the polarizability of the subject to create an induced dipole which is aligned in the electric field. Since the polarizability for micrometer sized objects is much larger than for single gas phase molecules the interaction can be strong enough to produce a significant effect even for field strengths on the order of 0.1–1 MV/m.

Dielectrophoresis has been used to stretch DNA molecules to  $\sim 15 \mu\text{m}$  ( $\sim 70\%$  of their full elongated length)[17]. The DNA molecules were attached at one end to an array of  $20 \mu\text{m}$  gold electrodes and an AC electric field of 0.2–0.8 MV/m with a frequency of 100–1000 kHz was applied. At lower frequencies electrophoretic forces cause fluid flow and electrothermal reactions. At higher frequencies the reorientation of the induced dipole on the DNA starts lagging behind the switch in the electric field since the magnitude of the induced dipole moment for the very non-rigid DNA molecules depend on nuclear displacement along a vast number of internal coordinates. Weaker fields are not sufficient to overcome the thermal randomization and stronger fields cause electrophoretic forces to dominate.

### Laser induced alignment

Electrode generated electric fields rarely exceeds 20 MV/m[9]. The electrical field strength at the focus of a pulsed laser can however be much higher – a moderately high laser intensity of  $10^{12}$  W/cm<sup>2</sup> corresponds to a field strength of 3 GV/m. The oscillatory nature of the laser field prevents molecules from orienting via their permanent dipole moment but if the field is non-resonant with absorptions in the molecules, the field aligns the molecules through an induced dipole moment. Since non-resonant laser induced alignment is the subject of the rest of this thesis I will not elaborate further here but move on to the case where the laser field *is* resonant with absorption.

Transition dipole moments depend on the orientation of the molecule with respect to the polarization of the exciting pulse. Therefore, absorption of polarized light generates an anisotropy in the distribution of orientations both in the initial (ground) state and the excited state of the molecule. The alignment obtained through a resonant transition is weak compared to the alignment achievable through non-resonant alignment.

If the alignment is induced by a short laser pulse, both resonant and non-resonant alignment can be used for time-resolved rotational spectroscopy. This type of spectroscopy, known as Rotational Coherence Spectroscopy (RCS)[18, 19], is discussed in chapter 6.

Alignment can also be induced in a liquid. Since a liquid cannot be cooled below the freezing point and stay liquid, rotational temperatures are high and alignment effects correspondingly weak. The induced alignment is however strong enough to induce a measurable birefringence of the liquid, known as the optical Kerr effect[20]. The decay rates of the induced birefringence contain information about the molecular dynamics of the solution or pure liquid. Time resolved optical Kerr effect studies are useful

for testing the validity of models for solvent-solute interactions[21, 22].

### **Optical tweezers and optical spanner**

When the subject of interest is macromolecules the laser analogs to dielectrophoresis are the optical tweezers and the optical spanner described below.

In the case of the optical tweezers the inhomogeneous electric field of a focused laser beam creates a gradient force towards the center of the focus. A small object such as a polystyrene bead will therefore follow a slowly moving laser focus, thereby the name: optical tweezers. By attaching a bead to one end of a protein, the motion and stretching of the protein can be studied by moving the laser focus[23, 24].

Circularly polarized light can make small objects (such as a 2  $\mu\text{m}$  Teflon particle) rotate due to the spin angular momentum of the photons, this is known as the “optical spanner”. Changing the laser mode from the usual plane wave front to a helical ‘corkscrew-shaped’ wave front creates orbital angular momentum, which can add to or cancel the spin-angular momentum, causing the objects to rotate faster or stop rotating[25].

Whereas the optical tweezers are a widely used tool for studying cellular biology the optical spanner has so far only been sparsely used. A search on the Web of Science yields 739 hits on “optical tweezers” and only seven hits on “optical spanner”.

### **1.2.2 Collision induced alignment**

Supersonic expansion of a gas into vacuum through a narrow nozzle is very useful as a source of translationally and rotationally cold molecules. Besides a general lowering of the rotational temperature a supersonic ex-

### **1.3 Advantages and disadvantages of laser induced alignment 11**

---

pansion sometimes also causes molecular alignment. In 1974, Zare and coworkers[26] showed experimentally that  $\text{Na}_2$  molecules emerging from a supersonic expansion preferred rotation about an axis perpendicular to the beam axis, corresponding to alignment of the molecular bond axis along the beam direction. Other molecules have also been observed to exhibit collision induced alignment. Pirani et. al[27] showed that planar molecules such as benzene prefer to travel as a frisbee, ie. with the molecular plane parallel to the beam axis.

### **1.3 Advantages and disadvantages of laser induced alignment**

Before moving on to discuss the theoretical and experimental details of our experiments. I will briefly address the advantages and disadvantages of laser induced alignment of gas-phase molecules compared to the other methods of orientation and alignment of free molecules presented.

As stated in the previous section the alignment induced by non-resonant laser pulse is stronger than alignment induced by a resonant pulse. Collision induced alignment is usually only observed to a significant degree in the very center of the molecular beam, which means that severe skimming of the beam must be done, resulting in loss of sample. Even with severe skimming the observed degrees of alignment are much weaker than what is obtainable through laser induced alignment.

Non-resonant laser induced alignment is a very general method applicable to all molecules, except spherical tops. Unlike brute force orientation and hexapole focusing no permanent dipole moment is required. Furthermore, the confinement of molecular axes achievable with laser induced alignment is much narrower than what can be achieved through brute force

orientation or hexapole focusing.

There are some problems extending laser induced alignment to really big molecules. As mentioned in the previous section the induced dipole moment of DNA molecules starts lagging behind the oscillations of the field when the frequency exceeds  $\sim 1$  GHz. Therefore the near-infrared wavelengths used in this thesis are not suitable for alignment of very big non-rigid molecules.

Unlike static fields laser induced alignment does not distinguish between ‘heads’ and ‘tails’ of the molecules, therefore some authors claim that “alignment experiments miss the main steric effect”[14]. However, when the aligned molecules are subject to some kind of polarized light pulse of few or more optical cycles, the oscillatory nature of the light will average out any “heads vs. tails” orientation – this is the case in most spectroscopic applications, such as the polarization experiments by Kong and coworkers[12]. These experiments could just as well have been performed on aligned rather than oriented molecules, in fact the narrower confinement available in alignment experiments would result in higher polarization ratios. Apart from special cases such as nonlinear processes due to half cycle pulses, the situations in which “heads vs. tails” orientation are important, are bimolecular reactions such as the example of electron transfer between  $\text{CF}_3\text{Br}$  and alkali atoms.

In conclusion non-resonant laser induced alignment is the preferable method whenever a narrow confinement of molecular axes is wanted without the need of “heads vs. tails” orientation. In this thesis laser induced alignment is demonstrated using either a long (adiabatic) pulse, one or two short (non-adiabatic) pulses, or a long and short pulse combined.

## Chapter 2

# Theory of alignment

### 2.1 Definition of Alignment

Alignment is the confinement of one or more molecular axes to laboratory fixed axes. The situation is illustrated in fig. 2.1 for iodobenzene molecules. Confinement of one molecular axis is called linear or 1-D alignment (fig. 2.1 b). If two axes of a rigid molecule are confined, the third axis is necessarily also confined, this is known as 3-D alignment (fig. 2.1 c).

#### 2.1.1 Molecular coordinates

To be more quantitative than the pictorial presentation of fig. 2.1 it is necessary to define which molecular axes are confined and how well. For that molecular coordinates and the transformation to laboratory fixed coordinates must be introduced.

As explained in sect. 2.2 laser induced alignment is due to an interaction with the polarizability of the molecule. The molecule fixed coordinate system is therefore defined so that the polarizability tensor is diagonal,

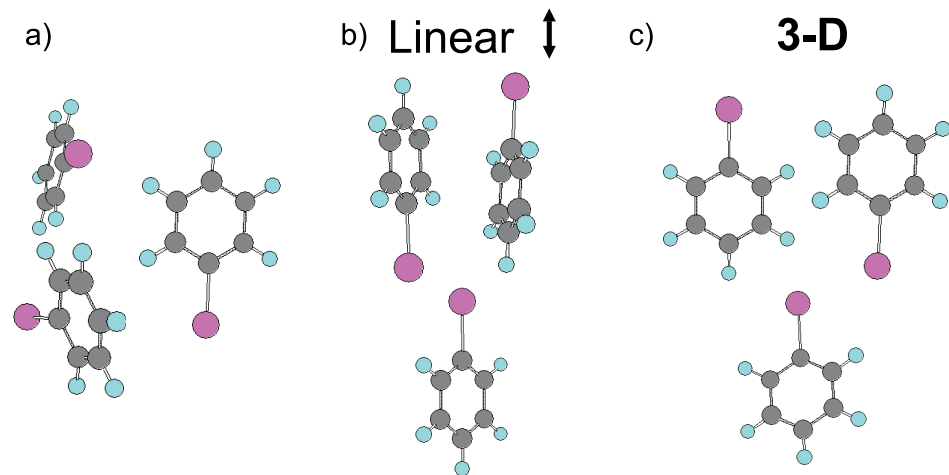


Figure 2.1: Alignment of iodobenzene molecules. a) Uniform distribution. b) Linear alignment: The C–I bond axis is confined to the vertical axis, the molecular plane is free to rotate. c) 3-D alignment: The molecule is confined in all three dimensions.

$$\alpha_{mol} = \begin{pmatrix} \alpha_{xx} & 0 & 0 \\ 0 & \alpha_{yy} & 0 \\ 0 & 0 & \alpha_{zz} \end{pmatrix} . \quad (2.1)$$

For linear and symmetric top molecules the symmetry axis is the molecule fixed z-axis. For asymmetric top molecules the major axis of polarizability is the z-axis. Transformation from molecule fixed  $(x,y,z)$  to laboratory fixed  $(X,Y,Z)$  coordinates can be done with the unitary Euler angle transformation matrix[28],  $\Phi$ ,

$$\begin{pmatrix} X \\ Y \\ Z \end{pmatrix} = \Phi^{-1} \begin{pmatrix} x \\ y \\ z \end{pmatrix} \quad \Phi^{-1} = \Phi^T \quad (2.2)$$

$$\Phi(\theta, \phi, \chi) = \begin{pmatrix} c\phi c\theta c\chi - s\phi s\chi & s\phi c\theta c\chi + c\phi s\chi & -s\theta c\chi \\ -c\phi c\theta s\chi - s\phi c\chi & -s\phi c\theta s\chi + c\phi c\chi & s\theta s\chi \\ c\phi s\theta & s\phi s\theta & c\theta \end{pmatrix}.$$

In eq.2.2 cos and sin are abbreviated to c and s respectively. The definition of the  $(\theta, \phi, \chi)$  Euler angles is illustrated in fig. 2.2.  $\theta \in [0, \pi)$  is the angle between the molecule fixed z-axis and the space fixed Z-axis,  $\phi \in [0, 2\pi)$  is the angle of rotation of the z-axis around the Z-axis and  $\chi \in [0, 2\pi)$  is the angle of rotation of the molecule around the z-axis.

The distribution of orientations,  $f_{mol}$ , of a non-linear molecule is in general a function of all three Euler angles. The  $\chi$  angle has no meaning for linear molecules. For a uniform distribution of all angles,  $f_{mol}(\theta, \phi, \chi) = \frac{1}{8\pi^2}$  (for a linear molecule  $f_{mol}(\theta, \phi) = \frac{1}{4\pi}$ ). The distribution of a given angle is obtained by integrating over the other angles,

$$f_{mol}(\theta) = \int_0^{2\pi} \int_0^{2\pi} f_{mol}(\theta, \phi, \chi) d\chi d\phi. \quad (2.3)$$

### 2.1.2 Linear alignment

In the case of linear or 1-D alignment the molecule fixed z-axis is confined near the laboratory fixed Z-axis, which is equivalent to a localization in the  $\theta$ -angle close to 0 and  $\pi$ . A commonly used measurement of the degree of linear alignment is the average value of  $\cos^2 \theta$  [29],  $\langle \cos^2 \theta \rangle$ , defined as

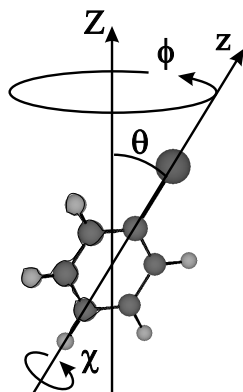


Figure 2.2: Euler angles illustrated with an iodobenzene molecule.  $\theta$  is the angle between the molecule fixed  $z$ -axis and the space fixed  $Z$ -axis,  $\phi$  is the angle of rotation of the  $z$ -axis around the  $Z$ -axis, and  $\chi$  is the angle of rotation around the  $z$ -axis.

$$\langle \cos^2 \theta \rangle = \int_0^\pi \cos^2 \theta f_{mol}(\theta) \sin \theta d\theta. \quad (2.4)$$

A uniform distribution has  $\langle \cos^2 \theta \rangle = \frac{1}{3}$ . A distribution of aligned molecules has  $\langle \cos^2 \theta \rangle > \frac{1}{3}$ .  $\langle \cos^2 \theta \rangle < \frac{1}{3}$  is referred to as “planar delocalization” [30] or “anti-alignment” [31], the latter is in a way a misnomer since the molecules are still aligned, as the molecular  $z$ -axis is now confined to the lab-fixed  $(X, Y)$ -plane.

The  $\langle \cos^2 \theta \rangle$  measure is used throughout this thesis but it is by no means the only way to measure linear alignment. Other measures such as the average value of  $\cos \theta$  to any even order or the percentage of molecule within a cone of a given angle could also be used. The molecular distribution in the  $\theta$ -angle,  $f_{mol}(\theta)$ , is not uniquely defined by  $\langle \cos^2 \theta \rangle$ . Two different angular

distributions may have the same  $\langle \cos^2 \theta \rangle$  as illustrated for two distributions of aligned  $I_2$  molecules in table. 2.1. Which molecular distribution is deemed most aligned thus depend on which measurement is chosen.

| Rotational temp.<br>Intensity   | $T_{rot} = 1.4$ K<br>$I_0 = 2 \times 10^{11}$ W/cm <sup>2</sup> | $T_{rot} = 4$ K<br>$I_0 = 5 \times 10^{11}$ W/cm <sup>2</sup> | Uniform<br>distribution |
|---------------------------------|---|---|-------------------------|
| $\langle \cos^2 \theta \rangle$ | 0.75  | 0.75  | 1/3                     |
| Within 15° cone                 | 25.1%   | 28.7%   | 3.4%                    |
| Within 30° cone                 | 63.6%   | 63.4%   | 13.4%                   |
| Within 60° cone                 | 94.0%   | 93.2%   | 1/2                     |

Table 2.1: Calculated molecular distribution of  $I_2$  molecules subject to adiabatic alignment.

### 2.1.3 3-D alignment

In the case of 3-D alignment all three principal axis of the molecule are confined in space. Therefore both  $f_{mol}(\theta)$ ,  $f_{mol}(\phi)$ , and  $f_{mol}(\chi)$  are localized. So far there is only a few papers concerned with 3-D alignment[32, 33], and there is no commonly used measure as for linear alignment. For planar molecules one obvious choice would be to use  $\langle \cos^2 \theta \rangle$  as a measure of the confinement of the major axis and measure the alignment of the molecular plane as  $\langle \cos^2 \gamma \rangle$ , with  $\gamma$  being the angle between the vector  $\vec{n}$  perpendicular to the plane (eq. C.6) and the laboratory fixed X-axis. This measure is used in [33].

## 2.2 Quantum Mechanical theory of alignment

An external electric field changes the environment of a molecule. Expanding the energy in a power series of the electric field the Hamiltonian becomes[34]

$$H = H_0 - \vec{\mu} \cdot \vec{E} - \frac{1}{2} \vec{E} \alpha \vec{E} + \dots \quad , \quad (2.5)$$

where  $H_0$  is the field free Hamiltonian,  $\vec{E}$  is the electric field vector,  $\vec{\mu}$  is the permanent dipole moment, and  $\alpha$  is the polarizability tensor. The interaction between the field and permanent dipole moment is the term  $-\vec{\mu} \cdot \vec{E}$  in eq. 2.5. The interaction between field and induced dipole moment is  $-\frac{1}{2} \vec{\mu}_{ind} \cdot \vec{E} = -\frac{1}{2} \vec{E} \alpha \vec{E}$ .

If an electric field of a laser pulse with a duration longer than a few optical cycles ( $\tau_{pulse} \gg \nu$ ) is considered, averaging over the optical period will quench interaction with the permanent dipole moment and higher moments that interact with odd orders of  $E$ . Assuming a linear polarized field and averaging over an optical period  $\vec{E} \alpha \vec{E}$  can be replaced by  $\frac{1}{2} \bar{\varepsilon}(t) \alpha \bar{\varepsilon}(t)$ , where  $\bar{\varepsilon}(t)$  is the pulse envelope. Higher order (4th,6th,...) interactions are negligible at field strengths below the onset of multi photon ionization. The interaction with the laser field can thus be written as

$$H_{int} = -\frac{1}{4} \bar{\varepsilon}(t) \Phi^{-1} \alpha_{mol} \Phi \bar{\varepsilon}(t). \quad (2.6)$$

In eq. 2.6, the polarizability tensor in laboratory fixed coordinates,  $\alpha$ , has been replaced by its diagonal expression in molecular coordinates,  $\alpha_{mol}$ , (eq. 2.1). The  $\Phi$ -matrix (eq. 2.2) transforms from laboratory to molecule fixed coordinates.

### 2.2.1 Angular dependence of the interaction

It is the angular dependence of the interaction between field and polarizability that is the cause of alignment.

For a linearly polarized laser field it is customary to choose the laboratory fixed Z-axis as the field axis,  $\vec{\varepsilon}(t) = \varepsilon(t)(0, 0, 1)$ . Depending on the symmetry of the molecule different expressions for  $H_{int}$  are obtained from eq. 2.6, see table 2.2.

| Molecular symmetry              | Eigenfunctions $\phi$                          | $H_{int} =$  | Conditions for $\langle \phi_2   H_{int}   \phi_1 \rangle \neq 0$ <sup>1</sup>   |
|---------------------------------|--|--|--|
| Linear                          | $  JM \rangle$                                 | $-\frac{1}{4}\varepsilon^2((\alpha_{\parallel} - \alpha_{\perp}) \cos^2 \theta + \alpha_{\perp})$            | $\Delta M = 0, \Delta J = 0, \pm 2$  |
| Symmetric top                   | $  JKM \rangle$                                | $\alpha_{\parallel} = \alpha_{zz}, \alpha_{\perp} = \alpha_{xx} = \alpha_{yy}$                               | $\Delta M = 0, \Delta K = 0$<br>$\Delta J = 0, \pm 1^2, \pm 2$                   |
| Asymmetric top of $C_{2v}$ type | $  J\tau M \rangle = \sum_K c_K   JKM \rangle$ | $-\frac{1}{4}\varepsilon^2(\alpha^{zx} \cos^2 \theta + \alpha^{yx} \sin^2 \theta \sin^2 \chi + \alpha_{xx})$ | $\Delta M = 0,$<br>$\Delta K = 0, \pm 2$<br>$\Delta J = 0, \pm 1, \pm 2^3$       |
| General asymmetric top          |  | $\alpha^{zx} = \alpha_{zz} - \alpha_{xx}$<br>$\alpha^{yx} = \alpha_{yy} - \alpha_{xx}$                       | $\Delta M = 0$<br>$\Delta K = 0, \pm 1, \pm 2$<br>$\Delta J = 0, \pm 1, \pm 2^3$ |

Table 2.2:  $H_{int}$  and selection rules for a linear polarized field.

Note that the projection of the angular momentum on the laboratory fixed Z-axis, the M quantum number, is always conserved.

#### Linear molecules

For linear molecules  $\alpha_{\parallel} > \alpha_{\perp}$ . From table 2.2 it is seen that the energy is minimized at  $\theta = 0$  and  $\theta = \pi$ . The effect of the field is thus a torque on the molecules towards  $\theta = 0$  and  $\theta = \pi$ , causing alignment.

<sup>1</sup>Selection rules for a rotational Raman transition. See [3, 33]

<sup>2</sup>If  $K \neq 0$ .

<sup>3</sup>In the basis of symmetric top eigenstates

### Symmetric top molecules

Since  $H_{int}$  is the same as for linear molecules, prolate symmetric top molecules ( $\alpha_{\parallel} > \alpha_{\perp}$ ) will align like linear molecules. For oblate symmetric top molecules ( $\alpha_{\parallel} < \alpha_{\perp}$ ) in a linear field, the energy is minimized at  $\theta = \frac{\pi}{2}$ , which means that the symmetry axis is confined to the plane perpendicular to the field axis. Oblate symmetric top molecules are thus not effectively aligned in a linear field (the symmetry axis is only confined to a plane and not to an axis). Using two perpendicular linear polarized fields or a circular polarized field the symmetry axis of an oblate symmetric top is aligned towards the third axis (the beam axis of a circular polarized beam), since the energy is minimized when the symmetry axis is perpendicular to both field axes.

The circular symmetry of the polarizability means that 3-D alignment is not possible for symmetric tops.

### Asymmetric top molecules

The angular confinement achieved for asymmetric top molecules subject to linear or elliptical fields are illustrated in fig. 2.3, which shows a calculation of  $f_{mol}$  of aligned 3,4-dibromothiophene molecules.

For asymmetric top molecules subject to a linear field the energy is minimized at  $\theta = 0$  and  $\theta = \pi$ , which means the major axis of polarizability, the z-axis, aligns along the field axis.  $H_{int}$  also depends on the  $\chi$ -angle. This  $\chi$ -angle dependence causes molecules that are not perfectly aligned in the  $\theta$ -angle to rotate to minimize the angle between the second principal axis of polarizability and the field axis corresponding to a localization in the  $\chi$ -angle (fig. 2.3 LP). For iodobenzene molecules, this means that the axis perpendicular to the plane is localized perpendicular to the alignment

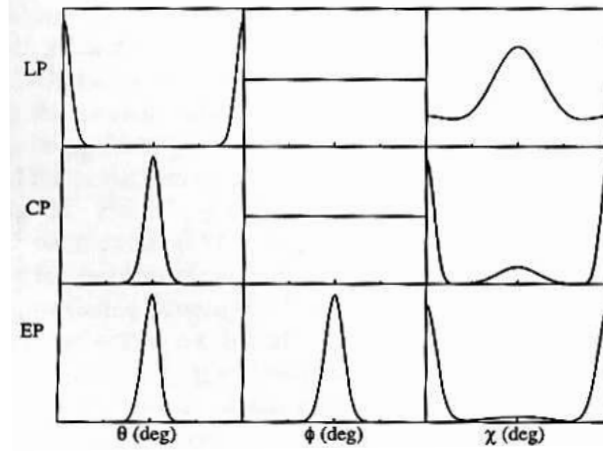


Figure 2.3:  $f_{mol}(\theta)$ ,  $f_{mol}(\phi)$ , and  $f_{mol}(\chi)$  of 3,4-dibromo thiophene subject to an alignment field with linear (LP), circular (CP), or elliptical (EP) polarization. Reprinted from [32].

field axis.

If the alignment field has circular polarization the minor axis of polarizability will align along the laser beam axis as for oblate symmetric tops. In this case there will also be a localization in the  $\chi$ -angle (fig. 2.3 CP).

If the alignment field has elliptical polarization[32], or consist of two perpendicular linear fields[33], 3-D alignment of asymmetric top molecules can be achieved. Averaging over an optical period, the interaction with the laser field can be expressed as

$$H_{int} = -\frac{1}{4} \left( \vec{\varepsilon}_X(t) \Phi^{-1} \alpha_{mol} \Phi \vec{\varepsilon}_X(t) + \vec{\varepsilon}_Y(t) \Phi^{-1} \alpha_{mol} \Phi \vec{\varepsilon}_Y(t) \right), \quad (2.7)$$

where  $\vec{\varepsilon}_X(t)$  and  $\vec{\varepsilon}_Y(t)$  are the field envelope along the X and Y coordinates respectively.

The energy is minimized when the major axis of polarizability is aligned

along the major axis of the field and the minor axis of polarizability is aligned perpendicular to the field, corresponding to a confinement of all three Euler angles (fig. 2.3 EP).

### 2.2.2 Time dependence of the interaction

Since  $\alpha_{mol}$  is constant for rigid molecules the time dependence of  $H_{int}$  is determined by the time dependence of  $\varepsilon(t)$ . If  $\varepsilon(t)$  is varying slowly compared to molecular rotation, i.e. the pulse duration of the alignment pulse is longer than the rotational period of the molecules, the field can be treated as constant in time. This is the *adiabatic* alignment regime. The other situation, in which the alignment pulse duration is shorter than the rotational period of the molecules is the *non-adiabatic* alignment regime. Non-adiabatic alignment can also result from fast truncation of a slow (adiabatic) pulse[35, 36].

#### Adiabatic alignment

The word adiabatic in this context means that each field-free eigenstate progress to an eigenstate of the field-on Hamiltonian:  $H_0+H_{int}$ . Upon adiabatic (i.e. slow) field turn-off each molecule returns to its original field free eigenstate[37].

A calculation of adiabatic alignment of  $I_2$  molecules is shown in fig. 2.4. The initial uniform distribution has  $\langle \cos^2 \theta \rangle = 1/3$ . The degree of alignment follows the shape of the alignment pulse and peaks at the peak of the alignment pulse. When the alignment pulse is over the original uniform distribution is recreated.

From fig. 2.4 it is clear that a low rotational temperature corresponds to a high degree of alignment. The obtained degree of alignment is obviously

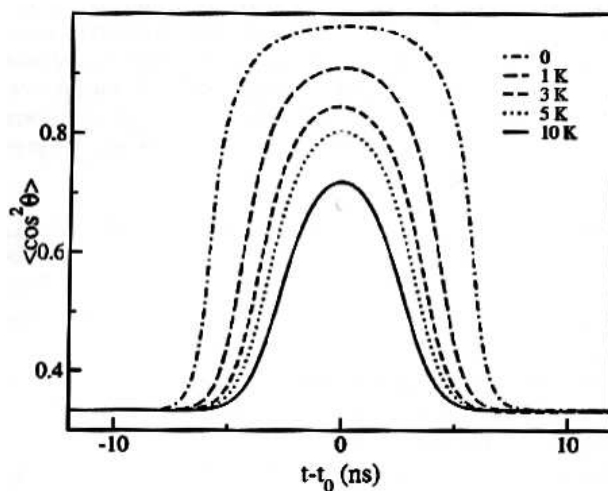


Figure 2.4: Calculation of adiabatic alignment of  $I_2$  molecules resulting from a linear polarized pulse peaking at  $t = t_0$  with a duration of 3.5 ns. The different curves correspond to different rotational temperatures. Reprinted from [38].

also dependent on the intensity of the alignment pulse – a higher intensity corresponds to a higher degree of alignment. The limit to the intensity is the onset of multi photon ionization. The third parameter that determines how well the molecules align is the anisotropy of the molecular polarizability.

### Non-adiabatic alignment

Non-adiabatic alignment can be viewed as a sequence of rotational Raman transitions (illustrated for a linear molecule in fig. 2.5). Each Raman cycle is limited by the selection rules of a pure rotational Raman transition (table 2.2 for linear fields). In a typical alignment experiment the molecules undergo 10–100 cycles and the resulting wave packet can be very broad[3].

Unlike the adiabatic case the induced non-adiabatic alignment does not

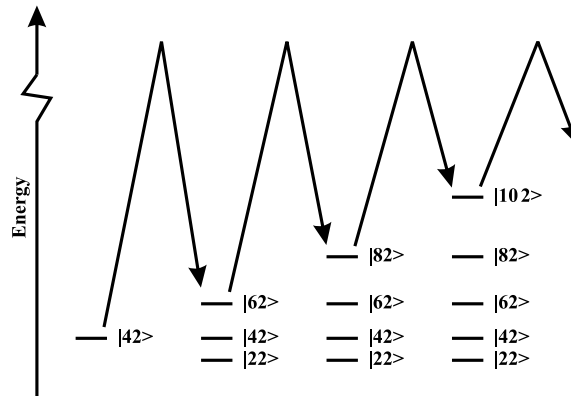


Figure 2.5: Linear non-adiabatic alignment of a linear molecule initially in the  $|JM\rangle=|42\rangle$  state. Each Raman cycle broadens the wave packet.

follow the shape of the alignment pulse. A typical development of  $\langle \cos^2 \theta \rangle$  induced by a linearly polarized non-adiabatic alignment pulse is shown in fig. 2.6. The alignment peaks after the peak of the alignment pulse (fig. 2.6 a) and if the pulse turn-off is sufficiently short the molecules are aligned without the presence of an electric field – field free alignment. The obtained degree of alignment is, like the adiabatic case, dependent on the rotational temperature, anisotropy of molecular polarizability, and intensity of the alignment pulse; but now additional parameters such as the shape and duration of the alignment pulse are also important.

After the peak  $\langle \cos^2 \theta \rangle$  will drop, go through a few damped oscillations and stabilize at a permanent value between  $1/3$  and  $1/2$ [39, 5].

This permanent alignment can be explained with a classical argument in the following way: For the molecules to align along the field axis they must necessarily rotate about an axis perpendicular to the field axis. When the alignment pulse is over, there are no other forces that can move the axis

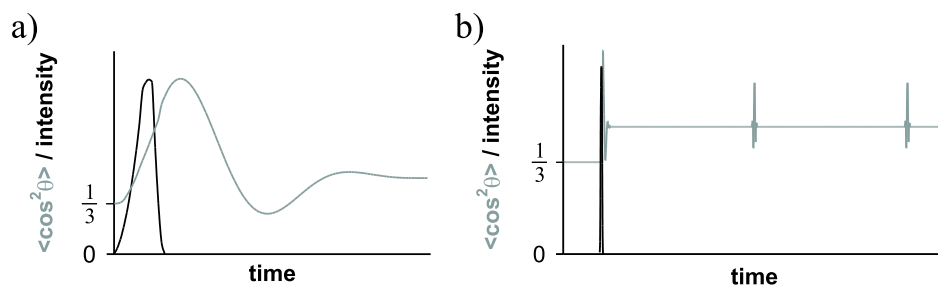


Figure 2.6: Typical development of  $\langle \cos^2 \theta \rangle$  in a non-adiabatic alignment experiment. a) On a short timescale  $\langle \cos^2 \theta \rangle$  (grey curve) peaks after the peak of the alignment pulse (black curve) and goes through a few damped oscillations. b) On a longer timescale rotational revivals occur with regular intervals.

of rotation, which means that the rotation axis is permanently confined to the plane perpendicular to the alignment axis. The probability for a molecule to have a  $\theta$ -angle close to 0 or  $\pi$  is therefore higher than for a uniform distribution. If the axis of rotation is completely confined to the plane perpendicular to the field axis for all molecules then  $\langle \cos^2 \theta \rangle = 1/2$ .

From a quantum mechanical viewpoint the permanent alignment can be explained from the composition of states in the wave packet. As illustrated in fig. 2.5 the conserved  $M$  quantum number restricts the possible values of  $J$  downwards since  $J \geq M$ .  $J$  is however not restricted upwards and the effect of the Raman-cycles is an increase of the average value of  $J$ ,  $\langle J \rangle$ . Since  $J$  is the quantum number of the total angular momentum and  $M$  is the projection on the field axis, increasing  $J$  while keeping  $M$  constant corresponds to moving the rotation axis towards the plane perpendicular to the field axis[5].

On a longer timescale (fig. 2.6 b) transients in  $\langle \cos^2 \theta \rangle$  are observed. These transients are known as rotational revivals of alignment. The ro-

tational revivals appear because the rotational eigenstates comprising the wave packet rephase. Considering the simple case of a linear molecule the energies of the rotational eigenstates are all multiples of  $2B$ , with  $B$  being the rotational constant. As a result rotational revivals for a linear molecule occur at times that are integer multiples of  $1/2B$ .

### 2.2.3 Methods of calculation

Numerical calculations of molecular alignment range from relatively simple calculations to quite complicated cases depending on the duration of the interaction, the polarization of the field, and the symmetry of molecule.

An adiabatic alignment calculation comes down to solving the time independent Schrödinger equation, i.e. finding the eigenstates of the Hamiltonian  $H_0 + H_{int}$ [29]. In the case of non-adiabatic alignment the time dependent Schrödinger equation must be solved. Here, it is advantageous to split the calculation in two parts: An interaction part and a field free propagation[3].

A linear field is easier to handle than an elliptical field, as  $H_{int}$  is simpler and more selection rules are imposed (see table 2.2). The  $M$  quantum number is always conserved for linear fields.

$H_{int}$  for linear and symmetric top molecules only depends on the  $\theta$ -angle. A calculation can be done in the basis of field free eigenfunctions. The interaction conserves the  $K$  quantum number (for symmetric top molecules) and thus only mixes states with different  $J$  quantum number.

Asymmetric top molecules can be divided into two groups: Molecules belonging to the pointgroups  $D_2$ ,  $C_{2v}$ , or  $D_{2h}$  and molecules belonging to other pointgroups ( $C_1$ ,  $C_S$ ,  $C_i$ ,  $C_2$ , or  $C_{2h}$ ). The first group of molecules has coinciding principal axes of polarizability and inertia due to symmetry. I will refer to these molecules as  $C_{2v}$ -type asymmetric tops, since  $C_{2v}$  is a

subgroup of  $D_{2h}$  and very few molecules belong to  $D_2$ .

The coincidence of polarizability and inertia molecular coordinates simplifies calculations on the  $C_{2v}$ -type asymmetric tops. For asymmetric tops in linear fields the interaction is most easily treated in the basis of symmetric top eigenfunctions. The coupling terms then have analytical expressions and are limited by selection rules. In a calculation of non-adiabatic alignment the subsequent field free propagation is then handled by projection back onto the basis of asymmetric top eigenfunction[3].

The simplest calculation is thus adiabatic alignment of a linear or symmetric top molecule, for which the solutions are known as pendular states. Furthermore  $\langle \cos^2 \theta \rangle$  of pendular states can be found directly from the eigenvalues (the energies) without calculation of the eigenfunctions ( $f_{mol}(\theta)$ ) using the Hellman-Feynman theorem[29, 40]. A calculation of  $\langle \cos^2 \theta \rangle$  is therefore not very time consuming and can be done quickly on a standard PC.

Calculations of non-adiabatic alignment are more time consuming, especially for asymmetric top molecules, where the created wave packets consist of a very large number of states[3].

A simple way of calculating non-adiabatic alignment was proposed by Leibscher, Averbukh, and Rabitz[41, 42] (for linear alignment of a linear rotor). They assumed that the alignment pulse was very short compared to molecular rotation, and the molecules therefore could be assumed to be frozen during the interaction with the short ‘ $\delta$ -kick’ pulse. For alignment pulses too long to be characterized as ‘ $\delta$ -kick’ pulses, there are no such shortcuts to the solution and the interaction must be treated by solving a set of coupled differential equations for the expansion coefficients[3].

## 2.3 Classical theories of alignment

### 2.3.1 Boltzmann distribution

At high (room) temperatures the molecular distribution,  $f_{mol}$ , obtained in adiabatic alignment approaches a Boltzmann distribution,

$$f_{mol}(\theta, \phi, \chi) \propto \exp\left(\frac{-E(\theta, \phi, \chi)}{k_B T}\right), \quad (2.8)$$

where  $k_B$  is the Boltzmann constant. The classical energy  $E(\theta, \phi, \chi)$  is equal to  $H_{int}$ . For a linear or prolate symmetric top in a linear field,  $H_{int}$  from table 2.2 can be written as

$$E(\theta) = H_{int} = -\frac{2\pi}{c} I (\Delta\alpha' \cos^2 \theta + \alpha'_\perp) \quad , \quad \Delta\alpha = \alpha_\parallel - \alpha_\perp. \quad (2.9)$$

Equation 2.9 was obtained by changing from  $\varepsilon^2$  to intensity ( $\varepsilon^2 = \frac{2I}{c\epsilon_0}$ ) and from polarizability to polarizability volume ( $\alpha' = \frac{\alpha}{4\pi\epsilon_0}$ ).

Assuming this angular dependence of the energy the Boltzmann distribution (eq. 2.8) becomes[20]

$$f_{mol}(\theta) = \frac{\exp(\frac{2\pi}{ck_B T} I \Delta\alpha' \cos^2 \theta)}{\int_0^\pi \exp(\frac{2\pi}{ck_B T} I \Delta\alpha' \cos^2 \theta) \sin \theta d\theta}. \quad (2.10)$$

The  $\alpha_\perp$  term of  $H_{int}$  does not enter eq. 2.10 as it is a constant energy shift independent of  $\theta$ .

$\langle \cos^2 \theta \rangle$  is obtained from  $f_{mol}$  using the definition in eq. 2.4. Assuming that  $\frac{2\pi}{c} I \Delta\alpha' \ll k_B T$  the exponentials in eq. 2.10 can be replaced by their first order expansions and a simple formula for  $\langle \cos^2 \theta \rangle$  is obtained,

$$\langle \cos^2 \theta \rangle = \frac{1}{3} + \frac{8\pi}{45} \frac{\Delta\alpha' I}{ck_B T}. \quad (2.11)$$

The calculations of adiabatic alignment of CS<sub>2</sub> molecules at two different temperatures shown in fig. 2.7 illustrate when the assumption of a Boltzmann distribution is appropriate. At low rotational temperatures (fig. 2.7 a) the Boltzmann distribution is only a good fit at very low intensities. At high (room) temperature (fig. 2.7 b) the Boltzmann distribution is a good fit at the intensities usually employed in adiabatic alignment experiments.

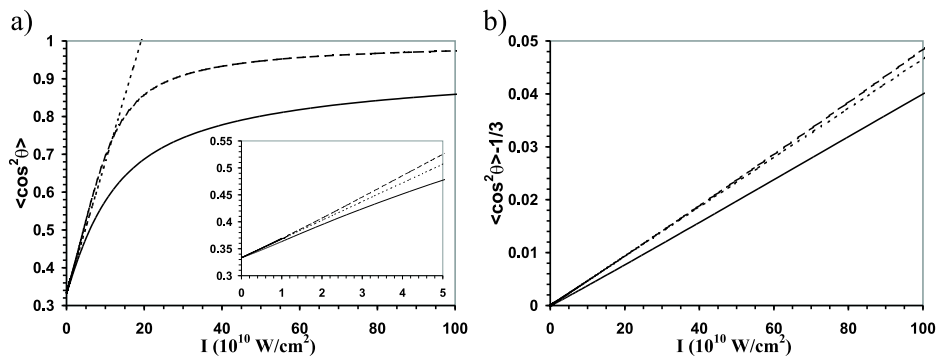


Figure 2.7: Linear adiabatic alignment of CS<sub>2</sub> molecules at two different rotational temperatures. The full curve is from a quantum mechanical calculation solving the time-independent Schrödinger equation, the dashed curve is the Boltzmann distribution, and the dotted curve is its first order approximation (eq. 2.11). a)  $T = 4$  K, the inset is a blow up of the low intensity part, b)  $T = 298$  K.

The Boltzmann distribution is thus a good fit at low intensities or high temperatures, which is also the regime where the simple first order approximation (eq. 2.11) is applicable for linear or symmetric top molecules in a linear field.

### 2.3.2 Classical kicked rotor

Besides the quantum mechanical version of their ‘ $\delta$ -kick’ model, Leibscher, Averbukh, and Rabitz[41, 42] also proposed a classical model for an ensemble of linear rotors subject to a fast kick by an alignment pulse. This model illustrates some key points of non-adiabatic alignment.

In the model, the angular velocity of the linear rotors in the ensemble after the interaction is

$$\omega = \omega_0 - P \sin(2\theta_0). \quad (2.12)$$

In eq. 2.12,  $\omega_0$  is the angular velocity before the interaction,  $\theta_0$  is the  $\theta$ -angle before the interaction, and  $P$  is the “kick strength” defined as

$$P = \frac{1}{4\mathcal{I}} \Delta\alpha \int_{-\infty}^{\infty} \varepsilon(t)^2 dt = \frac{8\pi B}{\hbar} \Delta\alpha' \phi. \quad (2.13)$$

In eq. 2.13,  $\mathcal{I}$  is the moment of inertia,  $B$  is the rotational constant (in  $\text{cm}^{-1}$ ), and  $\phi$  is the fluence (photon energy per unit area).

After the kick each rotor evolves freely and assuming that the initial angular velocity  $\omega_0$  is negligible compared to the angular velocity gained by the kick,

$$\theta(t) = \theta_0 - Pt \sin(2\theta_0). \quad (2.14)$$

From eq. 2.14 it is seen that rotors, for which  $\sin(2\theta_0) \approx 2\theta_0$ , all reach  $\theta = 0$  at  $t = \frac{1}{2P}$ . This model thus predicts that the alignment peaks shortly after the pulse at  $t = \frac{1}{2P}$  and that the obtained degree of alignment is improved if more molecules obey  $\sin(2\theta_0) \approx 2\theta_0$ . This is the case if the molecules are prealigned so that a larger fraction has a small  $\theta_0$ .

## Chapter 3

# Experimental Setup

In this chapter our experimental setup is explained in detail. Since the chapter is also meant to serve as a reference for future students in the group some technical information is included.

In our experiments we wish to align gas phase molecules with one or two laser pulses and subsequently probe the alignment with one or two probe pulses. A schematic overview of our experimental setup is shown in fig. 3.1. The molecular beam consisting of gas phase sample molecules seeded in helium or argon is crossed at  $90^\circ$  with the laser pulses. The probe pulse(s) create ions. The velocity distribution of the ions, which contain information about the molecular alignment, is obtained by accelerating the ions with a static extraction field towards a detector, where a 2-D ion image is created.

In the following sections the different parts of the experiment, the molecular beam, the laser pulses, and the ion imaging, are explained in detail.

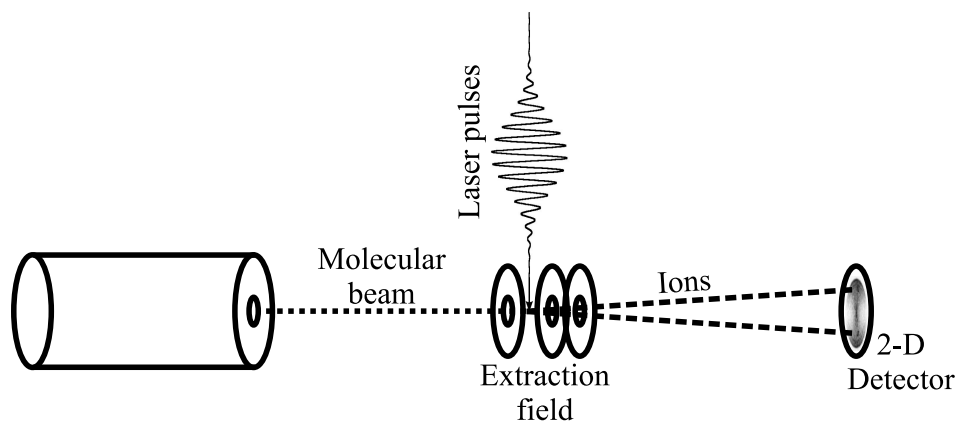


Figure 3.1: Schematic overview of the experimental setup.

## 3.1 The molecular beam

The molecular beam is obtained by expanding a gas of the sample molecules seeded in helium or argon into vacuum. The expansion cools the molecules rotationally to a few degrees Kelvin.[10]

### 3.1.1 Gas flow system

The gas flow system illustrated in fig. 3.2 is used for obtaining a gas of sample molecules seeded in helium or argon.

Helium or argon at moderate pressure (1-4 bar) is bubbled through a pure liquid sample of the molecule under study. The temperature of some of the liquids was kept low with a cold bath, consisting either of ice or a mixture of ethylene glycole and ethanol cooled with dry ice. Thereby the liquid was kept at a temperature where the vapor pressure was 0.5–15 mbar (see appendix A). The main purpose of the cooling was to avoid

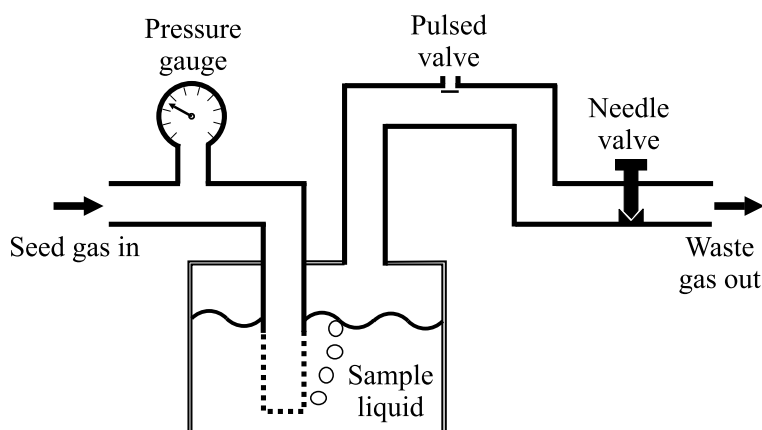


Figure 3.2: Schematic drawing of the gas flow system used for obtaining a gas of sample molecules seeded in helium or argon.

the sample container emptying too fast. In the case of tert-butyl iodide the low temperature was necessary to reduce clustering in the molecular beam.

Along the  $\sim 60$  cm long path from the liquid sample to the pulsed valve the sample molecules can condensate and revaporize several times. This path cannot be temperature controlled and as a result there is no direct relation between the vapor pressure in the sample container and the amount of molecules exiting the valve. Increasing the vapor pressure of iodobenzene from 1 to 10 mbar only result in an increase of  $\sim 25\%$  in total ion signal.

The needle valve is used to control the gas flow rate in the system. We have not observed any dependence of the molecular beam on the flow rate and have therefore used a minimum flow to save seed gas and sample.

### The pulsed supersonic valve

The pulsed valve is a commercially available apparatus (PSV C-211 from R. M. Jordan Company). It opens when a high current electrical pulse cause two conductors to repel and can be operated with a repetition rate of 20 Hz[43]. A jet of gas is ejected through a 0.5 mm nozzle into the vacuum chamber at supersonic speed. As a result of the expansion both translational and rotational motions of the molecules are cooled. A higher backing pressure makes a more efficient cooling but also reduces sample density in the molecular beam. We have used both helium and argon as seed gasses. Argon cools most effectively but also significantly reduces the density of sample molecules in the molecular beam.

#### 3.1.2 Vacuum chambers

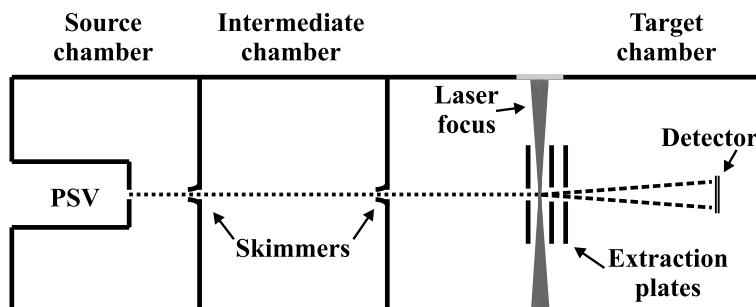


Figure 3.3: The vacuum chambers. The molecular beam travels from the pulsed supersonic valve (PSV) down through the center of the chambers. After interaction with the focused laser beams ions are created. The ions are accelerated down towards the detector by the static electric field of the extraction plates.

The vacuum chamber (fig. 3.3) is split in three to ensure a low background pressure in the interaction region. The pulsed supersonic valve

(PSV) ejects a jet of gas into the source chamber. The molecules pass through a 1 mm skimmer into the intermediate chamber. After traveling through the intermediate chamber another 1 mm skimmer is placed at the entrance to the target chamber. The skimmers serve to select the central, coldest part of the molecular beam and provide a well defined sample volume. The source and intermediate chambers are pumped by diffusion pumps. The target chamber is pumped by a turbo pump and two cold traps filled with liquid nitrogen ensures a low background pressure ( $\sim 7 \times 10^{-8}$  mbar). A detailed drawing of the pumping system, valves, and pressure gauges is found in [44].

In the target chamber the molecular beam is crossed at  $90^\circ$  with the focused laser beams. The experiments are performed on the front (early part) of the molecular pulse where the rotational cooling is best and the chance of clusters is minimal. The ions created in the experiment are accelerated by the static field between the extraction plates and travel toward the detector.

## 3.2 Laser pulses

### 3.2.1 Alignment and probe pulses

Our alignment experiments employ one or two alignment pulses and one or two probe pulses. The involved pulses are summarized in table 3.1.

The adiabatic alignment pulses were obtained as the fundamental (1064 nm) output of an injection seeded Q-switched Nd:YAG nanosecond laser. The non-adiabatic alignment pulses originate from a regenerative amplified Ti:Sapphire femtosecond laser system. The  $\sim 100$  fs pulses were stretched to the desired durations (0.5–3.5 ps).

We have used two different probe schemes. The first probe scheme

**Alignment pulses**

| Pulse                   | Wavelength | Duration, $\tau_{\text{FWHM}}$ | Peak intensity, $I_0$                           |
|-------------------------|------------|--------------------------------|---|
| Non-adiabatic alignment | 800 nm     | 0.5–3.5 ps                     | $1\text{--}13 \times 10^{12}$ W/cm <sup>2</sup> |
| Adiabatic alignment     | 1064 nm    | 3.5 ns or<br>9 ns              | $1\text{--}9 \times 10^{11}$ W/cm <sup>2</sup>  |

**Probe pulses**

| Pulse             | Wavelength | Duration, $\tau_{\text{FWHM}}$ | Peak intensity, $I_0$                            |
|-------------------|------------|--------------------------------|--|
| Dissociation      | 266 nm     | 0.3–1.5 ps                     | $0.5\text{--}2 \times 10^{12}$ W/cm <sup>2</sup> |
| Ionization        | 304 nm     | 2 ns or 5 ns                   | $1\text{--}10 \times 10^8$ W/cm <sup>2</sup>     |
| Coulomb explosion | 800 nm     | $\sim 20$ fs                   | $\sim 2 \times 10^{14}$ W/cm <sup>2</sup>        |

Table 3.1: The laser pulses used in our experiments. Pulse durations and peak intensities vary in the experiments.

employs two laser pulses. A 266 nm pulse breaks the C-I bond. The velocity vector of the I fragment reflect the position of the C-I bond axis. The iodine atom is subsequently ionized through a resonantly enhanced multi photon ionization (REMPI) process by a tunable nanosecond pulse at 304 nm. This probe scheme is explained in more detail in sect. 4.2.

The other probe scheme employs an ultra-short intense  $\sim 20$  fs 800 nm pulse that strips one or more electrons from the molecule causing the molecule to fragment into ions, a process known as a Coulomb explosion. The velocity vectors of the ions reflect the molecular distribution of orientations and can be used as a qualitative measure of alignment. This probe scheme is explained in more detail in sect. 7.1.

### 3.2.2 Optical setup

#### Nanosecond pulses

The optical setup of the nanosecond pulses is illustrated in fig. 3.4.

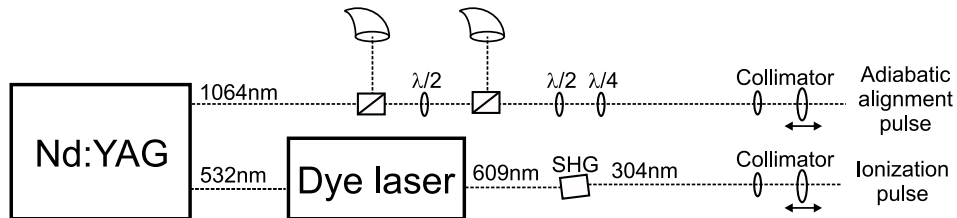


Figure 3.4: Schematic overview of the optical setup of the nanosecond pulses.

An injection seeded Q-switched Nd:YAG laser is frequency doubled in a BBO crystal to 532 nm. We use the residual 1064 nm as adiabatic alignment pulse and the 532 nm to produce the ionization pulse (the BBO crystal is removed in experiments that do not use the ionization pulse). We have used two different Nd:YAG lasers: A Coherent Infinity and a Spectra Physics Quanta Ray laser. The main difference is in the duration of the produced pulses. The duration of the 1064 nm pulses is 3.5 ns for the Infinity laser and 9 ns for the Quanta Ray laser.

#### *Adiabatic alignment pulse*

The 1064 nm beam meets two polarizers and a  $\lambda/2$ -plate that ensure a linear polarization and give the option of tuning the power by rotating the  $\lambda/2$ -plate. For the Quanta Ray laser the beam size was reduced with a telescope before passing through the polarizers. The subsequent  $\lambda/2$ - and  $\lambda/4$ -plates controls the polarization of the pulse. By rotating the second  $\lambda/2$  plate the polarization can be: linear (vertical or horizontal), circular,

or elliptical with a vertical major axis.

The collimator consisting of a diverging and a focusing lens serve to increase the beam size thereby decreasing the focal spot size. Furthermore the beam can be made slightly diverging or converging by tuning the distance between the two lenses.

#### *Ionization pulse*

The 532 nm pulses from the Nd:YAG laser pump a dye laser (Lambda Physik Scanmate 2). We use the Rhodamin 640 dye and methanol as solvent. With this dye the output wavelength can be tuned in range 605–620 nm. The output from the dye laser is frequency doubled in a KDP crystal to yield ultra violet pulses around 304 nm. The duration of the 304 nm pulses is 2 ns (Infinity Nd:YAG laser) or 5 ns (Quanta Ray Nd:YAG laser). The 304 nm pulse is optically delayed to 10 ns after the 1064 nm pulse. A collimator like the one in the 1064 nm beam path is also placed in this beam and serve the same purpose.

#### **Femto- and picosecond pulses**

The optical setup of the femto- and picosecond pulses is illustrated in fig. 3.5.

The short pulses originate from a regenerative amplified modelocked Ti:Sapphire femtosecond laser system. The output pulses from the laser system have a duration of approximately 100 fs. Our old amplification system (Clark) was capable of pulse energies up 0.8 mJ. The new (Spitfire) system used in the most recent experiments delivers up to 2 mJ per pulse.

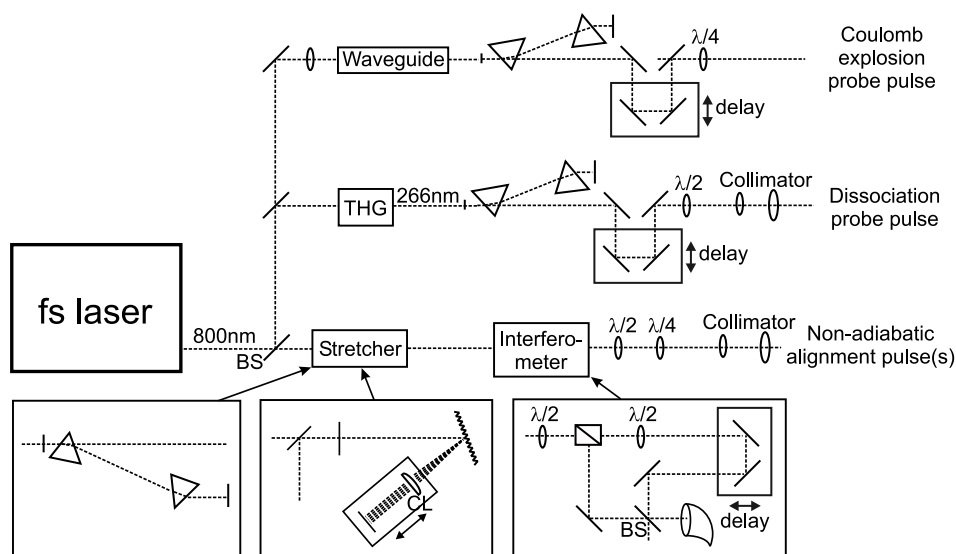


Figure 3.5: Schematic overview of the optical setup of the femto- and picosecond pulses (BS=beamsplitter, CL=cylindrical lens).

#### *Non-adiabatic alignment pulse*

A beamsplitter (BS) transmits most of the pulse energy ( $\sim 70\%$ ) to the beam path of the non-adiabatic alignment pulses. The pulses are stretched to the desired pulse duration (0.5–3.5 ps).

In our first experiments [2, 3] the stretching was done by a double pass through a pair of SF11 Brewster prisms. In that case the pulse duration is determined by the distance between the prisms. In our more recent experiments the prisms were replaced by a grating stretcher[4, 5, 6, 7]. The diffracted beam from the grating is collimated by a cylindrical lens (CL) and directed on the  $0^\circ$  end mirror. A second  $0^\circ$  mirror sends the beam on an extra roundtrip through the stretcher. The beam thus passes the grating four times. The grating stretcher has the advantage that the pulse

duration is easily tuned by changing the distance from the grating to the cylindrical lens while keeping the distance from lens to end mirror constant at the focal length of the lens. When the distance between the grating and the lens is equal to the focal length of the lens, the pulses are not stretched. Making the distance from grating to lens longer or shorter corresponds to stretching with a negative or positive chirp.

In the two pulse non-adiabatic alignment experiments the stretched pulse passes into a modified Mach-Zender interferometer. By rotating the  $\lambda/2$ -plate before the polarizing beamsplitter the energy ratio between the two pulses can be tuned while keeping the total pulse energy constant. For experiments that only require one non-adiabatic alignment pulse the beamsplitter is removed and the first  $\lambda/2$ -plate used for controlling the pulse energy.

As for the adiabatic alignment pulse,  $\lambda/2$ - and  $\lambda/4$ -plates and a collimator are placed after the interferometer, to control polarization and beam size.

#### *Dissociation pulse*

200–250  $\mu\text{J}$  of the 100 fs laser pulse are used to create the 266 nm dissociation pulse. Third harmonic generation (THG) of the 800 nm beam is obtained by frequency doubling in a BBO crystal and subsequent sum frequency mixing of the residual 800 nm and the created 400 nm in a second BBO crystal, resulting in 266 nm.

In the non-adiabatic alignment experiments, the created 266 nm pulses were compressed with a prism pair to 250–400 fs. In the adiabatic alignment experiment the distance between the prisms was minimized to stretch the pulses to 1.5 ps. The pulses were stretched to avoid direct multi photon ionization from the combined 266 nm and 1064 nm fields.

The Schneeberger delay stage used in the non-adiabatic alignment experiments can be translated up to 50 cm corresponding to a double pass delay of up to 3.3 ns. The stage position is measured with a precision of 0.01 mm corresponding to 0.07 ps.

The pulse energy was 9  $\mu\text{J}$  in the adiabatic alignment experiments and 4  $\mu\text{J}$  in the non-adiabatic alignment experiments. With the  $\lambda/2$ -plate placed before the collimator the linear polarization can be changed from horizontal to vertical.

#### *Coulomb explosion pulse*

Removing the mirror that couples into the 266 nm beam, the 800 nm pulse is focused by a lens on a hollow core waveguide filled with argon. The passage through the waveguide increases the spectral width of the pulse, making it possible to compress it with a prism pair to 20 fs or shorter[45]. The translation stage is the same Schneeberger stage used for the 266 nm beam. The  $\lambda/4$ -plate enables a choice between vertical linear polarization and circular polarization.

#### **Combining the laser pulses**

The different beams are combined colinearly using dichromatic  $0^\circ$  mirrors (fig. 3.6). When using the Coulomb explosion probe, which has the same color (800 nm) as the non-adiabatic alignment pulse, a 50/50 beamsplitter is used instead of the first dichromatic mirror. The beams are focused with an achromatic lens (focal length 30 cm) on the molecular beam. The achromatic lens is designed to make the involved colors focus at the same distance from the lens. The collimators installed in the various beam paths can make the beams slightly diverging or converging and thus allow fine adjustments to the focal distance. In some cases some beams were slightly

defocused to increase the spot size.

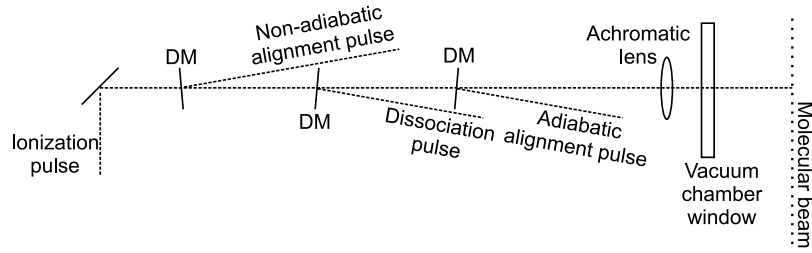


Figure 3.6: The beams are made colinear with dichromatic mirrors (DM) and focused on the molecular beam with an achromatic lens.

The spatial overlap of the beams was ensured by inserting a broadband mirror before the vacuum chamber window and focus the beams on a  $20\ \mu\text{m}$  pinhole. A replica of the chamber window is placed in the path. An overlap in the pinhole corresponds to an overlap on the molecular beam. Finally the spatial overlap is fine tuned on the molecular beam by optimizing an ion signal.

The temporal overlap of the short pulses is found by replacing the pinhole with a BBO crystal and monitoring the produced  $400\ \text{nm}$  from either difference frequency mixing of  $266\ \text{nm}$  and  $800\ \text{nm}$  or from sum frequency mixing of the two different  $800\ \text{nm}$  pulses. The timing of the nanosecond pulses is controlled electronically.

### 3.3 Data acquisition and treatment

#### 3.3.1 Ion imaging

To project the ions onto the detector we use the velocity imaging setup of Eppink and Parker[46]. This setup consists of three plates with circular

apertures as illustrated in fig. 3.1. Different voltages are applied to the first two plates, the third is grounded. The electric field accelerates the ions toward the detector. If the ratio of the applied voltages is chosen correctly, ions created different places in the laser focus with the same velocity vector are projected to the same spot on the detector. The positions of the ion hits on the detector are therefore a map of the velocity vectors of the ions, or more precisely a map of the 2-D projections of the ion velocity vectors.

The time of flight (*TOF*) from the ions are created to they hit the detector is proportional to the square root of the ratio of mass ( $m$ ) and charge ( $Z$ ) of the ions:  $TOF \propto \sqrt{m/Z}$ . Ions with different masses will thus arrive at the detector at different times.

The detector consists of a micro channel plate (MCP) and a phosphor screen. When an ion hits the MCP it triggers an electron avalanche. This electron avalanche is guided so that the electrons leave the MCP from the same point as it was hit by the ion. The electrons hit the phosphor screen and excite the phosphor in a localized spot which subsequently emits light. The position of this ‘blob’ of light on the phosphor screen thus corresponds to the position of the ion hit. The voltages on the detector can be time gated so that only ions with certain flight times (typically  $I^+$ ) are seen on the screen. A CCD camera records images of the phosphor screen.

Each image from the CCD camera is immediately analysed by a computer and the center of each blob of light is found and stored[47]. The identification of the position of each blob means that all ion hits are counted with the same weight regardless of the size of the resulting blob of light, which can vary because the detector does not have uniform sensitivity. It also gives a better resolution, in principle sub-pixel resolution. From the stored blob-positions angular and radial distributions can be calculated. Assuming a gaussian shape of each blob an ion image can be constructed

as illustrated in fig. 3.7.

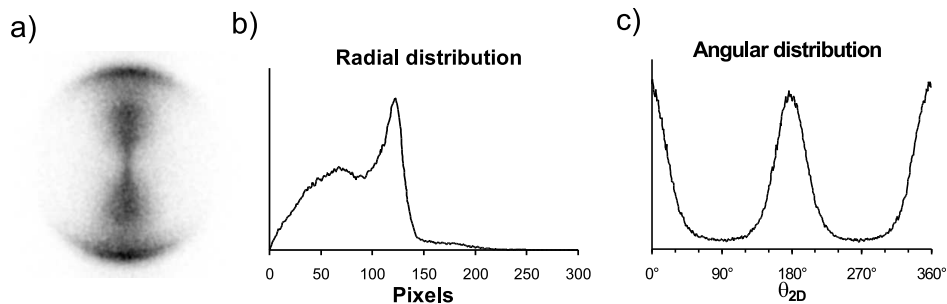


Figure 3.7: a) Ion image of I<sup>+</sup> ions from aligned iodobenzene molecules, b) radial distribution, c) angular distribution.

The pixel scale in the radial distribution is easily converted to mm and since the flight time is known, the projected ion velocity can be calculated. As the ion image is a two dimensional projection, it only contains information about the ion velocity in the detector plane. From the angular distribution  $\langle \cos^2 \theta_{2D} \rangle$  can be calculated,  $\theta_{2D}$  is the angle to the vertical axis. We often use  $\langle \cos^2 \theta_{2D} \rangle$  as a qualitative measure of the degree of alignment. In general it is mathematically impossible to extract the complete 3-D velocity distribution from its 2-D projection unless certain assumptions regarding the initial 3-D distribution can be made.

### 3.3.2 Abel inversion

If the ion velocity distribution has cylindrical symmetry around an axis in the detector plane a transformation from the 2-D projection back to the initial 3-D distribution exists. This transformation is known as the inverse Abel transformation or Abel inversion. Mathematically the transformation is simple[48],

$$f_{3D}(r, z) = -\frac{1}{\pi} \int_r^\infty \frac{\frac{d}{dx} f_{2D}(x, z)}{\sqrt{x^2 - r^2}} dx . \quad (3.1)$$

In eq. 3.1 the original distribution  $f_{3D}$  is a function of two coordinates:  $z$  is the symmetry axis coordinate and  $r = \sqrt{x^2 + y^2}$  is the distance from the symmetry axis.  $f_{2D}$  is the projected distribution and  $(x, z)$  is the projection plane.

In principle the original distribution can be obtained through eq. 3.1. In practice it is not very useful on ion images with finite resolution since it requires the derivative of the noisy projected image and has a singularity (for  $x \rightarrow r$ ).

Until a few years ago the numerical methods for Abel inversion produced quite bad representations of the original distribution, sometimes with negative densities. Then two very different methods of obtaining a reliable Abel inversion was proposed: Vrakking's iterative method[49] and the basis-set expansion (BASEX) method of Reisler's group[48].

The idea of the iterative method by Vrakking is to compare the projection of a trial 3-D distribution with the ion image and correct the 3-D distribution with the differences between the projection and the ion image. After 30–40 iterations the projection is indistinguishable from the original ion image.

The BASEX method expands the ion image in a basis of gaussian-type functions. These basis functions are "well behaved", that is they can be inverted easily as they are projections of known functions. The inverted distribution is then found by using the set of expansion coefficients on the inverted basis. The ability of the BASEX method to recreate the original distribution thus depends on how well the ion image is expandable in the basis.

The computational time required for the BASEX inversion is  $\sim 50$  times shorter than for the iterative inversion. Computational time is however not a big issue since the iterative inversion can be done in 10–30 minutes on a slightly outdated 1 GHz PC.

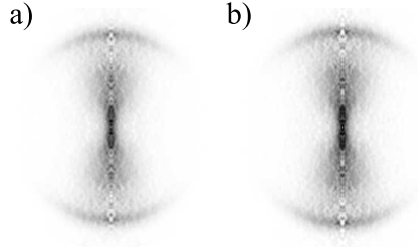


Figure 3.8: Abel inverted images of the 2-D ion image shown in fig. 3.7 a). The images are represented as a slice through the 3-D distribution ( $f_{3D}(r, z)$ ). a) Using Vrakking’s iterative approach[49], b) BASEX method of Reisler and coworkers[48].

Figure 3.8 shows Abel inverted images of the ion image shown in fig. 3.7 a) obtained with the Vrakking iterative approach and with the BASEX method. The inverted images are slices through the 3-D distribution corresponding to a  $f_{3D}(r, z)$  plot.

The images in fig. 3.8 appear quite similar to the naked eye, but a further analysis reveals some small differences. The angular distributions of the BASEX inversion are a bit noisier than those of the iterative inversion. The radial (speed) distributions are however better reproduced by the BASEX method. In our alignment experiments we are mostly interested in the angular distributions and we have therefore used the iterative Abel inversion method.

The noise on the centerline, which is present in both inverted images is an unavoidable effect of the noise and limited resolution of the 2-D image.

The input for the inversion programs is a matrix of ion densities. This

matrix is constructed like the 2-D ion image by assuming a gaussian shape of each ion hit. We have found that a gaussian width of 3 pixels is usually a good choice for insuring a relatively smooth distribution suitable for inversion. Since each ion hit is determined with sub-pixel accuracy it is possible to enlarge the ion image, so that it covers a larger matrix than the one determined by the camera resolution. This way the centerline pixels cover a smaller fraction of the image.

## Chapter 4

# Adiabatic alignment of iodobenzene – control of the photodissociation

The idea of using an intense adiabatic laser pulse to obtain a high degree of alignment of rotationally cold molecules was first presented in 1995 by Friedrich and Herschbach[29]<sup>1</sup>. Kim and Felker[51] presented the first experimental evidence of adiabatic alignment, a change of Raman bands indicating transitions between pendular states in the presence of a strong laser field. More direct evidence was presented in 1999 by Stapelfeldt and coworkers[52]. They used ion imaging to show that I<sub>2</sub> molecules subject to an adiabatic alignment pulse obtained a high degree of alignment ( $\langle \cos^2 \theta \rangle = 0.81$ ). They also demonstrated alignment of a range of other

---

<sup>1</sup>Zon and Katsnel'son[50] solved the quantum mechanical equations for a symmetric top molecule in an intense non-resonant field as early as 1975. The implications in terms of alignment was however not addressed

molecules including iodobenzene[53].

The alignment was used to control the photodissociation of  $I_2$  at 485 nm[54]. At this wavelength the photodissociation of  $I_2$  can either go through a perpendicular transition resulting in two ground state I ( $^2P_{3/2}$ ) atoms or a parallel transition resulting in one ground state I atom and one spin excited  $I^*$  ( $^2P_{1/2}$ ) atom. By polarizing the 485 nm dissociation pulse either parallel or perpendicular to the alignment axis one transition could thus be favored over the other.

Our work on adiabatic alignment of iodobenzene was a continuation of this work. We wanted to demonstrate a new probe scheme, photodissociation at 266 nm followed by selective ionization of the iodine photofragment. This probe scheme allowed us to obtain the distribution of molecular orientations *prior* to the photodissociation. We also wanted to use alignment to control the photodissociation of iodobenzene as it had been demonstrated for  $I_2$ . Most of the results presented here are published in [1].

## 4.1 Idea

The experimental idea is illustrated in fig. 4.1. The experiment involves three different linearly polarized pulses. The adiabatic alignment pulse aligns the major axis of polarization, which is the C–I bond axis. At the peak of the alignment pulse (where the degree of alignment peaks cf. sect. 2.2.2) a 1.5 ps 266 nm pulse cleaves the C–I bond of some of the aligned molecules, producing phenyl radicals and iodine atoms in the ground (I) and spin excited ( $I^*$ ) states. The 266 nm pulses are stretched to 1.5 ps to avoid direct multi photon ionization from the combined 266 nm and 1064 nm fields. When the alignment pulse is over, a third (304 nm) pulse selectively ionizes either ground state or spin-excited iodine atoms.

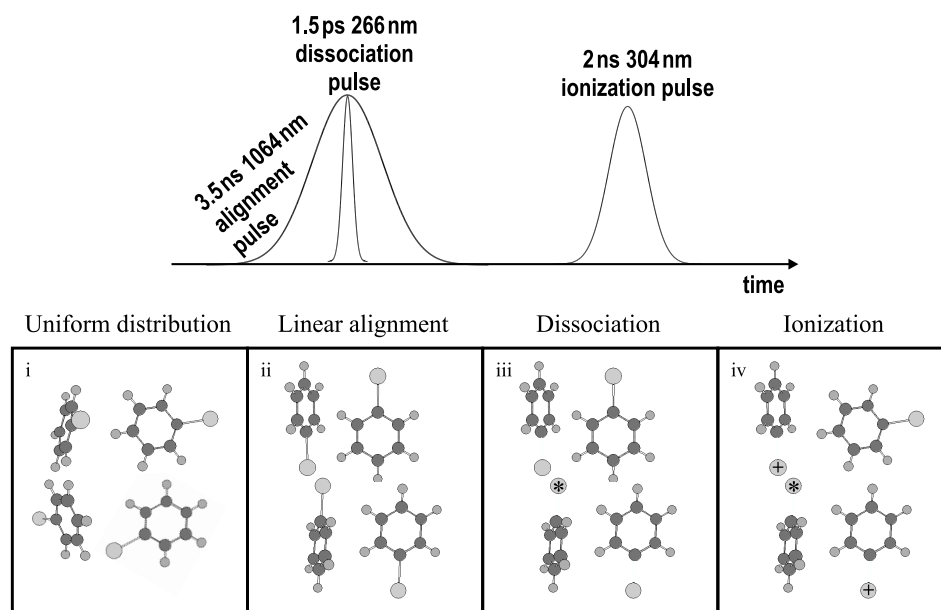


Figure 4.1: Photodissociation of adiabatically aligned iodobenzene molecules. Top: The laser pulses involved. Bottom: Cartoon showing the experimental idea: Molecules, initially with a uniform distribution (i) are subject to a linearly (vertically) polarized adiabatic alignment pulse, which aligns the major axis of polarizability (the C–I bond axis) (ii). The aligned molecules are then dissociated by the 266 nm pulse (iii), which cleaves the C–I bond and produces phenyl radicals and iodine atoms in the ground (I) and spin excited ( $I^*$ ) states. When the alignment pulse is over the iodine photofragments are ionized by the ionization pulse (iv). By tuning the wavelength of the ionization pulse we can select to ionize either I or  $I^*$ .

As explained below (sect. 4.3), the dissociation of iodobenzene can go through two different channels. These two dissociation channels have different dependencies on the relative orientation of molecule and polarization

of the dissociation pulse. This difference means that alignment can be used as a control tool for the photodissociation.

## 4.2 Resonantly enhanced multi photon ionization of iodine

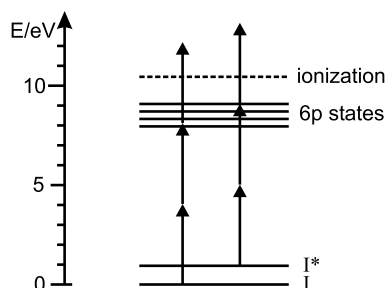


Figure 4.2: Resonantly enhanced multi photon ionization (REMPI) of iodine atoms

To ionize the photofragment iodine atoms we use a nanosecond pulse with a wavelength close to 304 nm. As illustrated in fig. 4.2 the ionization process is a 2+1 resonantly enhanced multi photon ionization (REMPI). Two photons promote ground state ( $^2P_{3/2}$ ) I-atoms or spin-excited ( $^2P_{1/2}$ ) I\*-atoms to highly excited (6p) states, from which a third photon ionize the atom. By tuning the wavelength the ionization of either I or I\* is resonantly enhanced, see table 4.1.

For iodobenzene and the other molecules studied the absorption cross section at 304 nm is much smaller than at 266 nm (see appendix A). The contribution of  $I^+$  ions from dissociation and subsequent ionization by the 304 nm pulse is therefore small. Absorption at 304 nm leads almost ex-

| Initial state      | Resonance state[55] | Wavelength <sup>2</sup> |
|--------------------|---------------------|-------------------------|
| I ( $^2P_{3/2}$ )  | 6p $^4D_{7/2}$      | 304.59 nm               |
| I* ( $^2P_{1/2}$ ) | 6p $^4D_{1/2}$      | 303.96 nm               |

Table 4.1: The wavelengths used for making resonantly enhanced multi photon ionization (REMPI) of iodine. The tabulated wavelengths are calibrated against the spectral lines of Ne using an optogalvanic lamp[56].

clusively to the formation of ground state I (for iodobenzene the relative quantum yield of I\* is 0.005[57]).

We have (so far) only used the scheme of dissociation and subsequent ionization on molecules with C–I bonds. The reason is that the REMPI wavelengths of other photofragments such as Br or OH are close to 260 nm, where the absorption cross sections of molecules are usually much bigger.

A minor problem with the ionization pulse is that the spectral width is almost too narrow. If the spectral width is narrower than the Doppler profile of the iodine atoms, the REMPI-probe will only select part of the Doppler profile. To overcome this we have either scanned the wavelength over the Doppler profile or used a pulse so intense that the resonance is sufficiently power broadened.

### 4.3 Photodissociation of iodobenzene

The group of El-Sayed has shown that photodissociation of iodobenzene in the range 220-305 nm occurs through two main channels[58]. One channel is the excitation from a non-bonding orbital on the iodine atom to an anti-bonding orbital along the C–I bond. This  $n \rightarrow \sigma^*$  transition leads to a

<sup>2</sup>Eppink and Parker[55] report these wavelengths as 304.55 nm (I) and 304.02 nm (I\*).

fast breakage of the C–I bond. The other channel is an excitation from a bonding to an anti-bonding orbital ( $\pi \rightarrow \pi^*$ ) of the aromatic  $\pi$ -system. The energy of this transition is quickly redistributed to the C–I bond, so that the end result of both channels is the breaking of the C–I bond.

Dissociation through the  $\pi \rightarrow \pi^*$  channel leaves the phenyl radical higher vibrationally excited than the direct dissociation through the  $n \rightarrow \sigma^*$  channel. Fragments produced by dissociation through the  $\pi \rightarrow \pi^*$  channel will thus have less kinetic energy than fragments originating from the  $n \rightarrow \sigma^*$  dissociation. The detected  $I^+$  ions can therefore be separated in the two dissociation channels.

#### 4.3.1 The $n \rightarrow \sigma^*$ dissociation channel

The  $n \rightarrow \sigma^*$  dissociation channel only involves bond-localized orbitals. It is therefore common to all molecules with a C–I bond. Figure 4.3 shows the potential surfaces involved in the transition for  $\text{CH}_3\text{I}$ . The precise energies and absorption cross sections are molecule dependent but the basic mechanism is common to all molecules with a C–I bond.

Eppink and Parker [59] report the mechanism to be as follows: The parallel  $^1Q_0 \rightarrow ^3Q_0$  transition is the most dominant. Molecules excited to the  $^3Q_0$  surface will either dissociate into  $\text{CH}_3$  and  $I^*$  or make a curve crossing to the  $^1Q_1$  surface resulting in  $\text{CH}_3$  and  $I$ . The perpendicular transitions  $^1Q_0 \rightarrow ^1Q_1$  and  $^1Q_0 \rightarrow ^3Q_1$  that lead to  $\text{CH}_3$  and  $I$  have smaller cross sections but are also present ( $^1Q_0 \rightarrow ^1Q_1$  much more than  $^1Q_0 \rightarrow ^3Q_1$ ). The  $n \rightarrow \sigma^*$  excitation will thus either result in  $I^*$  through a pure parallel transition ( $^1Q_0 \rightarrow ^3Q_0$ ) or  $I$  through a transition that is mainly parallel but has a minor perpendicular component.

Assuming the transition is not saturated (cf. appendix C.1) the probability of dissociation through a combined parallel and perpendicular tran-

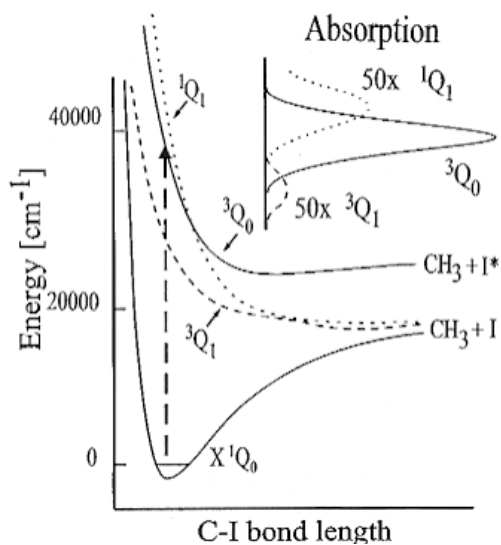


Figure 4.3: Schematic diagram showing the potential surfaces involved in the photodissociation of  $\text{CH}_3\text{I}$  at 266 nm. Reprinted from [59].

sition, such as the  $n \rightarrow \sigma^*$  channel has the dissociation probability<sup>3</sup>,

$$P_{diss}^{n \rightarrow \sigma^*} = \sigma_{n \rightarrow \sigma^*} \Phi_0 \frac{3}{2-A} \left( A \cos^2 \theta + (1-A) \sin^2 \theta \right). \quad (4.1)$$

In eq. 4.1,  $\Phi_0$  is the photon flux,  $\sigma_{n \rightarrow \sigma^*}$  is the orientation averaged absorption cross section,  $\theta$  is the angle between the C-I bond axis and the dissociation polarization, and the  $A$  parameter designates how parallel or perpendicular the transition is:  $A = 0$  corresponds to a pure perpendicular transition and  $A = 1$  corresponds to a pure parallel transition. Equation 4.1 is derived in appendix C.2.

<sup>3</sup>eq. 4.1 is equivalent to  $P_{diss} \propto 1 + \beta P_2(\cos \theta)$  (see appendix C.2).

### 4.3.2 The $\pi \rightarrow \pi^*$ dissociation channel

The  $\pi \rightarrow \pi^*$  channel involve the aromatic ring and is similar to the same transition of benzene ( ${}^1A_{1g} \rightarrow {}^1E_{1u}$ ). The transition perpendicular to the plane is symmetry forbidden (the bonding ( $\pi$ ) and anti-bonding ( $\pi^*$ ) orbitals of the aromatic ring have the same symmetry with respect to the symmetry operation of mirroring in the plane of the molecule). The transition dipole moments along the other two coordinates are equal due to symmetry.

In conclusion the  $\pi \rightarrow \pi^*$  channel is a planar transition, which means that the transition dipole moment is proportional to  $\sin^2 \gamma$  with  $\gamma$  being the angle between the dissociation laser polarization and the axis perpendicular to the molecular plane.

Transforming to Euler angles and once again assuming that the transition is not saturated, the probability of dissociation is (eq. C.14)

$$P_{diss}^{\pi \rightarrow \pi^*} = \sigma_{\pi \rightarrow \pi^*} \Phi_0 \frac{3}{2} (1 - \sin^2 \theta \sin^2 \chi). \quad (4.2)$$

### 4.3.3 Promptness of the dissociation

Since the velocity vectors of the iodine fragments are used as a measure of the molecular alignment, it is important to ensure that the molecules do not rotate during the photodissociation. This assumption is known as the axial recoil approximation. After the dissociation the rapid increase of the moment of inertia and the conservation of angular momentum cause the fragmented molecule to stop its rotation.

Zewail and coworkers[60] found that dissociation through the  $n \rightarrow \sigma^*$  channel occurs within 0.7 ps and dissociation through the  $\pi \rightarrow \pi^*$  channel within 2.2 ps. The rotational period of iodobenzene (perpendicular to

the C–I bond axis) is  $\sim 700$  ps (see appendix A), rotation of iodobenzene molecules during the dissociation is thus negligible except for highly excited rotational states. The same assumption can be made for the other molecules studied. The fastest molecule, methyl iodide, has a rotational period of 66.7 ps, two orders of magnitude slower than the dissociation.

## 4.4 Linear alignment

### 4.4.1 Ion images

Figure 4.4 shows  $I^+$  ion images recorded with and without the presence of the alignment pulse.

Focusing first on the images recorded without the presence of the alignment pulse, the image in fig. 4.4 a) shows  $I^+$  ions from REMPI of ground state I. The image has two main features: An outer ring of high kinetic energy ions (7–10 mm) which is angularly confined along the vertical polarization of the dissociation pulse and a region of low kinetic energy ions (0–7 mm) with a more uniform distribution. We identify the high kinetic energy ions in the outer ring as ions originating from the mainly parallel  $n \rightarrow \sigma^*$  channel, and the low kinetic energy ions as ions originating from the  $\pi \rightarrow \pi^*$  channel.

The image in fig. 4.4 c) shows  $I^+$  ions from REMPI of  $I^*$ . This image has the same main features as the previous image. The image is smaller since some of the energy is now stored in the excitation of the I atom. The outer ring ( $n \rightarrow \sigma^*$  channel) is slightly more confined since the transition is now a pure parallel transition with no perpendicular component. The yield of  $I^*$  from the  $\pi \rightarrow \pi^*$  channel is low and concentrated in the center of the image. When the 1064 nm alignment pulse is included a confinement of the  $I^+$  ion distribution along the polarization of the pulse is observed,

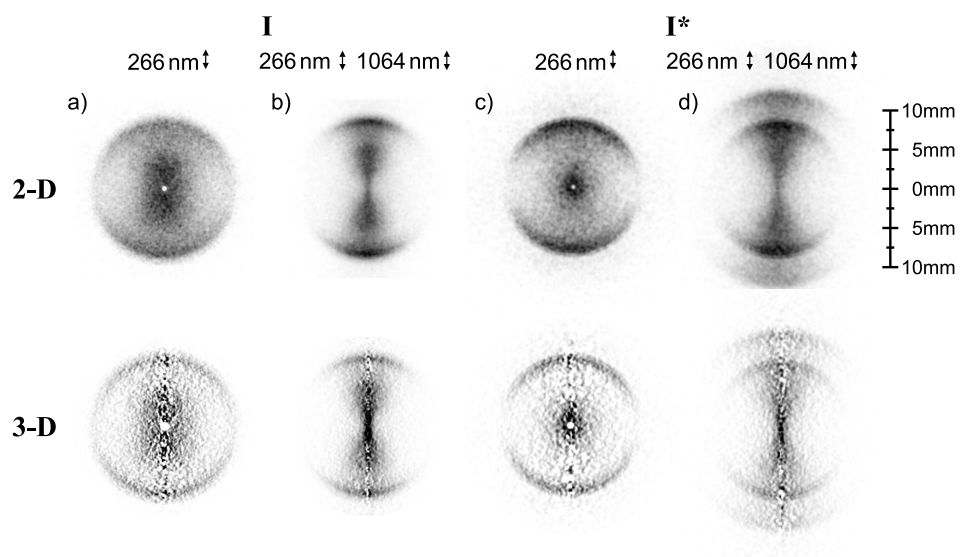


Figure 4.4: Ion images of  $I^+$  ions from REMPI of iodine photofragments using a vertically polarized 266 nm pulse. Top row: 2-D ion images, bottom row: Abel inverted images represented as a slice through the 3-D distribution. a+b) REMPI wavelength set to ionize ground state I, c+d) REMPI wavelength set to ionize  $I^*$ . a+c) Without alignment pulse, b+d) With a vertically polarized alignment pulse.

which we interpret as molecular alignment.

The confinement in the distribution is visible for both I (fig. 4.4 b) and  $I^*$  (fig. 4.4 d). In the latter case an extra ring of high kinetic energy ions also appears. We identify this extra ring as  $I^*$  fragments from a dissociation channel involving the absorption of both a 266 nm photon and a 1064 nm photon. This channel does not produce ground state I. The extra ring in the image of fig. 4.4 d) illustrates a major problem in the application of adiabatic alignment. The molecules are only aligned in the presence of the alignment field and that field can interfere with the process, one wish to

study.

In the aligned ion image of ground state I (fig. 4.4 b) there is no extra ring and we assume that the presence of the alignment field changes the molecular distribution without otherwise affecting the photodissociation leading to I. For all the images an image recorded without the ionization pulse is subtracted to account for the small ( $\sim 10\%$ ) background of  $I^+$  ions produced directly by dissociative ionization.

Since all laser pulses have vertical linear polarization there is cylindrical symmetry in the ion velocity distribution and the images can therefore be Abel inverted (cf. sect. 3.3.2). From the Abel inverted images radial and angular distributions can be extracted.

#### 4.4.2 Kinetic energy distributions

The radial (velocity) distributions can be converted to kinetic energy distributions. The kinetic energy distributions shown in fig. 4.5 are extracted from the Abel inverted ion images in fig. 4.4.

Comparing the kinetic energy distributions without alignment pulse (fig. 4.5 a and b), it is seen that the kinetic energy difference between I and  $I^*$  photofragments of the  $n \rightarrow \sigma^*$  channel is 0.23 eV corresponding to a difference in total kinetic energy (of both iodine and phenyl radical) of 0.61 eV. This difference is smaller than the energy difference between I and  $I^*$ , which is 0.943 eV. We therefore conclude that the phenyl radical is most excited vibrationally when the  $n \rightarrow \sigma^*$  excitation leads to ground state I.

As seen from the (ground state) I kinetic energy distribution of aligned molecules (fig. 4.5 c) the yield of both dissociation channels is increased when the molecules are aligned. Figure 4.5 d) shows the  $I^*$  kinetic energy distribution of aligned molecules. The  $I^+$  ions in the new high kinetic energy channel have an additional kinetic energy of up to  $\sim 0.4$  eV corresponding

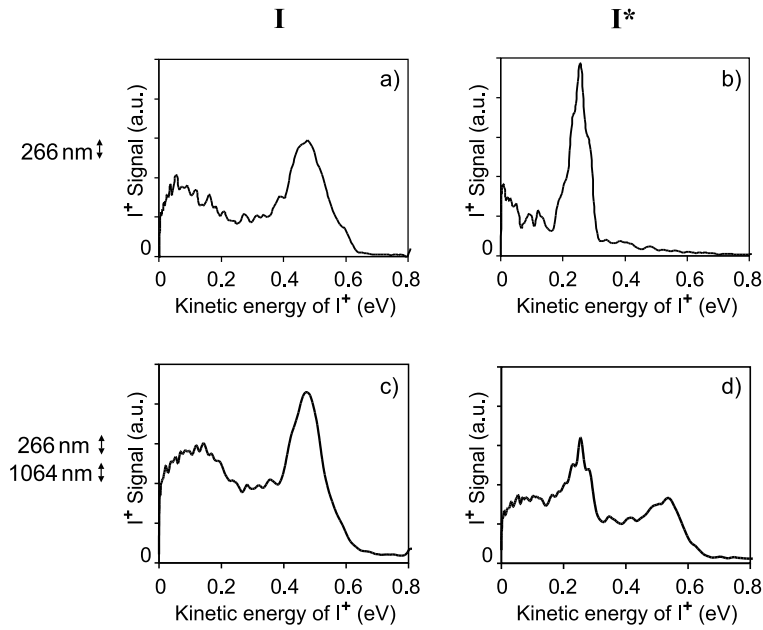


Figure 4.5: Kinetic energy distributions of  $I^+$  ions from REMPI of iodine photofragments. a+c) REMPI wavelength set to ionize ground state I, b+d) REMPI wavelength set to ionize  $I^*$ . a+b) Without alignment pulse, c+d) With alignment pulse.

to a total extra energy (of both fragments) of  $\sim 1.1$  eV, which is the energy of a 1064 nm photon.

#### 4.4.3 Angular distributions

Angular ( $\theta$ ) distributions (shown in fig. 4.6) can also be obtained from the Abel inverted images. The noise in the distributions stems from the Abel inversion.

Assuming the axial recoil approximation (sect. 4.3.3) and that the tran-

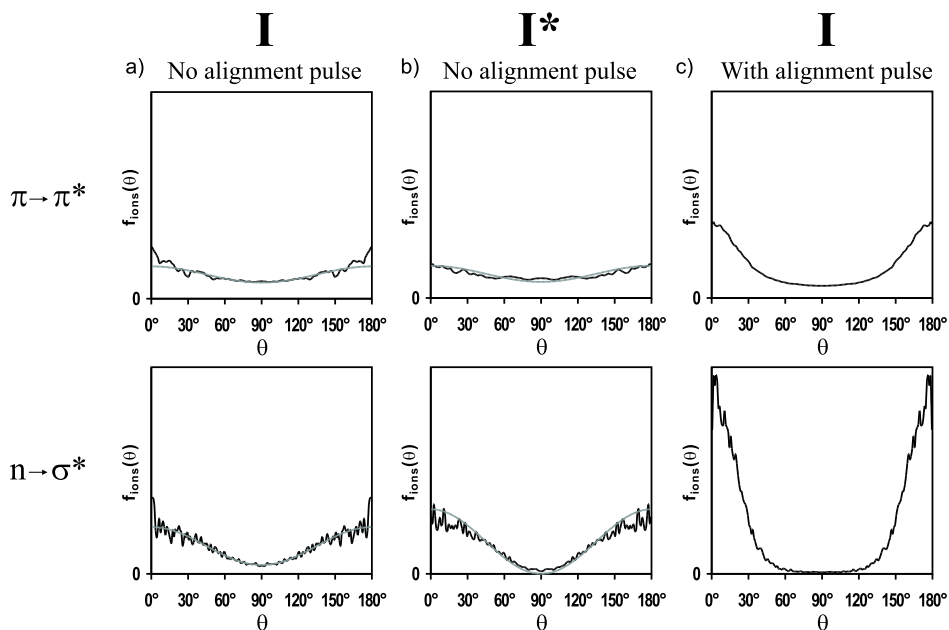


Figure 4.6: Angular distributions of  $I^+$  ions,  $f_{ions}(\theta)$ , from REMPI of I and  $I^*$  photofragments. Top row: Ions originating from the  $\pi \rightarrow \pi^*$  channel, bottom row: ions originating from the  $n \rightarrow \sigma^*$  channel. The black curves are the distributions obtained from the Abel inverted images, the gray curves are the dissociation probabilities derived in appendix C.2. a) REMPI of I, no alignment pulse, b) REMPI of  $I^*$ , no alignment pulse, c) REMPI of I, with alignment pulse.

sition is not saturated, the ion angular distributions originating from a uniform distribution of molecules must reflect the angular dependence of the dissociation probability. The expressions for the angular dependence were presented in the previous section and derived in appendix C.2. The gray curves in fig. 4.6 a) and b) show the distributions calculated with those expressions.

For the  $n \rightarrow \sigma^*$  channel (leading to ground state I)  $A = 0.84$  is obtained by fitting to the experimental distribution<sup>4</sup>. This corresponds to a transition, which is mainly parallel but has a minor perpendicular component, in agreement with the predictions of sect. 4.3.1.

The  $n \rightarrow \sigma^*$  angular distribution of  $I^*$  shown in fig. 4.6 b) is close to a pure parallel transition (gray curve). The deviations are due to noise, saturation, and deviation from the axial recoil approximation (molecules rotating slightly during dissociation).

The dissociation probability of the  $\pi \rightarrow \pi^*$  channel (eq. 4.2), which does not contain any fitting parameters, is reasonable close to the angular distributions of I and  $I^*$ . When the alignment pulse is included (fig. 4.6 c) a dramatic narrowing of the angular distributions of both dissociation channels is observed.

#### 4.4.4 Obtaining $f_{mol}(\theta)$ and $\langle \cos^2 \theta \rangle$

Assuming that the dissociation is not saturated the distribution of photofragments,  $f_{ions}$ , is proportional to the product of the molecular distribution prior to dissociation,  $f_{mol}$ , and the dissociation probability,  $P_{diss}$ ,

$$f_{ions}(\theta, \phi, \chi) \propto f_{mol}(\theta, \phi, \chi) P_{diss}(\theta, \phi, \chi). \quad (4.3)$$

For the  $n \rightarrow \sigma^*$  channel the dissociation probability only depends on the  $\theta$ -angle and eq. 4.3 can be reduced to

$$f_{ions}^{n \rightarrow \sigma^*}(\theta) \propto f_{mol}(\theta) P_{diss}^{n \rightarrow \sigma^*}(\theta). \quad (4.4)$$

We assume that the molecular distribution of the  $\theta$ -angle,  $f_{mol}(\theta)$ , is uniform when the alignment is not present and obtain  $P_{diss}^{n \rightarrow \sigma^*}(\theta)$  from the

<sup>4</sup> $A = 0.84$  correspond to  $\beta = 1.17$  (see eq. C.12)

ion angular distribution of the  $n \rightarrow \sigma^*$  channel of the unaligned image (fig. 4.6 a).  $f_{mol}(\theta)$  of the aligned molecules is obtained by dividing the angular distribution of the ions,  $f_{ions}^{n \rightarrow \sigma^*}(\theta)$ , with the dissociation probability,  $P_{diss}^{n \rightarrow \sigma^*}(\theta)$ , and normalizing.

Knowing the molecular distribution,  $f_{mol}(\theta)$ ,  $\langle \cos^2 \theta \rangle$  can be found using definition 2.4. Figure 4.7 shows  $\langle \cos^2 \theta \rangle$  obtained at different intensities of the alignment pulse and different backing pressures of the seed gas, helium. A higher backing pressure corresponds to a lower rotational temperature. The degree of alignment improves at lower rotational temperature and higher intensities as expected (sect. 2.2.2). It is evident in fig. 4.7 that the degree of alignment saturates at high intensities so that a further increase of the intensity does not cause a significant increase in  $\langle \cos^2 \theta \rangle$ .

In principle  $\langle \cos^2 \theta \rangle$  can also be calculated directly from the increase of ion yield in the  $n \rightarrow \sigma^*$  channel when the molecules are aligned. The ion yield,  $Y$ , is proportional to the dissociation probability averaged over all angles,  $\langle P_{diss} \rangle$  (once again assuming that the transition is not saturated). Dividing the ion yield of aligned molecules with that from a uniform distribution gives

$$\begin{aligned} \frac{Y_{align,para}^{n \rightarrow \sigma^*}}{Y_{noalign}^{n \rightarrow \sigma^*}} &= \frac{\langle P_{diss,para}^{n \rightarrow \sigma^*} \rangle}{\langle P_{diss,noalign}^{n \rightarrow \sigma^*} \rangle} = \frac{3}{2-A} (A \langle \cos^2 \theta \rangle + (1-A)(1 - \langle \cos^2 \theta \rangle)) \\ &\Downarrow \\ \langle \cos^2 \theta \rangle &= \frac{2-A}{6A-3} \frac{Y_{align,para}^{n \rightarrow \sigma^*}}{Y_{noalign}^{n \rightarrow \sigma^*}} + \frac{A-1}{2A-1}. \end{aligned} \quad (4.5)$$

However, experimental drift of the dissociation pulse energy, saturation, and the slight overlap of the two channels have so far excluded us from obtaining the yield ratio,  $Y_{align,para}^{n \rightarrow \sigma^*}/Y_{noalign}^{n \rightarrow \sigma^*}$ , with the precision required for eq. 4.5 to be useful.

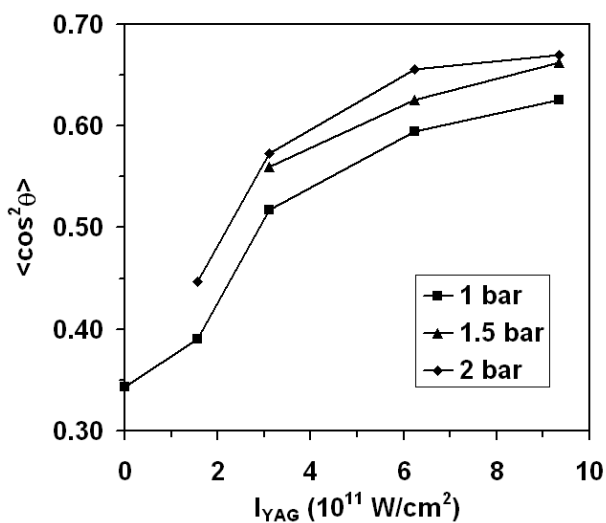


Figure 4.7:  $\langle \cos^2 \theta \rangle$  as a function of the peak intensity of the adiabatic alignment pulse,  $I_{YAG}$ , for iodobenzene molecules seeded in helium. Values for different backing pressures of helium are shown, a higher backing pressure corresponds to a lower rotational temperature. The lines between the points serve to guide to eye.

#### 4.4.5 Assumptions made for obtaining $\langle \cos^2 \theta \rangle$

Our method of obtaining  $\langle \cos^2 \theta \rangle$  is based on three basic assumptions: (1) That the molecular distribution is uniform when no alignment pulse is present, (2) that the  $n \rightarrow \sigma^*$  transition is not saturated, and (3) that the axial recoil approximation holds. We furthermore assume that the dissociation pulse is too fast and too weak to induce any significant degree of alignment during the pulse. Considering the intensity of the dissociation pulse, this is a good approximation even if the anisotropy of the molecular polarizability is a factor of 2–3 higher at 266 nm than at near infrared wavelengths.

### Collision induced alignment

As discussed in sect. 1.2.2 the molecules may be prealigned due to collision induced alignment in the supersonic expansion. Collision induced alignment is a confinement of the molecular rotation axis to the plane perpendicular to the molecular beam axis (fig. 4.8).

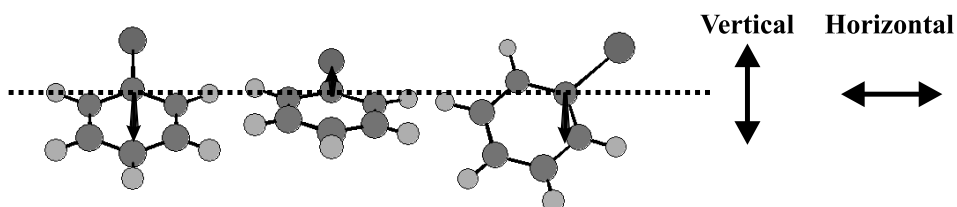


Figure 4.8: If the molecules experience collision induced alignment, the axis of rotation will be confined perpendicular to the beam axis.

If such a confinement is present the distribution in the  $\theta$ -angle,  $f_{mol}(\theta)$ , is still uniform, when the laboratory fixed Z-axis is perpendicular to the molecular beam axis (vertical polarization). The anisotropy caused by collision induced alignment is only affecting the distribution in the  $\phi$ -angle,  $f_{mol}(\phi)$ . When all laser polarizations are parallel along the Z-axis, the  $\phi$ -angle anisotropy is averaged out. Any degree of collision induced alignment is therefore not affecting the linear alignment experiments, in which all laser pulses have parallel polarizations perpendicular to the molecular beam.

For the sake of the following section on the control of the photodissociation, it is worth noting that if the laboratory fixed Z-axis is along the beam axis (horizontal polarization) there will be a weak confinement of the  $\theta$ -angle:  $\frac{1}{3} < \langle \cos^2 \theta \rangle < \frac{1}{2}$ . An increase in the yield of the mainly parallel  $n \rightarrow \sigma^*$  channel is therefore expected when changing from vertical to horizontal polarization of the dissociation pulse. We do not observe any such

yield increase for iodobenzene and therefore conclude that no significant degree of collision induced alignment is present for iodobenzene.

### Saturation

The next important assumption we have made is the assumption that the transition is not saturated. This assumption is equivalent to

$$\sigma\Phi_0 \ll 1, \quad (4.6)$$

where  $\sigma$  is the absorption cross section and  $\Phi_0$  is the photon flux of the dissociation pulse. In the experiment the peak intensity of the dissociation pulse was  $5 \times 10^{11}$  W/cm<sup>2</sup>. With a pulse duration of 1.5 ps, this corresponds to a (focal averaged) photon flux of  $42 \text{ \AA}^{-2}$ . The gas-phase absorption cross section (of iodobenzene) at 266 nm is  $2.3 \times 10^{-2} \text{ \AA}^2$  (appendix A). However, the cross section that should be considered for the  $\langle \cos^2 \theta \rangle$  determination is the cross section for the  $n \rightarrow \sigma^*$  transition leading to ground state I, which is less than 40% of the total cross section. So in our experiment  $\sigma_{n \rightarrow \sigma^*(I)} \Phi_0 \approx 0.4$ . This is high enough for weak saturation effects. Any saturation will be more pronounced for aligned than for uniformly distributed molecules since the yield is higher when the molecules are aligned. The angular distributions of ions from aligned molecules are thus broadened more than angular distributions of ions from a uniform distribution. The effect of saturation is therefore a lowering of the experimental  $\langle \cos^2 \theta \rangle$  value. The obtained  $\langle \cos^2 \theta \rangle$  values are thus lower estimates, the real values might be slightly higher.

### Axial recoil approximation

The last important assumption is that the axial recoil approximation holds, i.e. that the molecules do not rotate during the dissociation.

As stated in sect. 4.3.3 highly excited rotational states can rotate slightly during the fast  $n \rightarrow \sigma^*$  dissociation, causing broadening of the angular distributions and thus a slight lowering of the experimental  $\langle \cos^2 \theta \rangle$  values. Highly excited rotational states are mainly present in the very broad wave packets created by intense non-adiabatic alignment pulses. Deviations from the axial recoil approximation will lower the  $\langle \cos^2 \theta \rangle$  values most when the wave packets are broadest, which is also where the obtained degree of alignment is highest.

## 4.5 Controlling the photodissociation

The two dissociation channels have different geometry. The photodissociation can therefore be controlled by aligning the molecules to favor one dissociation channel over the other. By controlling the dissociation pathway the vibrational excitation of the phenyl radical is controlled. Dissociation through the  $\pi \rightarrow \pi^*$  channel gives the phenyl radical more vibrational excitation than dissociation through the  $n \rightarrow \sigma^*$  channel.

### 4.5.1 Control using linear Alignment

The ion images in fig. 4.9 a) and b) show what happens when the polarization of the dissociation pulse is changed from parallel to perpendicular to the linear alignment pulse polarization. Since the molecules are aligned the ions are still confined to the vertical alignment axis even though the dissociation pulse has horizontal polarization (fig. 4.9 b). The ions can therefore

still be separated in the two dissociation channels. The ion image with the perpendicular polarizations cannot be Abel inverted since it does not have cylindrical symmetry.

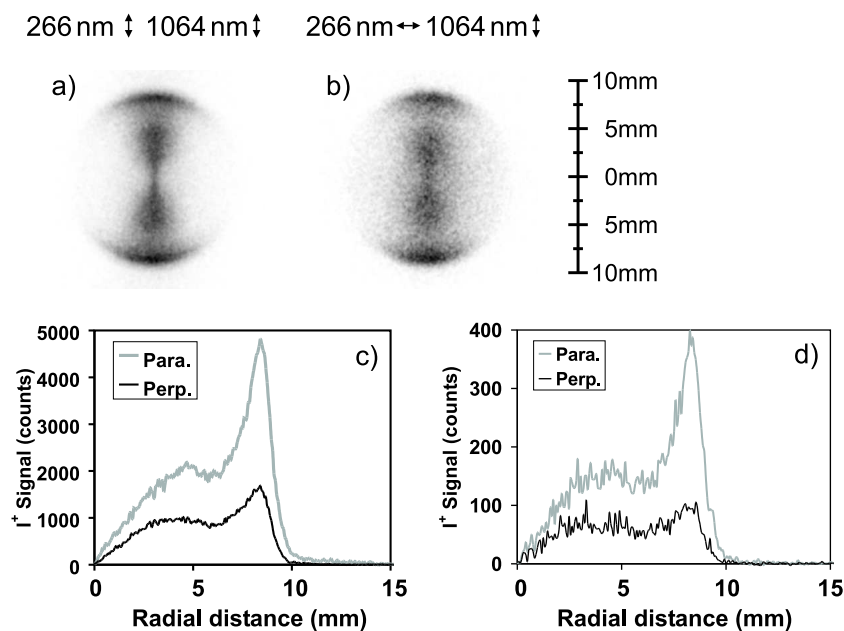


Figure 4.9: a+b) 2-D ion images of  $I^+$  ions from REMPI of I atoms produced by the photodissociation of iodobenzene seeded in 2 bar helium. a) Parallel polarizations of the alignment and dissociation pulses, b) Perpendicular polarizations of the alignment and dissociation pulses. c) Radial distributions of the 2-D ion images shown in the top row, d) Radial distributions obtained when seeding in 1 bar argon (images not shown).

The radial distributions of the two 2-D images are shown in fig. 4.9 c). Comparing the radial distributions it is seen that the ion yield of both dissociation channels is decreased going from parallel to perpendicular ge-

ometry. The ion yield is however decreased more in the mainly parallel  $n \rightarrow \sigma^*$  channel (a factor of 2.7) than in the planar  $\pi \rightarrow \pi^*$  channel (a factor of 2.0). When the iodobenzene molecules are seeded in argon instead of helium a lower rotational temperature is obtained, resulting in stronger alignment. The decreases in ion yield going from parallel to perpendicular geometry are therefore higher (factors of 3.4 and 2.6) when using argon as seedgas (fig. 4.9 d).

How much the ion yields are expected to be decreased can be calculated using the experimentally obtained distribution of aligned molecules,  $f_{mol}(\theta)$ . The number of ion hits in the images with argon as seedgas is low and the image therefore too noisy for Abel inversion.  $f_{mol}(\theta)$  can thus only be obtained when helium is used as seedgas. The peak intensity of the alignment pulse was  $9 \times 10^{11}$  W/cm<sup>2</sup> and  $\langle \cos^2 \theta \rangle = 0.68$  (fig. 4.7).

The ion yield,  $Y$ , is proportional to the dissociation probability averaged over the three Euler angles. Assuming  $f_{mol}$  to be uniform in  $\phi$  and  $\chi$ ,

$$Y \propto \langle P_{diss} \rangle = \int_0^\pi f_{mol}(\theta) P_{diss}(\theta) \sin \theta d\theta. \quad (4.7)$$

The expressions for dissociation probability,  $P_{diss}$ , of the two dissociation channels (averaged over  $\phi$ ) are shown in table 4.2 and derived in appendix C.2. Using the experimentally determined  $f_{mol}(\theta)$  and the dissociation probabilities of table 4.2 we calculate that going from parallel to perpendicular dissociation polarization the yield is decreased by a factor of 2.2 in the  $n \rightarrow \sigma^*$  channel and by a factor of 1.4 in the  $\pi \rightarrow \pi^*$  channel. The experimental factors were 2.7 and 2.0.

The discrepancies between the calculated values and the experimental results have two different causes. As mentioned in the previous section the requirement that the transition is not saturated is not completely fulfilled. This leads to an underestimate of the alignment and less difference between

| $n \rightarrow \sigma^*$ channel |  |
|----------------------------------|--|
| Parallel                         | $\sigma_{n \rightarrow \sigma^*} \Phi_0 \frac{3}{2-A} (A \cos^2 \theta + (1-A) \sin^2 \theta)$   |
| Perpendicular                    | $\sigma_{n \rightarrow \sigma^*} \Phi_0 \frac{3}{2-A} \left( \frac{1}{2} A \sin^2 \theta + (1-A) \left(1 - \frac{1}{2} \sin^2 \theta\right) \right)$ |

| $\pi \rightarrow \pi^*$ channel |  |
|---------------------------------|--|
| Parallel                        | $\sigma_{\pi \rightarrow \pi^*} \Phi_0 \frac{3}{2} (1 - \sin^2 \theta \sin^2 \chi)$                                    |
| Perpendicular                   | $\sigma_{\pi \rightarrow \pi^*} \Phi_0 \frac{3}{2} \left( \frac{1}{2} + \frac{1}{2} \sin^2 \theta \sin^2 \chi \right)$ |

Table 4.2: Dissociation probabilities (averaged over  $\phi$ ) of the two dissociation channels of iodobenzene. The dissociation pulse polarization is either parallel or perpendicular to the linear alignment pulse polarization (lab fixed Z-axis). Assuming a uniform  $\chi$ -distribution for all  $\theta$ ,  $\sin^2 \chi$  can be replaced by  $\frac{1}{2}$ .

parallel and perpendicular geometry. For the  $\pi \rightarrow \pi^*$  channel another factor also plays a role, the assumption of a uniform distribution of  $\chi$  for all  $\theta$  is not correct. A molecule at a given  $\theta \in (0, \pi)$  tends to align so that the alignment axis is in the molecular plane rather than out of the plane because the polarizability is higher in the plane than perpendicular to it. Therefore, there will be a weak localization of  $\chi$  around 0 and  $\pi$  (fig. 2.3 LP in sect. 2.2.1). This localization of  $\chi$  leads to higher yield in the  $\pi \rightarrow \pi^*$  channel for the parallel geometry and lower yield for the perpendicular geometry (cf. table 4.2).

### 4.5.2 Improving the control with 3-D alignment

As shown in the previous section we have obtained an amount of control of the photodissociation with linear alignment. However the best way to favor the  $\pi \rightarrow \pi^*$  channel is to use 3-D alignment to fix both the C-I bond axis and the molecular plane and then polarize the dissociation pulse in the molecular plane, perpendicular to the C-I bond axis. In that way the yield

of the  $n \rightarrow \sigma^*$  channel is minimized and the yield of the  $\pi \rightarrow \pi^*$  channel is maximized.

| Alignment (seedgas)              | $\frac{Y_{\pi \rightarrow \pi^*}}{Y_{n \rightarrow \sigma^*}}$ | $\frac{Y_{\pi \rightarrow \pi^*}}{Y_{n \rightarrow \sigma^*}}$ |
|----------------------------------|--|--|
|                                  | Parallel   | Perpendicular  |
| Uniform distribution             | 1.21   |  |
| Adiabatic, Linear (2 bar He)     | 1.01   | 1.35   |
| Adiabatic, Linear (1 bar Ar)     | 1.04   | 1.64   |
| Non-adiabatic, Linear (3 bar He) | 0.99   | 1.39   |
| Non-adiabatic, 3-D (3 bar He)    | 1.11   | 1.94   |

Table 4.3: Ratio of yields of the two dissociation channels of iodobenzene with the dissociation pulse polarization either parallel or perpendicular to the (major) alignment axis.

We have later<sup>5</sup> performed 3-D control experiments using an elliptically polarized 800 nm non-adiabatic alignment pulse ( $\tau_{FWHM} = 1.6$  ps,  $I_0 = 5 \times 10^{12}$  W/cm<sup>2</sup>). The results are compared with linear alignment in table 4.3. Using linear alignment and parallel dissociation polarization the yields in the two dissociation channels are the same. Using 3-D alignment and perpendicular dissociation polarization the yield of the  $\pi \rightarrow \pi^*$  channel is  $\sim 2$  times the yield of the  $n \rightarrow \sigma^*$  channel. We are thus able to tweak the ratio of yields from the two channels by a factor of 2.

In principle the  $n \rightarrow \sigma^*$  channel can be favored more by aligning the molecular plane (with circular alignment pulse polarization) and polarizing the dissociation pulse perpendicular to the alignment plane. With this scheme the planar  $\pi \rightarrow \pi^*$  channel is suppressed while the  $n \rightarrow \sigma^*$  channel survives due to its minor perpendicular component. As shown in fig. 4.10

<sup>5</sup>Unpublished data (2004).

this scheme is superior to linear alignment if a high degree of alignment is achievable. We can (currently) not perform this experiment as it requires two laser beams crossing at  $90^\circ$ .

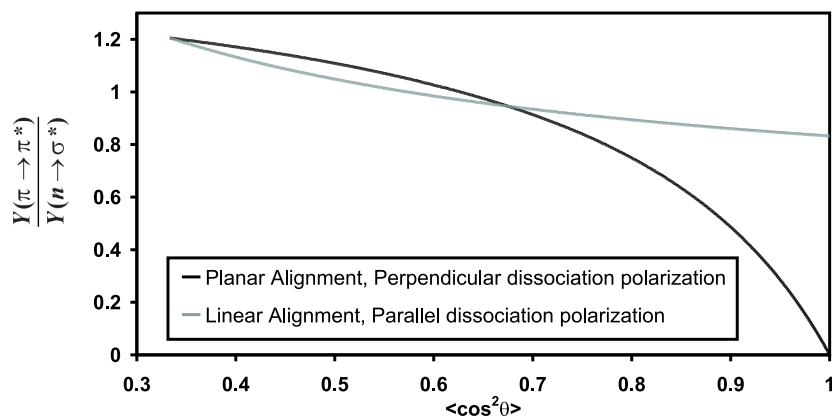


Figure 4.10: Calculation of the ratio of yields of the two dissociation channels of iodobenzene. Black curve: Alignment of the plane, dissociation polarization perpendicular to the alignment plane. Gray curve: Linear alignment of the C–I bond axis, dissociation polarization parallel to the the alignment axis ( $\chi$ -distribution assumed uniform for all  $\theta$ ). Note that  $\langle \cos^2 \theta \rangle$  is a measure of the alignment of two different axes: The C–I bond axis (linear alignment) or the axis perpendicular to the plane (planar alignment).

## 4.6 Conclusion

We have demonstrated a probe of molecular alignment that allow us to obtain the distribution of molecular orientations,  $f_{mol}(\theta)$ , and thus  $\langle \cos^2 \theta \rangle$  *prior* to dissociation by the probe. With this probe scheme we have mea-

sured the alignment of iodobenzene induced by an adiabatic alignment pulse at different rotational temperatures. The alignment improves with lower rotational temperature of the molecules and higher intensity of the alignment pulse. At high intensities the alignment saturates so that a further increase of the intensity only weakly enhances the alignment. The intensity is limited by the onset of multi photon ionization.

The iodobenzene molecule can be dissociated at 266 nm through two different channels. We have shown that linear alignment can be used as tool for controlling which channel the dissociation goes through and thereby the amount of vibrational excitation of the phenyl radical. The control can be improved by using 3-D alignment.

## Chapter 5

# Non-adiabatic alignment – short time dynamics

For many applications of alignment the unavoidable presence of the adiabatic alignment laser field is a major drawback. The alignment field might interfere in the process one wish to study. An example of this was presented in the previous chapter. The presence of the alignment field opened a new channel in the photodissociation of iodobenzene leading to the formation of  $I^*$  (sect. 4.4). With a short, non-adiabatic alignment pulse it is possible to have molecules aligned under field-free conditions. Field-free alignment is observed both immediately after the alignment pulse and at subsequent rotational revivals. This chapter will focus on the alignment observed immediately after the alignment pulse. The rotational revivals are treated in the next chapter.

In 1995, Seideman[61] published the first calculations on non-adiabatic alignment of linear molecules induced by a short intense laser pulse. That a short laser pulse can induce alignment was known long before but had

only been treated in the weak field limit, where the created wave packet is limited by the selection rules of the transition that produced it. Since then many theoretical papers have been published on strong laser field non-adiabatic alignment. Among them are quantum mechanical calculations on the dependence on alignment pulse duration[35, 37] and the effect of thermal averaging[35, 37, 39].

The first experimental observation of strong field non-adiabatic alignment was presented by Rosca-Pruna and Vrakking in 2001[62, 63, 64]<sup>1</sup>. They used a short intense probe pulse to Coulomb explode aligned I<sub>2</sub> molecules and velocity map imaging to study the angular distribution of the ion fragments. Later, other groups also presented strong field non-adiabatic alignment experiments. Dooley et al.[31] used a similar probe to study the non-adiabatic alignment of N<sub>2</sub> and O<sub>2</sub> and Renard et al.[30] probed the non-adiabatic alignment of CO<sub>2</sub> by measuring transient birefringence.

Common to all the works mentioned above is that they pertain to linear molecules. We wished to apply non-adiabatic alignment on a much more general class of molecules, asymmetric top molecules. The results presented in this chapter are all concerned with the asymmetric top iodobenzene molecule. The short time dynamics are especially important for asymmetric top molecules since the alignment of asymmetric top molecules is strongest immediately after the alignment pulse[5].

At first the possibility of obtaining field-free alignment was our main reason to study non-adiabatic alignment. It was therefore important for us to find the conditions where the highest degree of alignment is obtained under

---

<sup>1</sup>In 1999 and 2000 Frey et. al.[65, 66] presented degenerate four-wave mixing (DFWM) experiments that can be viewed as strong field laser induced alignment. However, the authors did not interpret the data as strong field alignment but used weak field, perturbative methods.

field-free conditions. Another attractive feature of the non-adiabatic alignment regime compared to adiabatic alignment is that there are more parameters available for improving the alignment. In an adiabatic alignment experiment there is essentially only one parameter for a given ensemble of molecules at a given rotational temperature – the intensity. In the previous chapter it was shown that the alignment saturates at higher intensities, so that an increase of intensity only gives a small increase of the degree of alignment (fig. 4.7). Furthermore, the intensity cannot be increased beyond the threshold for multi photon ionization<sup>2</sup>. In the non-adiabatic case using a sequence of alignment pulses can enhance the alignment beyond the limit to the alignment obtainable by a single alignment pulse.

## 5.1 Alignment with one pulse

### 5.1.1 Experiment

The probe scheme of the experiment is the same as the adiabatic alignment experiment: dissociation of aligned iodobenzene molecules by a 266 nm pulse and subsequent selective ionization of either I or I\* with a 304 nm REMPI pulse. The adiabatic alignment pulse is replaced by a picosecond non-adiabatic alignment pulse. The pulses involved in the experiment are illustrated in fig. 5.1.

The alignment pulses used in the first experiments were stretched to 1.9–2.7 ps by double passage through two prisms. In the later experiments the prisms were replaced by a grating stretcher, which produced smoother temporal profiles and facilitated an easy adjustment of the pulse duration

---

<sup>2</sup>Since the multi photon ionization process is highly non-linear (at least six 800 nm photons are required to ionize iodobenzene), it scales with a high order of the intensity and thus has a threshold like behavior.

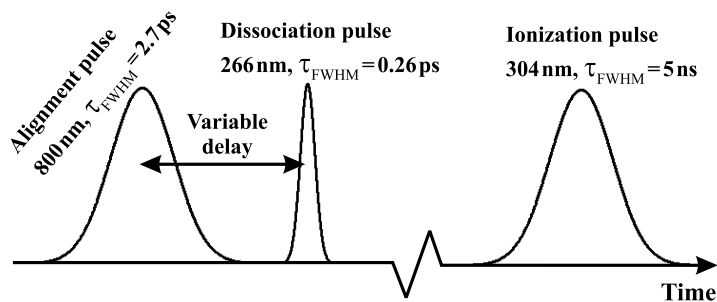


Figure 5.1: The pulses involved in the non adiabatic alignment experiments on iodobenzene.

(sect. 3.2.2).

Since the alignment depends on the delay between the alignment and dissociation pulses, adequate time-resolution is needed. The 266 nm dissociation pulses were therefore compressed to 260 fs. The peak intensity was  $2 \times 10^{12}$  W/cm<sup>2</sup>. In the adiabatic alignment experiment the pulses were stretched to 1.5 ps because the presence of the alignment pulse enhanced direct dissociative ionization. In this experiment the alignment and dissociation pulses do not coincide in time. The 266 nm pulses were later stretched to 400–500 fs to minimize ions produced by dissociative ionization of the 266 nm pulse alone.

The ionization pulse wavelength was initially set to ionize I\* (303.96 nm). The absorption cross section is smaller for the  $n \rightarrow \sigma^*$  transition leading to I\* than for the  $n \rightarrow \sigma^*$  transition leading to I, the transition is therefore not saturated even though the intensity of the dissociation pulse is high. For the later experiments (pulse duration, two pulse alignment, and rotational revivals) the ionization pulse wavelength was set to ionize I (304.59 nm). In those experiments the 266 nm pulses were longer ( $\sim 400$  fs) and the intensity lower, ensuring saturation could be avoided.

### 5.1.2 Ion images and $\langle \cos^2 \theta \rangle$

Figure 5.2 shows ion images recorded at different delays between the 1.9 ps alignment pulse and the dissociation pulse. The intensity of the alignment pulse was kept under the threshold for multi photon ionization. When the molecules are dissociated prior to the alignment pulse (fig. 5.2 b), the image is similar to the image without the alignment pulse (fig. 5.2 a). When the alignment and dissociation pulses coincide in time (fig. 5.2 c) the ion image is dominated by high kinetic energy ions. The high kinetic energy ions are produced in an ionization process involving photons from both alignment and dissociation pulses. In the ion image recorded immediately after the alignment pulse is over (fig. 5.2 d), a significant angular confinement along the (vertical) alignment axis is observed. We interpret this confinement as molecular alignment. Note that this alignment occurs under field-free conditions. At longer delays the alignment goes to a local minimum (fig. 5.2 e) and a weak local maximum (fig. 5.2 f) before stabilizing at a weak permanent level. Much later rotational revivals are observed as demonstrated in the next chapter.

As described in sect. 4.4.3 the molecular distribution prior to dissociation,  $f_{mol}(\theta)$ , and  $\langle \cos^2 \theta \rangle$  can be obtained from the ion images. As in sect. 4.4.3, a background image recorded without the ionization pulse is subtracted to account for the ions produced directly by the dissociation pulse. When the alignment and dissociation pulses do not coincide in time this background is small, 10–15%. However, when there is temporal overlap the ‘background’ ions comprise up to 75% of the total ion hits. To account for experimental fluctuations of the dissociation pulse energy, the background images were scaled so that the high-kinetic energy part of image and background image matched (only background ions reside in the high kinetic energy part of the image). The background subtracted images

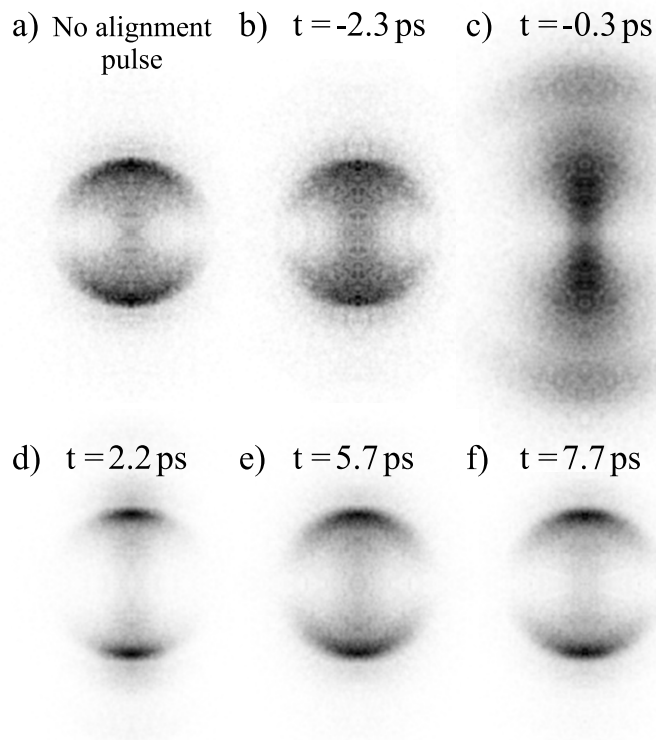


Figure 5.2: Ion images of  $I^*$  photo fragments of iodobenzene dissociated at different times,  $t$ , compared to the peak of the 1.9 ps non-adiabatic alignment pulse. a) No alignment pulse, b)  $t = -2.3$  ps, c)  $t = -0.3$  ps, d)  $t = 2.2$  ps, e)  $t = 5.7$  ps, f)  $t = 7.7$  ps.

were Abel inverted and divided by the probe selectivity to obtain  $f_{mol}(\theta)$ , from which  $\langle \cos^2 \theta \rangle$  was obtained.

Figure 5.3 shows both the  $f_{mol}(\theta)$  distribution and the obtained  $\langle \cos^2 \theta \rangle$  values. Note that during the alignment pulse (-1.5 to 1.5 ps) the calculation significantly underestimates  $\langle \cos^2 \theta \rangle$  since direct ionization from the com-

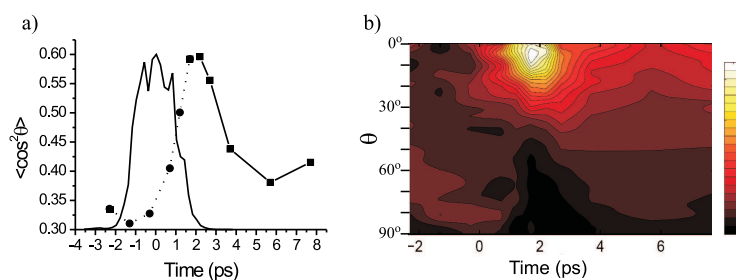


Figure 5.3: Alignment of iodobenzene by a 1.9 ps (FWHM) 800 nm pulse with a peak intensity of  $3.4 \times 10^{12}$  W/cm<sup>2</sup>. a) Cross correlation trace of the alignment pulse (full curve) and  $\langle \cos^2 \theta \rangle$  values obtained from the ion images (squares, lines between points included to guide the eye). During the alignment pulse the  $\langle \cos^2 \theta \rangle$  values are significantly underestimated, these are marked with circles and connected with dotted lines. b)  $f_{mol}(\theta)$  calculated from the ion images.

binated dissociation and alignment pulses depletes the best aligned molecules. The small dip of  $\langle \cos^2 \theta \rangle$  in the beginning of the alignment pulse is an artefact created by this effect. The strongest alignment in terms of  $\langle \cos^2 \theta \rangle$  is reached at  $t \approx 2.1$  ps with  $\langle \cos^2 \theta \rangle = 0.59$ . The most pronounced confinement of  $f_{mol}(\theta)$  is reached slightly earlier at  $t \approx 1.8$  ps. The exact determination of the timing of the peak of alignment is thus dependent on which measure is used (cf. sect. 2.1.2).

### 5.1.3 Dependence on intensity and rotational temperature

Figure 5.4 illustrates how non-adiabatic alignment depends on the intensity of the alignment pulse and on the rotational temperature of the sample molecules.

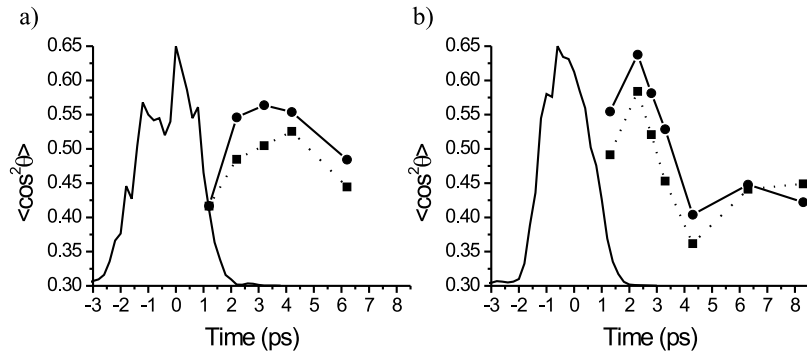


Figure 5.4:  $\langle \cos^2 \theta \rangle$  values from ion images of aligned iodobenzene molecules seeded in 3 bar helium (circles connected by solid lines) and 1 bar helium (squares connected by dotted lines). The connecting lines serve to guide the eye. A higher seedgas pressure corresponds to a lower rotational temperature. Also shown is the cross correlation trace of the alignment pulse (full curve). a) Alignment pulse peak intensity,  $I_0 = 1.0 \times 10^{12}$  W/cm<sup>2</sup>, b) Alignment pulse peak intensity,  $I_0 = 3.4 \times 10^{12}$  W/cm<sup>2</sup>.

### Intensity dependence

Comparing fig. 5.4 a) and b) it is seen that a lowering of the intensity decreases the maximum obtained degree of alignment. Furthermore, the dynamics become slower, the alignment reaches its maximum later, and the molecules are aligned for a longer time.

These result agree with the argument that a higher intensity of the alignment pulse creates a broader wave packet resulting in stronger alignment. With more states in the wave packet the dephasing becomes faster. In classical terms the increased angular momentum corresponds to an increased angular velocity.

Figure 5.5 shows a quantum mechanical calculation of the alignment

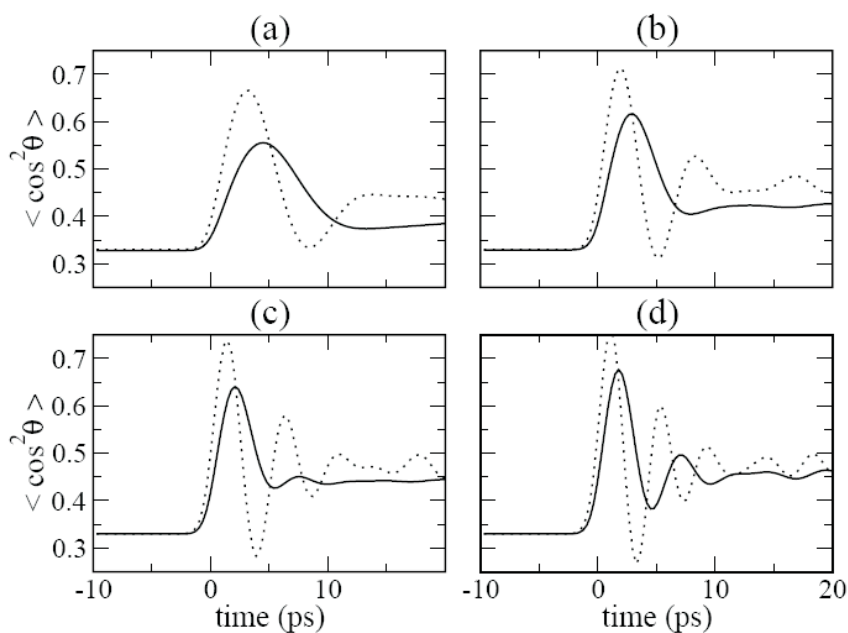


Figure 5.5: Calculated alignment dynamics of iodobenzene at 2.4 K for different peak intensities of the alignment pulse. The calculation was averaged over the different intensities present in the focal volume of the probe pulse (solid lines). The corresponding dynamics without focal averaging is overlaid as a dotted line. The peak intensities are: a)  $1 \times 10^{12} \text{ W/cm}^2$ , b)  $2 \times 10^{12} \text{ W/cm}^2$ , c)  $3 \times 10^{12} \text{ W/cm}^2$ , d)  $4 \times 10^{12} \text{ W/cm}^2$ . The alignment pulse peaks at  $t = 0$  and has a duration of 2.7 ps.

dynamics induced by a 2.7 ps long alignment pulse. The calculation illustrates the same intensity effect as the experiment: When the intensity is increased the maximum obtained degree of alignment is increased and the dynamics become faster. Note that there is a significant difference between the calculated alignment curve with and without focal averaging of the intensity. In the experiment the focal spot size of the dissociation pulse is

a factor of 1.5 smaller than the spot size of the alignment pulse. Averaging over the alignment intensities present in the focus of the dissociation pulse shortens the duration of the initial alignment peak and significantly dampens the oscillations following the first peak of alignment.

### Dependence on the rotational temperature

The rotational temperature can be decreased by increasing the pressure of the seed gas. Comparing the  $\langle \cos^2 \theta \rangle$  values obtained at two different seed gas pressures, it is seen that a decrease of the rotational temperature gives a higher degree of alignment with only small changes to the dynamics. The highest degree of alignment is reached at the same time and drops off with the same speed.

Figure 5.6 shows a quantum mechanical calculation of the alignment dynamics at different rotational temperatures. The calculation shows the same effect of an increase in the rotational temperature: a decrease of the obtained alignment and only small changes to the dynamics (the alignment peak becomes slightly narrower at higher temperatures). The curve corresponding to a rotational temperature of 2.4 K is quite close to the experimental curve obtained when the molecules are seeded in 3 bar helium (fig 5.4 a). The rotational temperature of the experiment is not accurately known. Comparing with the calculation we conclude that iodobenzene seeded in 3 bar helium obtain a rotational temperature of 2–3 K.

#### 5.1.4 Alignment pulse duration

Another very important parameter for the degree of alignment is the pulse duration. For a given pulse duration the peak intensity of the alignment pulse must be low enough that direct multi photon ionization by the align-

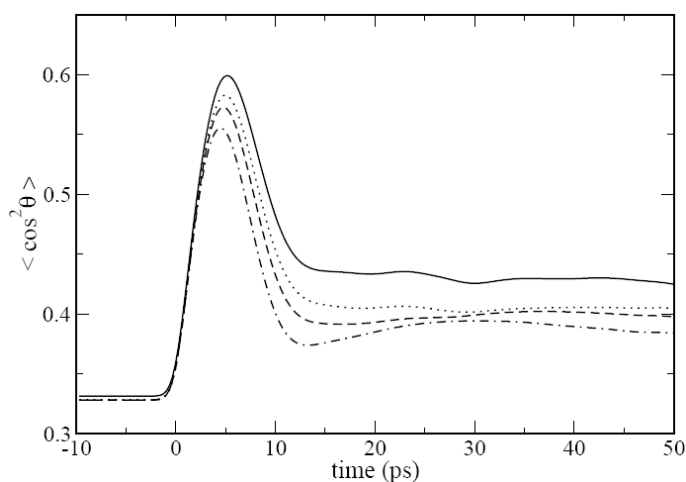


Figure 5.6: Calculated Alignment dynamics of iodobenzene at different rotational temperatures following a 2.7 ps alignment pulse centered at  $t = 0$  for a focal averaged peak intensity of  $1 \times 10^{12}$  W/cm<sup>2</sup>. The calculation was averaged over the different intensities present in the focal volume of the probe pulse. The rotational temperature was: 0 K (solid), 0.4 K (dotted), 1.2 K (dashed), 2.4 K (dot-dashed).

ment pulse is negligible. Figure 5.7 shows the alignment dynamics of iodobenzene following non-adiabatic alignment pulses with different pulse durations. The intensity of each alignment pulse was chosen to be as high as the molecules could tolerate, i.e. just below the threshold for multi photon ionization. In practice this was ensured by keeping the background ion signal from multi photon ionization by the alignment pulse constant at a very low value. The pulse energy was higher for the longer pulses (though the peak intensity was lower).

This experiment was done as part of the experiments regarding the comparison and combination of adiabatic and non-adiabatic alignment (chapter 7). The probe pulse was therefore an ultrashort 20 fs intense 800 nm

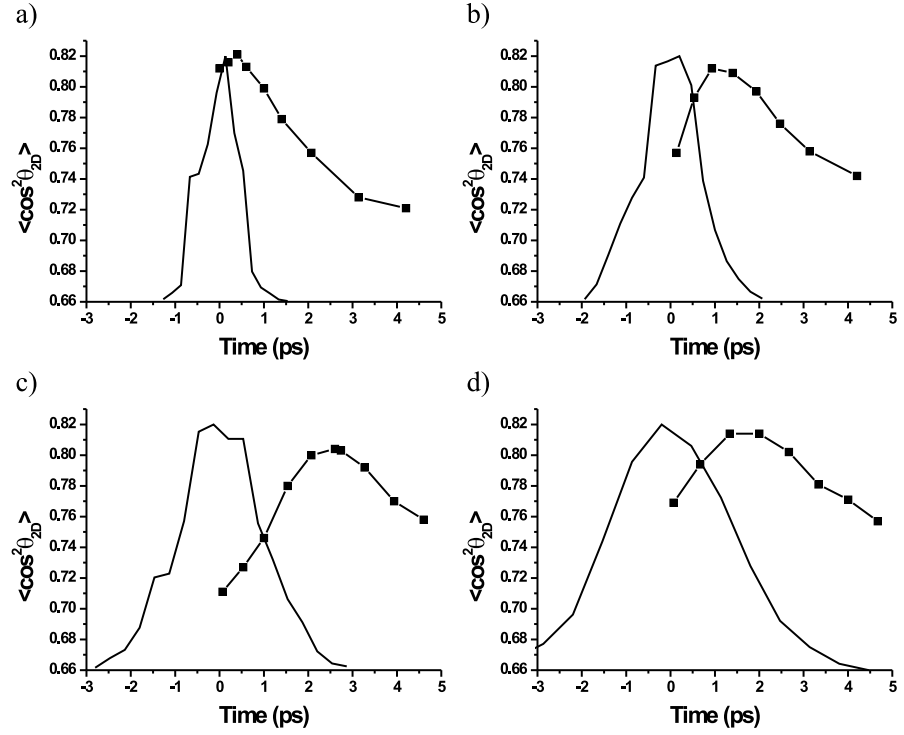


Figure 5.7: Alignment of iodobenzene,  $\langle \cos^2 \theta_{2D} \rangle$ , induced by alignment pulses with different durations (the lines between the points serve to guide the eye). Also shown are the cross correlation traces of the alignment pulses (full curves). The peak intensity of the alignment pulses was chosen so that the background ion signal from multi photon ionization by the alignment pulse was kept constant at a very low level. The alignment was probed with a 20 fs Coulomb explosion pulse (see sect. 7.1), without alignment pulse  $\langle \cos^2 \theta_{2D} \rangle = 0.65$ . a)  $\tau_{\text{FWHM}} = 1.1 \text{ ps}$ ,  $I_0 = 6.9 \times 10^{12} \text{ W/cm}^2$ , b)  $\tau_{\text{FWHM}} = 1.5 \text{ ps}$ ,  $I_0 = 6.2 \times 10^{12} \text{ W/cm}^2$ , c)  $\tau_{\text{FWHM}} = 2.1 \text{ ps}$ ,  $I_0 = 5.8 \times 10^{12} \text{ W/cm}^2$ , d)  $\tau_{\text{FWHM}} = 3.1 \text{ ps}$ ,  $I_0 = 4.9 \times 10^{12} \text{ W/cm}^2$ .

pulse that Coulomb explodes the molecules (see sect. 7.1). With this probe  $\langle \cos^2 \theta \rangle$  cannot be obtained and  $\langle \cos^2 \theta_{2D} \rangle$  measured directly on the ion image was therefore used as a qualitative measure of alignment. For this probe  $\langle \cos^2 \theta_{2D} \rangle = 0.65$  when no alignment pulse is present.

The maximum obtained degree of alignment is almost the same for all pulse durations in fig. 5.7,  $\langle \cos^2 \theta_{2D} \rangle \approx 0.81$ . Note that an even shorter duration ( $< 1$  ps) will induce a weaker alignment as the pulse energy in that case has to be significantly decreased to avoid multi photon ionization. It is only for the 2.1 ps pulse the peak occurs after the alignment pulse under field-free conditions. For the other pulse durations the alignment peak occurs during the pulse (though close to field-free conditions for the 1.5 ps pulse<sup>3</sup>). The timing of the peak of the alignment is not in agreement with the predictions of the simple classical kicked rotor model (sect. 2.3.2). The reason is that the pulses at these high intensities are too long to be considered a “sudden kick”.

We conclude that a pulse duration of 1.5–2.5 ps is optimal for obtaining field-free alignment of iodobenzene. Using a longer or shorter pulse, the intensity must be decreased to delay the alignment peak causing a lower degree of alignment<sup>4</sup>. Alternatively pulse shaping[67, 68] can be employed to ensure a steep decline of alignment pulse so that the alignment peaks under field-free conditions.

In all the experiments presented in this thesis the alignment pulses

---

<sup>3</sup>The volume probed by the Coulomb explosion probe is much smaller than that of the dissociation probe. Thus the average intensity is higher causing a slightly earlier peak of alignment than observed with the dissociation probe. When the dissociation probe is used the alignment induced by a 1.5 ps pulse peaks under field-free conditions.

<sup>4</sup>For pulses shorter than those of this experiment the alignment peaks under field-free conditions but the intensity has to be significantly decreased resulting in weaker alignment.

have had negative chirp. We do not expect the chirp to play a role as the spectral width of the alignment pulse ( $\Delta\nu \approx 5$  THz) is much larger than required for the Raman transitions responsible for creating the wave packet ( $\sim 1$ –500 GHz). This assumption was tested by investigating the short time dynamics and the first rotational revival of alignment induced by a 1.4 ps alignment pulse with either positive or negative chirp. The observed differences were well within the experimental uncertainties.

## 5.2 Alignment with two pulses

### 5.2.1 Idea

As stated in the last section the intensity of the alignment pulse is limited by the onset of multi photon ionization. To overcome this problem Averbukh and coworkers [69, 41, 42] suggested to use a train of short pulses rather than just one alignment pulse. Using the quantum mechanical kicked rotor model (sect. 2.2.3) they calculated optimal delays and intensities for alignment of a linear molecule using two or three alignment pulses. With two alignment pulses the calculations for molecules initially at  $T = 0$  K predicted that the second pulse should be fired close to the peak of the alignment induced by the first pulse and the intensity of the second pulse should be approximately a factor of 10 higher than the first pulse. At higher rotational temperatures more intensity is required in the first pulse.

The basic idea of using more than one alignment pulse is readily understood from the classical kicked rotor model (sect. 2.3.2). The first alignment pulse forces a large number of molecules into the angular range where  $\sin(\theta) \approx \theta$ . The second pulse ‘kicks’ the molecules with an impulse proportional to  $\theta$  causing the molecules to align, i.e. reach  $\theta = 0$  at the same time.

### 5.2.2 Experiment

The experiments presented here show that the non-adiabatic alignment of iodobenzene can be strongly enhanced by using two alignment pulses instead of one. The results are published in [4].

The two alignment pulses have parallel linear polarizations and both have a duration of 1.4 ps. This is the shortest duration of the alignment pulse, for which the alignment induced by an intense pulse is still peaking under almost field-free conditions (cf. fig. 5.7). By choosing relatively short alignment pulses interference effects at short delays between the pulses can be avoided.

We use our usual probe scheme of dissociation with a 266 nm pulse followed by resonantly enhanced multi photon ionization and extract  $\langle \cos^2 \theta \rangle$  from the ion images.

### 5.2.3 Alignment dynamics

We have mainly investigated the short time dynamics of the two-pulse alignment scheme, since our primary motivation for using two pulses is to enhance the alignment. The strongest alignment (for an asymmetric top molecule) is found shortly after the alignment pulse[5]. Averbukh and coworkers[41, 42] proposed to fire the second pulse at a rotational revival. Their calculations were done on a linear molecule, which has perfect recurrences at the rotational revivals. This scheme was used in the two-pulse experiment on N<sub>2</sub> by Lee et al.[70], which was published simultaneous with our two-pulse experiment.

Figure 5.8 shows experimental  $\langle \cos^2 \theta \rangle$  values at different times obtained with one or two alignment pulses. The first (weak) alignment pulse has a peak intensity of  $1.4 \times 10^{12}$  W/cm<sup>2</sup>. The second (strong) alignment

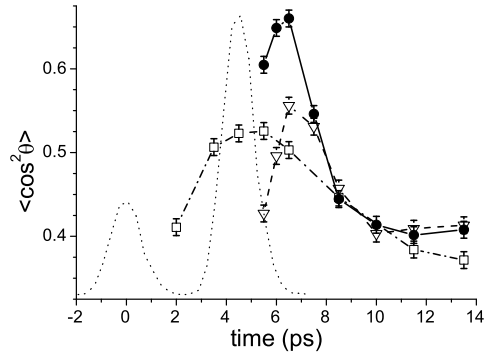


Figure 5.8:  $\langle \cos^2 \theta \rangle$  vs. time for the first pulse only (squares), the second pulse only (triangles), and both pulses (filled circles). The lines serve to guide the eye. The intensity shapes (cross correlation traces) of the alignment pulses are given by the dotted line (arb. units).

pulse is delayed 4.5 ps with respect to the first and has a peak intensity of  $4.1 \times 10^{12}$  W/cm<sup>2</sup>. When only the first weak alignment pulse is used (squares) the degree alignment peaks at  $\langle \cos^2 \theta \rangle = 0.52$  close to  $t = 5$  ps, after which it drops off to a permanent level at  $\langle \cos^2 \theta \rangle \approx 0.37$ . When only the second strong alignment pulse is used the alignment dynamics is faster and the degree of alignment peaks at  $\langle \cos^2 \theta \rangle = 0.56$  only  $\sim 2$  ps after the peak of the alignment pulse, in agreement with the results presented in the previous section. When both alignment pulses are used the alignment still peaks  $\sim 2$  ps after the peak of the second alignment pulse but now  $\langle \cos^2 \theta \rangle = 0.66$ . The obtained degree of alignment is thus significantly higher with two alignment pulses than with the second strong pulse alone. Note that the high degree of alignment is reached under field-free conditions.

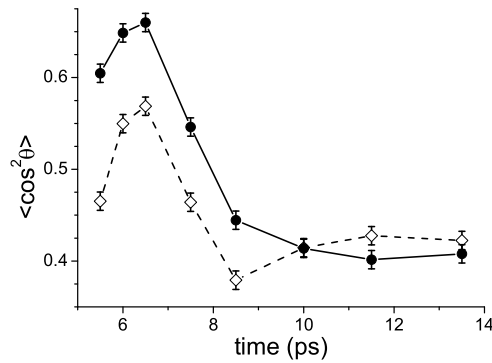


Figure 5.9: The alignment dynamics due to a single pulse (centered at  $t = 4.5$  ps) with a peak intensity of  $5.5 \times 10^{12}$  W/cm<sup>2</sup> (diamonds) and due to the two-pulse sequence illustrated in fig. 5.8 (filled circles). The lines between the points serve to guide the eye. The total energy of the two-pulse sequence as the same as the energy of the single intense pulse.

To ensure that the enhancement of alignment is not an effect of the extra pulse energy of the two-pulse experiment we also investigated the dynamics following a single alignment pulse with peak intensity  $5.5 \times 10^{12}$  W/cm<sup>2</sup> (fig. 5.9). This pulse has the same pulse energy as the total energy of the two-pulse sequence. For the single intense pulse the alignment peaks at  $\langle \cos^2 \theta \rangle = 0.57$ , much lower than with the two-pulse scheme and only 0.01 higher than the alignment obtained with a peak intensity of  $4.1 \times 10^{12}$  W/cm<sup>2</sup>. The intensity cannot be increased more without causing multi photon ionization of the molecules. A stronger alignment can therefore not be obtained by increasing the intensity of the alignment pulse. By distributing the available pulse energy in two pulses we have thus surpassed the limit to the alignment imposed by the maximum intensity a molecule can be

exposed to without causing ionization.

### 5.2.4 Pulse to pulse delay

The calculations of Averbukh and coworkers[41, 42] predicted that the second pulse should be fired close to the peak of the alignment induced by the first. The timing of the pulse sequence in fig. 5.8 was therefore chosen so that the second pulse was fired at the peak of the alignment induced by the first. To investigate the effect of the relative timing of the two alignment pulses, we measured  $\langle \cos^2 \theta \rangle$  2 ps after the second pulse for different pulse to pulse delays. We chose to measure 2 ps after the second pulse because the strongest field-free alignment is found at this time (cf. fig. 5.8).

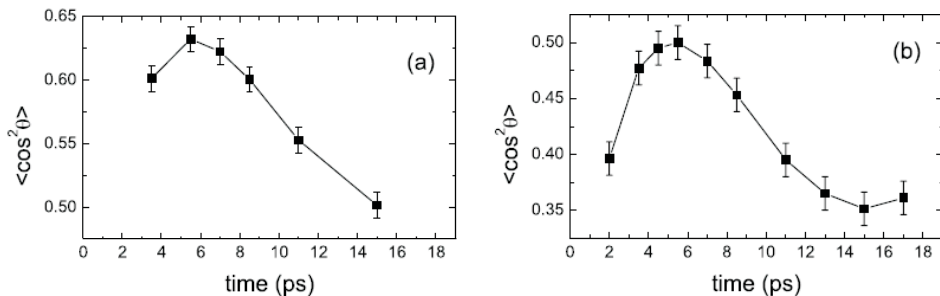


Figure 5.10: a)  $\langle \cos^2 \theta \rangle$  measured 2 ps after the second pulse as a function of the delay between the two alignment pulses. The peak intensity of the first pulse is  $1.4 \times 10^{12}$  W/cm<sup>2</sup>, the peak intensity of the second pulse is  $4.1 \times 10^{12}$  W/cm<sup>2</sup>. b)  $\langle \cos^2 \theta \rangle$  obtained with the first pulse only. The data displayed in this figure were recorded at a higher rotational temperature than fig. 5.8 and 5.9 and the obtained degree of alignment is therefore lower.

Figure 5.10 a) shows the strongest field-free alignment obtained with a two-pulse sequence as a function of the delay between the pulses. The best

degree of alignment is reached when the second pulse is fired approximately 5.5 ps after the first. Figure 5.10 b) shows the alignment obtained with the first pulse only. The alignment induced by the first pulse peaks at 5.5 ps. The prediction that the second pulse should be fired close to the peak of the alignment induced by the first is thus confirmed.

### 5.2.5 Intensity ratio, $I_1/I_2$

For the data displayed in fig. 5.10 an intensity ratio of the alignment pulses,  $I_1/I_2 = 1/3$ , was used. We have also investigated the dependence of the pulse to pulse delay for other intensity ratios. In all cases we found that the optimal field-free alignment occurs approximately 2 ps after the peak of the second pulse and when the second pulse is sent at or slightly after the peak of the alignment induced by the first pulse. These observations are summarized in fig. 5.11 where the optimal degree of alignment at different  $I_1/I_2$  ratios are displayed. The total pulse energy is the same for all pulse sequences.

As seen from fig. 5.11 the highest degree of alignment is obtained when the second pulse is 3–5 times more intense than the first.

### 5.2.6 Discussion

By splitting the pulse energy in two pulses the alignment was enhanced to  $\langle \cos^2 \theta \rangle = 0.66$  under field-free conditions. The strongest alignment obtained in the adiabatic regime was  $\langle \cos^2 \theta \rangle = 0.68$ . Using two-pulse non-adiabatic alignment we have thus obtained molecules almost as strongly aligned as in the adiabatic regime but under field-free conditions. This makes two-pulse non-adiabatic alignment the favorable choice for obtaining strongly aligned molecules unless the molecules need to be aligned for longer

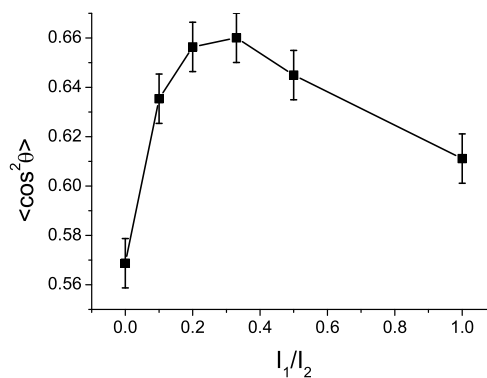


Figure 5.11: Optimal degree of field-free double pulse alignment, measured 2 ps after the peak of the second pulse, as a function of the intensity ratio,  $I_1/I_2$ , for a fixed total energy. For  $I_1/I_2 = 0$ ,  $I_2 = 5.5 \times 10^{12}$  W/cm<sup>2</sup> and for  $I_1/I_2 = 1$ ,  $I_1 = I_2 = 2.6 \times 10^{12}$  W/cm<sup>2</sup>.

time than a few picoseconds.

The two-pulse scheme treated in this section can be regarded as one case of a generalized pulse sequence with variable duration, timing, intensity, and polarization of the pulses tailored to achieve the strongest possible alignment of one or more molecular axes. Efforts to optimize such pulse sequences are ongoing.

### 5.3 Conclusion

We have demonstrated field-free non-adiabatic alignment of the asymmetric top iodobenzene molecule and investigated the dependence on the intensity and duration of the alignment pulse and on the rotational temperature of the molecules. With higher intensity the molecular alignment becomes

stronger and the dynamics faster. The presence of different intensities in the focus of the probe pulse significantly dampens oscillations after the first alignment peak. To ensure that the alignment of iodobenzene peaks under field-free conditions the duration of a high intensity alignment pulse should be 1.5–2.5 ps. For a shorter or longer pulse the alignment peaks during the alignment pulse. Lowering the rotational temperature result in a higher degree of alignment with only small changes to the dynamics.

We have have furthermore shown that the alignment can be significantly enhanced by distributing the available pulse energy in two alignment pulses instead of one. The strongest alignment is obtained when the second pulse is timed at or slightly after the peak of the alignment induced by the first pulse and when the second pulse is 3–5 times more intense than the first.

## Chapter 6

# Non-adiabatic alignment – Rotational revivals

The revivals of alignment that appear in non-adiabatic alignment experiments bear strong similarities with the rotational recurrences of rotational wave packets created by weak fields.

The ability of a short laser pulse to create a rotational wave packet that exhibit revivals has been known the past 30 years. Already in the seventies, Lin and coworkers showed both theoretically[71] and experimentally[72] that a wave packet created by exciting  $\text{CS}_2$  molecules with a short pulse exhibits “susceptibility echoes”, rotational revivals, at regular intervals spaced by  $1/4B$ ,  $B$  being the rotational constant (in MHz). Also non-linear molecules exhibit rotational revivals at regular intervals determined by the rotational constants. The spectrum of rotational revivals can thus be used to measure rotational constants. This time resolved rotational spectroscopical method is known as Rotational Coherence Spectroscopy (RCS)[18, 19].

RCS has been performed on rotational wave packets both in an elec-

---

tronic excited state created through a resonant transition and on ground state rotational wave packets created through a non-resonant Raman process[73, 19], as it is done in strong laser field non-adiabatic alignment experiments. Until recently all RCS methods used weak fields to create the rotational wave packet. Weak field induced wave packets are limited by the selection rules of a single transition and the spectra can be simulated with perturbative methods. However, a recently developed method of RCS, time resolved degenerate four wave mixing (TRDFWM)[65, 66, 19], employs strong fields. In TRDFWM experiments two simultaneous pump pulses are focused on the sample at different angles generating a transient grating. The measured signal is the diffraction of a delayed probe pulse.

The number and complexity of the molecules studied with various weak field RCS methods is high[18, 19]. In contrast rotational revivals in the strong field limit have (except for our experiments) only been investigated for linear molecules. Our aim was to investigate the rotational revivals of symmetric and asymmetric top molecules and to bridge the gap between Rotational Coherence Spectroscopy and strong field non-adiabatic alignment.

The results on rotational revivals presented in this chapter pertain to three different classes of molecules: symmetric tops, asymmetric tops of  $C_{2v}$ -type (where the principal axes of polarizability and inertia coincide), and asymmetric tops of general type. They are presented here in that order, although chronologically the experiments on asymmetric tops of  $C_{2v}$ -type were done first. Those results are published in [5]. The results on symmetric tops will be published as [6].

## 6.1 Experiment

The probe of alignment in the revival experiments is the same as in the previous chapters, dissociation at 266 nm and subsequent ionization of ground state iodine fragments.

Our usual method for obtaining  $\langle \cos^2 \theta \rangle$  is rather time consuming since it requires a background image without the ionization pulse and a high number of ion hits in both images to reduce the noise of the Abel inversion. To be able to measure alignment at a large number of different delays within a reasonable data acquisition time we have used another measure of alignment,  $\langle \cos^2 \theta_{2D} \rangle$ .  $\theta_{2D}$  is measured directly on the 2-D image without Abel inversion. A uniform distribution of ion hits has  $\langle \cos^2 \theta_{2D} \rangle = \frac{1}{2}$ . However, without Abel inversion it is impossible to deconvolute the probe selectivity. The measured  $\langle \cos^2 \theta_{2D} \rangle$  values will thus also reflect the probe selectivity. As a result the  $\langle \cos^2 \theta_{2D} \rangle$  value obtained for a uniform distribution is molecule dependent. Furthermore, small differences in the experimental conditions on different days might result in small differences between the  $\langle \cos^2 \theta_{2D} \rangle$  value obtained for a uniform distribution in different data series on the same molecule. Even with these reservations,  $\langle \cos^2 \theta_{2D} \rangle$  is still a good qualitative measure of the alignment in the sense that a higher  $\langle \cos^2 \theta_{2D} \rangle$  corresponds to a stronger alignment, a higher  $\langle \cos^2 \theta \rangle$ . The standard deviation of the measured  $\langle \cos^2 \theta_{2D} \rangle$  values is small,  $\sim 0.003$ . However, due to the long data acquisition times, a slight drift of the experimental conditions is often observed.

## 6.2 Symmetric top molecules

We have studied two symmetric top molecules: methyl iodide ( $\text{CH}_3\text{I}$ ) and tert-butyl iodide ( $(\text{CH}_3)_3\text{I}$ ). The observed spectra of rotational revivals have the same features for both molecules – transients at regular intervals of  $1/(4B)$ , with  $B$  being the rotational constant.

### 6.2.1 Ion images

Figure 6.1 shows ion images of I photofragments from methyl iodide molecules seeded in argon recorded at different times,  $t$ , with respect to the peak of an alignment pulse with a duration of 0.75 ps and a peak intensity of  $1.3 \times 10^{13}$  W/cm<sup>2</sup>.

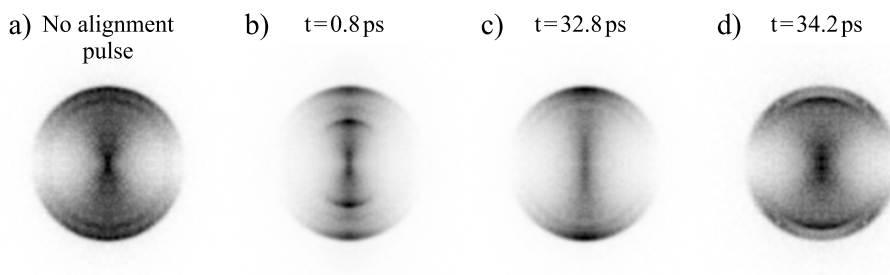


Figure 6.1: Ion images of I photofragments from methyl iodide molecules recorded at different times,  $t$ , with respect to the peak of the alignment pulse ( $\tau_{FWHM} = 0.75$  ps,  $I_0 = 1.3 \times 10^{13}$  W/cm<sup>2</sup>). a) No alignment pulse present, b)  $t = 0.8$  ps, c)  $t = 32.8$  ps, d)  $t = 34.2$  ps.

The ion image recorded without alignment pulse (fig. 6.1 a) has two rings, both of which are angularly confined along the vertical laser polarization axis. The outermost ring originates from molecules dissociated by the 266 nm pulse ( $n \rightarrow \sigma^*$  transition). The inner ring originates from

molecules dissociated by the 304 nm ionization pulse, which was kept at a high intensity. The appearance of this extra inner ring has no consequence for the experiment. Since the rings are clearly separable  $\langle \cos^2 \theta_{2D} \rangle$  and  $\langle \cos^2 \theta \rangle$  can be extracted from the radial region outside the inner ring. The number of ion hits in the ring originating from dissociation by the 304 nm pulse is the same for all the images in fig. 6.1. The ring appears to have different intensity in the images of fig. 6.1 because the images are scaled to the most intense part. When the alignment pulse is included, the molecules align immediately after the pulse (fig. 6.1 b). The two extra low kinetic energy rings that appear in fig. 6.1 b) stem from dissociation and ionization processes involving the alignment pulse, they are observed because the alignment field is not completely gone. The alignment observed immediately after the pulse quickly decays (within 2–3 ps) and the degree of alignment is then constant at a low permanent level ( $\langle \cos^2 \theta \rangle = 0.39$ ) until the first rotational revival appear at  $t \approx 34$  ps. A physical explanation of this permanent alignment is given in sect. 2.2.2. At the first rotational revival the degree of alignment first reach a local maximum (fig. 6.1 c) after which it quickly drops to a local minimum (fig. 6.1 d). Note that the image in fig. 6.1 d) is less confined along the vertical axis than the image without alignment pulse (fig. 6.1 a) indicating that the molecules are confined to the plane perpendicular to the alignment axis (due to the selectivity of the vertically polarized dissociation probe the density of the ring in the ion image is highest at  $\sim 45^\circ$ ).

### 6.2.2 Revival spectra

To quantify the alignment dynamics and the rotational revivals  $\langle \cos^2 \theta_{2D} \rangle$  was calculated from ion images of aligned methyl iodide molecules seeded in helium recorded at delays 1–75 ps (fig. 6.2 a). The transient at very early

time correspond to the alignment obtained immediately after the pulse. This alignment quickly dephases and the degree of alignment is then constant except for two rotational revivals observed close to 34 and 67 ps. Close to the transients of alignment we also measured  $\langle \cos^2 \theta_{2D} \rangle$  on images recorded with argon as seedgas (fig. 6.2 b–d). The rotational temperature is lower with argon as seedgas. At selected times high statistics ion images like those shown in fig. 6.1 were recorded and  $\langle \cos^2 \theta \rangle$  extracted from those images.

Since the molecules are field free from  $t > 1$  ps the alignment dynamics hereafter are determined solely by molecular rotation. The timing of the rotational revivals can readily be understood from the rotational energies of a prolate symmetric top in the rigid rotor approximation,

$$E_{rot}(J, K, M) = BJ(J + 1) + (A - B)K^2, \quad (6.1)$$

where  $A$  and  $B$  are the rotational constants and  $J$ ,  $K$ , and  $M$  are the symmetric top rotational quantum numbers. The energies are degenerate in  $M$ .

The selection rules for a rotational Raman transition in a symmetric top molecule (table 2.2) are  $\Delta J = 0, \pm 1, \pm 2$  and  $\Delta K = 0$ . All the states in the rotational wave packet created by the alignment pulse will thus share the same  $K$  quantum number. The energy difference between different states in the wave packet is therefore always a multiple of  $2B$ . A full rephasing of the wave packet is thus expected at regular intervals of  $t_J = 1/(2B)^1$ . Halfway between these revivals the wave packet is localized in the opposite direction causing a local minimum of the alignment. For methyl iodide  $t_J = 66.655$  ps (appendix A). We can thus identify the transient at  $\sim 67$  ps

<sup>1</sup> $t_J = 1/(2B)$  with  $B$  in MHz,  $t_J = 1/(2Bc)$  with  $B$  in  $\text{cm}^{-1}$ , and  $t_J = \pi/(2B)$  in atomic units.

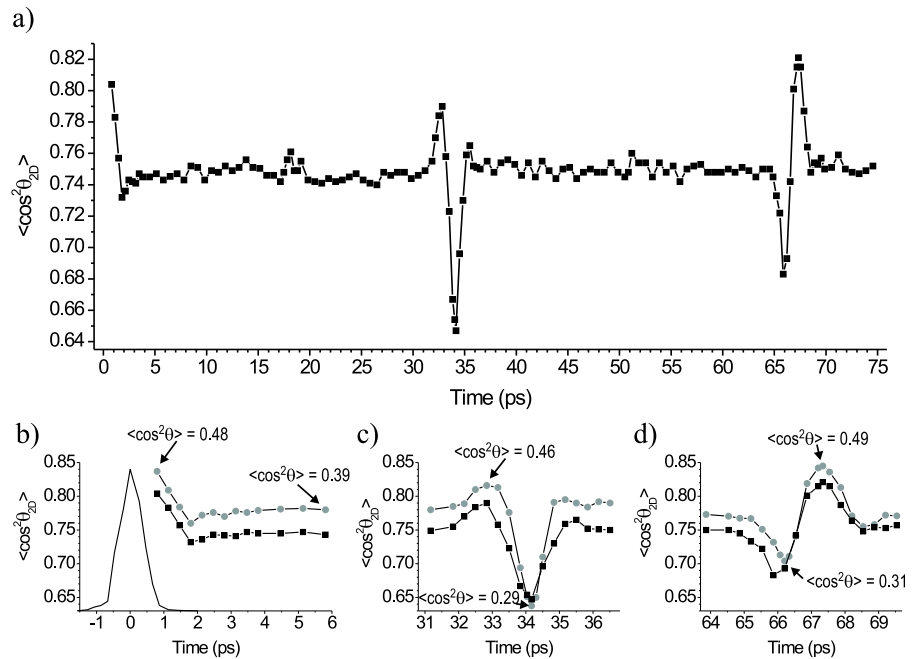


Figure 6.2: Alignment of methyl iodide seeded in helium (black squares), measured as  $\langle \cos^2 \theta_{2D} \rangle$  as a function of time after the peak of the alignment pulse. Lines between points included to guide the eye. a) Long time scan, b–d) Transients in the alignment. In b–d) are also shown  $\langle \cos^2 \theta_{2D} \rangle$  for methyl iodide seeded in argon (grey circles). The  $\langle \cos^2 \theta \rangle$  values are calculated from high statistics ion images (with argon as seedgas) recorded at selected times (some of them shown in fig. 6.1). The cross correlation trace of the alignment pulse ( $\tau_{FWHM} = 0.75$  ps,  $I_0 = 1.3 \times 10^{13}$  W/cm<sup>2</sup>) is shown in b) (full curve). The alignment pulse intensity was the maximum, the molecules could tolerate. With no alignment pulse present  $\langle \cos^2 \theta_{2D} \rangle = 0.71$ .

as the first full revival and the transient at  $\sim 34$  ps as a half revival.

The results presented in fig. 6.2 confirm that the alignment present

immediately after the pulse is fully reestablished at the full revival. The relatively modest degree of alignment obtained,  $\langle \cos^2 \theta \rangle = 0.49$ , has two causes: the polarizability anisotropy of methyl iodide is modest,  $\Delta\alpha = \alpha_{\parallel} - \alpha_{\perp} = 2.6 \text{ \AA}^3$  and the duration of the alignment pulse is not optimized for obtaining the strongest alignment (see sect. 6.2.3). Note that  $\langle \cos^2 \theta \rangle < \frac{1}{3}$  at the half revival, corresponding to the molecular axis being confined in the plane perpendicular to the alignment axis.

Full recurrence of the alignment at the full rotational revivals requires two assumptions to be met: The molecules must travel in a collision-free environment and the rigid rotor approximation must hold. The low translational temperature and low density of the sample molecules ensure a collision-free environment. Deviation from the rigid rotor approximation due to centrifugal distortion will change the shape and amplitude of the revivals but not affect the permanent alignment, which is due to a localization of the axis of rotation. To investigate the changes to the rotational revivals on a longer timescale, we measured the alignment close to selected full revival times (fig. 6.3).

The dynamics of the first two revivals (fig. 6.3 a–b) is essentially identical. From the fourth revival (fig. 6.3 c) the amplitude starts to drop. At the eighth and 16th revivals (fig. 6.3 d–e) the amplitude drops even more and small changes to the general shape of the transient are visible. The maximum delay of the dissociation pulse in the optical setup is  $\sim 3 \text{ ns}$ , so the last revival we could measure was the 42nd (fig. 6.3 f). At the 42nd revival the amplitude has dropped even more and significant changes in the shape of the transient are observed, the rise and fall have become slower. No significant change of the permanent alignment was observed. We thus ascribe the changes to the shape of the revivals to centrifugal distortion.

To confirm the generality of our results on the rotational revival spectra

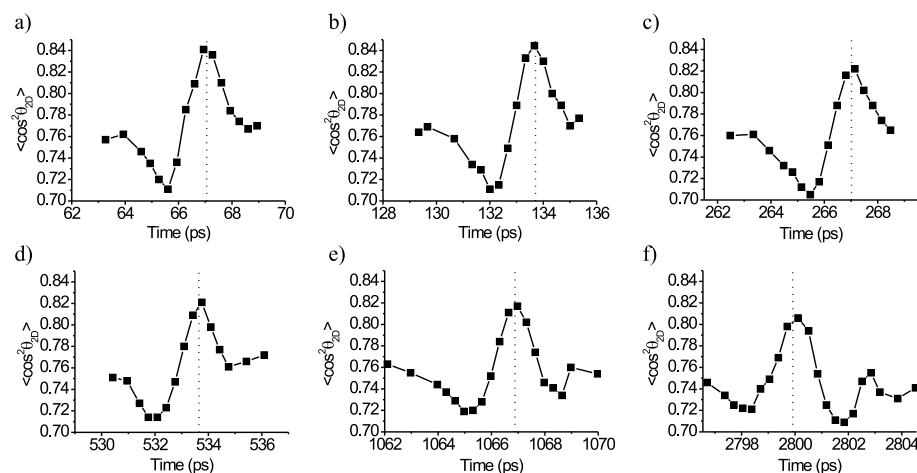


Figure 6.3: Alignment dynamics of methyl iodide seeded in argon (black squares connected by lines to guide the eye) near selected full rotational revival times. a) 1st full revival, b) 2nd full revival, c) 4th full revival, d) 8th full revival, e) 16th full revival f) 42nd full revival. The dotted vertical lines indicate predicted revival times  $t = n/(2B) + 0.4$  ps,  $n$  being the revival number.

of symmetric top molecules, we also performed the experiment on another prolate symmetric top molecule, tert-butyl iodide (fig. 6.4).

As seen in fig. 6.4 the rotational revival spectrum of tert-butyl iodide is very similar to the spectrum of methyl iodide. The alignment obtained immediately after the pulse quickly dephases to the level of the permanent alignment where it is constant except for two narrow transients occurring close to  $1/(4B)$  and  $1/(2B)$ , the half and full rotational revivals. The only difference from the methyl iodide spectrum is that the alignment is not fully reestablished at the full revival. We assume this difference is due to centrifugal distortion playing larger role for this molecule than for methyl

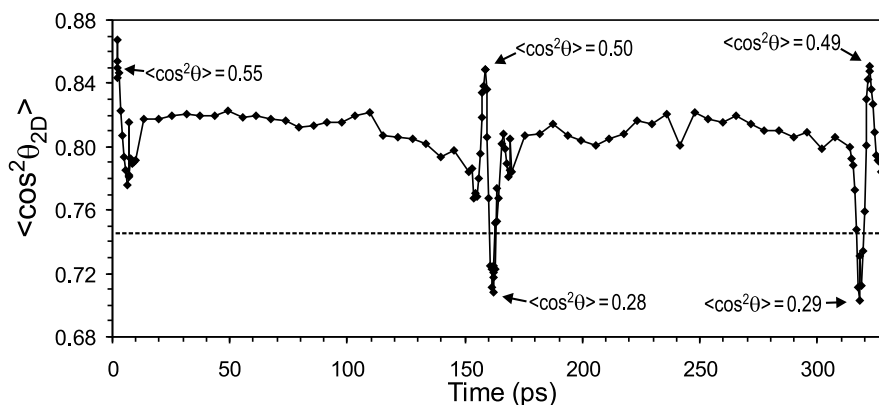


Figure 6.4: Alignment of tert-butyl iodide seeded in helium (black diamonds connected by lines to guide the eye) measured as  $\langle \cos^2 \theta_{2D} \rangle$  as a function of time after the peak of the alignment pulse ( $\tau_{FWHM} = 1.1$  ps,  $I_0 = 1.0 \times 10^{13}$  W/cm<sup>2</sup>). The dashed horizontal line indicates  $\langle \cos^2 \theta_{2D} \rangle$  without alignment pulse. The  $\langle \cos^2 \theta \rangle$  values are calculated from high statistics ion images.

iodide<sup>2</sup>. We have observed that the amplitude of the second full revival (not shown) is considerably lower than the first, which confirms this assumption.

The spectrum of rotational revivals of symmetric top molecules are very similar to those of linear molecules. The rotational energies of linear molecules are described by setting  $K = 0$  in eq. 6.1. It is therefore not surprising that linear molecules also have full revivals at regular intervals of  $1/(2B)$  and half revivals in between. Some linear molecules also exhibit quarter revivals at odd multiples of  $1/(8B)$ . The reason is that the Ra-

<sup>2</sup>Since tert-butyl iodide has a smaller rotational constant the average  $J$ ,  $\langle J \rangle$ , is higher compared to methyl iodide. The centrifugal distortion term,  $-D_J J^2 (J+1)^2$ , is very sensible to  $J$ .

man selection rule for linear molecules is  $\Delta J = 0, \pm 2$ . The rotational wave packet will thus only consist of states with either even or odd  $J$ . At quarter revival times even- $J$  and odd- $J$  wave packets are oppositely localized[31]. Quarter revivals will thus be averaged out in a sample with the same number of molecules in even and odd  $J$  states. However, for molecules belonging to the  $D_{\infty h}$  pointgroup the population of odd or even  $J$  states is affected by nuclear spin statistics and these molecules usually have an uneven distribution of odd vs. even  $J$  states resulting in observable quarter revivals. That is the case for  $O_2$  and  $N_2$ [31, 65], for  $CO_2$ [30, 65], and for  $I_2$ [62].

The revival spectra showed in fig. 6.2 and fig. 6.4 are similar to typical weak field RCS spectra except for two important differences. The first difference is that the first alignment maximum is not reached at  $t = 0$  but shortly after. The second difference is the permanent alignment observed between the transients. These effects are not present in the perturbative limit. TRDFWM spectra have so far been simulated using weak field theory. However, a background signal constant in time but depending on the laser intensity has been observed in TRDFWM spectra recorded by Riehn and coworkers[74, 75]. They accounted for this effect by introducing an *ad hoc* parameter,  $k$ , whose “physical meaning is still unclear” [74]. We believe this background signal is due to permanent alignment. The short delay between the peak of alignment pulse and the first alignment maximum occurring immediately after the pulse result in a small time-shift on the revivals compared to  $t = 0$ . Perturbative simulations of TRDFWM spectra do not account for this time-shift and it seems to be negligible in those experiments, although it is striking that the rotational constants extracted from perturbative simulations of TRDFWM experiments usually are slightly lower than those obtained from standard microwave spectroscopy[65, 66, 74, 75], as expected if a small time-shift is not accounted for.

### 6.2.3 Duration of the alignment pulse

The shape and amplitude of the rotational revivals depend very much on the duration of the alignment pulse. To investigate how the duration of the alignment pulse affects the rotational revivals we measured the alignment of methyl iodide at the first full revival for different durations of the alignment pulse (fig. 6.5). The pulse energy,  $E_{pulse}$ , was kept constant at 120  $\mu\text{J}$ . The product of the pulse duration and peak intensity,  $\tau I_0$ , is thus the same for all alignment pulses. As seen from fig. 6.5 the difference between minimum and maximum alignment is highest for the shortest pulses (fig. 6.5 a–b). However, the strongest alignment is achieved for the somewhat longer duration of 1.1 ps (fig. 6.5 c). For even longer durations (fig. 6.5 d–e) the dynamics become slower and the alignment weaker.

The shortest alignment pulses approach the “sudden kick” limit where the molecules do not rotate during the interaction with the alignment. In this limit there is no phase lag between different states in the wave packet resulting in a rotational revival with a fast dynamic and high amplitude, i.e. high difference between minimum and maximum alignment. It is however interesting that the strongest alignment is reached for a longer pulse. We believe this observation can be explained by the argument used to explain the enhanced alignment obtained when the alignment pulse is split in two (sect. 5.2). When the alignment pulse is long enough that the molecules can rotate during the interaction the first part of the alignment pulse can prealign the molecules and thereby enhance the alignment induced by the remaining part of the pulse. When the duration of the alignment pulse becomes too long the adiabatic limit is approached. The slow decay of the alignment pulse will then destroy the alignment.

We can thus conclude that alignment with a very short pulse gives the narrowest transient with the highest modulation. A short pulse is thus

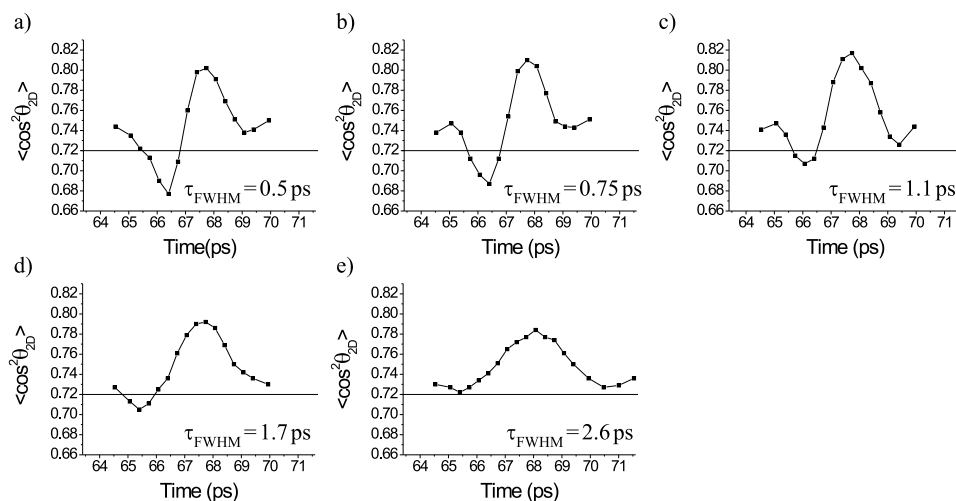


Figure 6.5: Alignment of methyl iodide seeded in helium (black squares connected by lines to guide the eye), measured as  $\langle \cos^2 \theta_{2D} \rangle$  at times close to the first full rotational revival. The durations of the alignment pulses,  $\tau_{\text{FWHM}}$ , were: a) 0.5 ps, b) 0.75 ps, c) 1.1 ps, d) 1.7 ps, e) 2.6 ps. The energy,  $E_{\text{pulse}}$ , of the alignment pulse was kept constant at  $120 \mu\text{J}$ , this corresponds to a peak intensity of the shortest (0.5 ps) pulse of  $1.6 \times 10^{13} \text{ W/cm}^2$ . The horizontal lines indicate  $\langle \cos^2 \theta_{2D} \rangle$  without alignment pulse.

preferable for spectroscopic purposes where one is interested in the timing of the revivals rather than the obtained degree of alignment. However, a somewhat longer pulse (1.1 ps) is preferable when the strongest alignment is wanted. Note that the pulse energy was chosen so that the intensity of the shortest pulses were the maximum tolerable by molecules. For the longer pulses the intensity can be increased slightly resulting in stronger alignment.

To confirm the generality of our results we performed a similar pulse

duration experiment on tert-butyl iodide (fig. 6.6). In this experiment the intensity was the maximum tolerable by the molecules for all durations of the alignment pulse. The pulse energy was therefore slightly increased for the longer pulses.

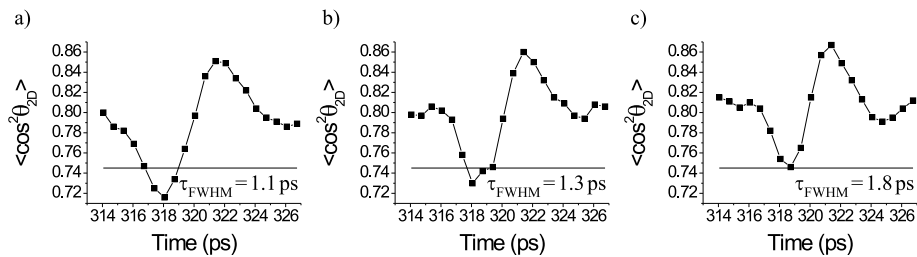


Figure 6.6: Alignment of tert-butyl iodide seeded in helium (black squares connected by lines to guide the eye), measured as  $\langle \cos^2 \theta_{2D} \rangle$  at times close to the first full rotational revival. The durations of the alignment pulses,  $\tau_{\text{FWHM}}$ , were: a) 1.1 ps, b) 1.3 ps, c) 1.8 ps. The energy,  $E_{\text{pulse}}$ , of the alignment pulse was increased slightly with the pulse duration, so that the intensity was kept at the maximum tolerable by the molecules. The peak intensities were: a)  $1.0 \times 10^{13} \text{ W/cm}^2$ , b)  $9 \times 10^{12} \text{ W/cm}^2$ , c)  $6 \times 10^{12} \text{ W/cm}^2$ . The horizontal lines indicate  $\langle \cos^2 \theta_{2D} \rangle$  without alignment pulse.

The dependence of the alignment on the pulse duration for tert-butyl iodide (fig. 6.6) is similar to the observations on methyl iodide. The modulation of the transient is highest for the shortest alignment pulses (fig. 6.6 a–b) but a stronger alignment is achieved with a longer alignment pulse (fig. 6.6 c).

### 6.3 Asymmetric top molecules of $C_{2v}$ type

The rotational energies of asymmetric top molecules cannot be described by a simple formula like eq. 6.1 for symmetric top molecules. As a consequence the question of when revivals occur and how strong they are, is non-trivial. To investigate the revival spectra of asymmetric top molecules of  $C_{2v}$  type, we performed alignment experiments on the iodobenzene and iodopentafluorobenzene molecules. The results are confirmed by quantum mechanical calculations.

#### 6.3.1 Revival spectra

To investigate the revival spectrum of an asymmetric molecule we recorded low statistics ion images of iodobenzene molecules subject to a 2.7 ps alignment pulse ( $I_0 = 4 \times 10^{12}$  W/cm<sup>2</sup>) with delays of the dissociation pulse in the range 0–800 ps. The ion images were similar to those shown in fig. 5.2.  $\langle \cos^2 \theta_{2D} \rangle$  values calculated from the ion images are shown in fig. 6.7.

As seen before the alignment reached immediately after the pulse quickly dephases and the degree alignment drops to the level of the permanent alignment as for the symmetric top molecules. Hereafter the degree of alignment is essentially constant except for three prominent and very narrow transients. The strongest transients occur close to 378 and 756 ps. A weak transient also appears close to 703 ps. In order to quantify the alignment high statistics ion images were recorded close to the transients and  $\langle \cos^2 \theta \rangle$  extracted from these images. The results are shown in fig. 6.8.

I will focus first on the timing of the revivals. The alignment maximum after the pulse is reached at  $t = 2.0$  ps (fig. 6.8 a) and the three subsequent transients are centered at 378.8 ps, 702.7 ps, and 755.9 ps respectively (fig. 6.8 b–d). As the molecules are field free from  $\sim 2$  ps the timing of

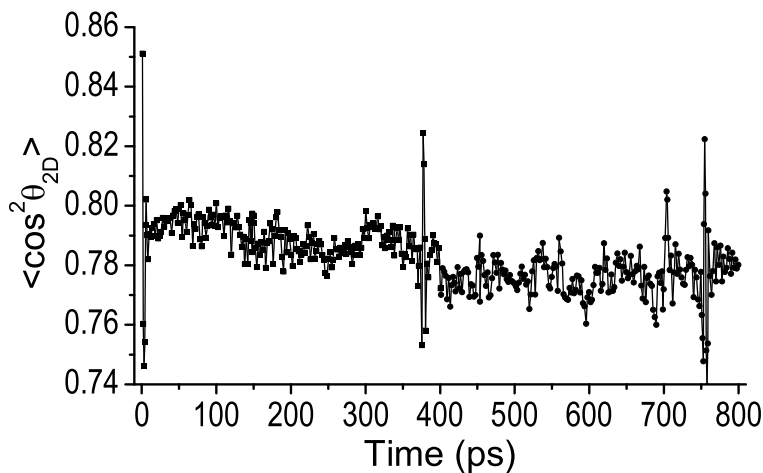


Figure 6.7:  $\langle \cos^2 \theta_{2D} \rangle$  determined from iodobenzene ion images. The images from 400–800 ps (circles) are recorded with a slightly weaker alignment pulse than the images from 0–400 ps (squares). A slight drift of the experimental conditions are the cause of the weak long term changes. When no alignment pulse is present  $\langle \cos^2 \theta_{2D} \rangle = 0.69$ . Lines between the points are included to guide the eye.

the revivals is determined by the rotational motion of the molecules. The principal axes of iodobenzene are shown in the inset in fig. 6.8. The  $a$ -axis is the molecular symmetry axis, the  $b$ -axis is the axis in the molecular plane perpendicular to the  $a$ -axis, and the  $c$ -axis is perpendicular to the molecular plane. The rotational constants are accurately known (see appendix A) and the asymmetry parameter is  $\kappa = -0.965$ . Iodobenzene is therefore a near-prolate molecule ( $\kappa = -1$  is the prolate symmetric top limit).

To simplify the connection with RCS methods, we classify the revivals

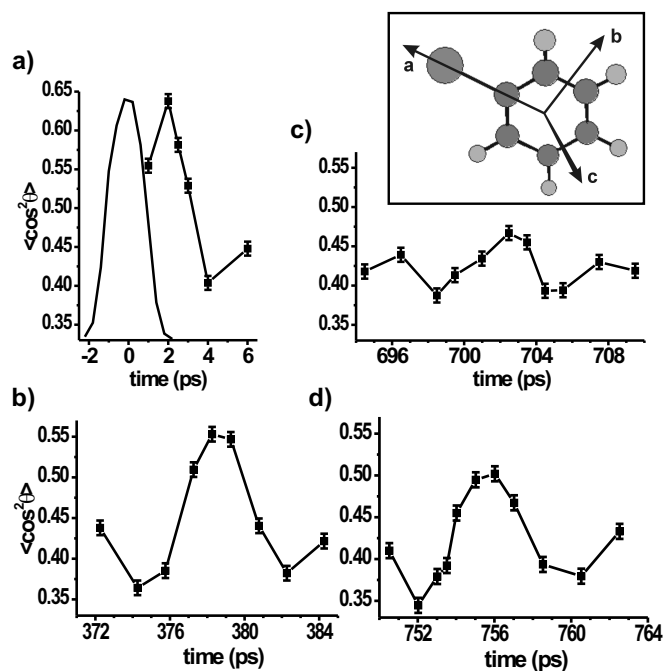


Figure 6.8:  $\langle \cos^2 \theta \rangle$  calculated from Abel inverted images at different delays. a) Right after the pulse b)–d) At the revival times. In a) is also shown the shape of the alignment pulse in arbitrary units on the ordinate axis. Lines between the points are included to guide the eye. Inset: The principal axes of iodobenzene.

with the RCS nomenclature introduced by Felker[73]. The time spacing between the early alignment peak (fig. 6.8 a) and the first revival (fig. 6.8 b) is 376.8 ps and the time spacing between the first and third revival (fig. 6.8 d) is 377.1 ps. Comparing with  $1/(4C) = 377.29$  ps we identify the first and third revivals as the first and second C-type revivals. The separation between the early alignment peak and the second revival (fig. 6.8 c) is 700.5 ps.

This is close to  $1/(B + C) = 707.7$  ps and we identify this transient as the first full J-type revival. The appearance of the J-type revival is due to the fact that iodobenzene is a near-prolate. The rotational energies can therefore with a good approximation be described by eq. 6.2,

$$E_{rot}(J, K_{-1}, M) = \bar{B}J(J + 1) + (A - \bar{B})K_{-1}^2, \quad \bar{B} = \frac{B + C}{2}, \quad (6.2)$$

where  $J$ ,  $K_{-1}$ , and  $M$  are the symmetric top quantum numbers. As for symmetric tops states in the wave packet with the same  $K_{-1}$  differ in energy by multiples of  $(B + C)$  causing full revivals spaced by  $1/(B + C)$ . Equation 6.2 is only an approximation and especially for large  $J$  it underestimates the energies. As stated before the wave packets of our experiments are very broad (the average value of  $J$ ,  $\langle J \rangle$ , is above 45 [2]), the J-type revival is therefore expected to appear slightly earlier than  $1/(B + C)$ , which is indeed the case. Retaining the symmetric top analogy a half J-revival is expected close to  $1/(2(B + C))$ . We could not resolve this transient in the above experiment but later experiments performed under different experimental conditions (shorter pulse duration) reveal a weak transient close to 356 ps.

The appearance of the C-type revivals is due to the polarizability tensor being significantly asymmetric. The mechanism can be explained with a classical argument. The presence of the linear alignment field causes the molecule to experience a force that rotates the major axis of polarizability, the  $a$ -axis, closer to the field vector, i.e. the molecule experiences a torque perpendicular to the  $a$ -axis. This is the cause of the alignment observed immediately after alignment pulse. Since the polarizability tensor is asymmetric the molecule also experiences a force that rotates the second axis of polarizability, the  $b$ -axis, towards the plane spanned by the  $a$ -axis and the alignment field vector, i.e. the molecule experiences a (smaller) torque

perpendicular to the  $b$ -axis. The only way to apply a torque that is perpendicular to both the  $a$ - and  $b$ -axes is to rotate around the  $c$ -axis. When the alignment field is gone there are no forces to move the axis of rotation and it will continue to be close to the  $c$ -axis. Since the molecules thus prefer to rotate around the  $c$ -axis, strong C-type revivals are observed.

Next I will focus on the intensity of the transients. As seen in fig. 6.8 a) the strongest alignment is reached immediately after the pulse. The observed revivals are only partial revivals and the initial alignment is therefore not completely reestablished. The C-type revivals are much stronger than the J-type revival. This observation is contrary to what is usually observed in RCS-spectra of near-prolate molecules: strong J-type revivals and weak C-type revivals[18]. It is an effect of the high laser intensity. High intensity causes a broad wave packet with high  $J$  values making the symmetric top approximation (eq. 6.2) less valid. Furthermore, the displacement of the axis of rotation that gives rise to the C-type revivals becomes more pronounced.

Figure 6.9 shows a quantum mechanical calculation of the alignment dynamics of iodobenzene subject to an alignment pulse with different intensities. The calculation was done at a much lower temperature than the experiment and without averaging the intensity over the focal volume of the probe pulse as it was done in the calculations presented in previous chapter. The calculated spectra in fig. 6.9 therefore have a much more oscillatory structure at the transients compared to the experiment. The calculations show how the intensity affects the amplitudes of the J- and C-type revivals. At the lowest intensity (fig. 6.9 a) the J-type revival is strongest whereas the C-type revival is dominant at the higher intensities (fig. 6.9 b–d). The calculation thus confirms that C-type revivals dominate at high intensities.

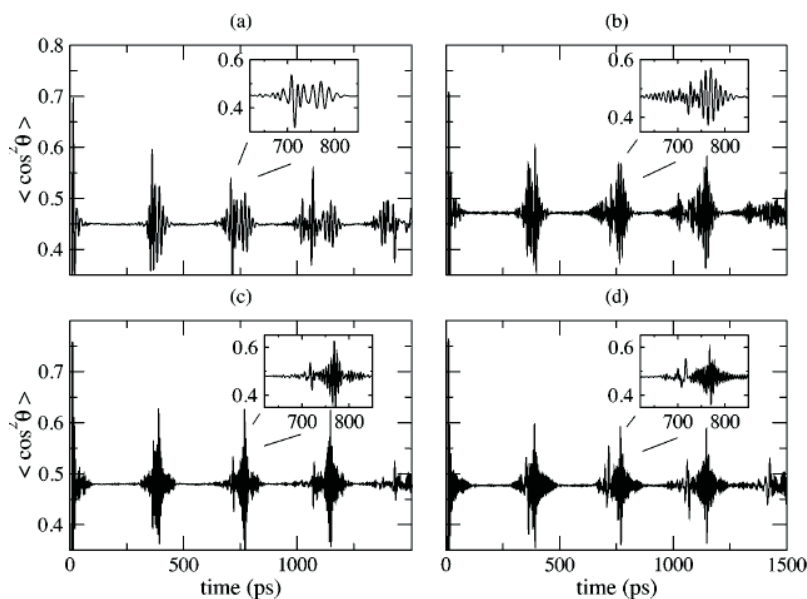


Figure 6.9: Quantum mechanical calculation of  $\langle \cos^2 \theta \rangle$  of iodobenzene initially at 0.4 K subject to a 2.6 ps alignment pulse with peak intensities: a)  $6.0 \times 10^{11}$  W/cm<sup>2</sup>, b)  $1.0 \times 10^{12}$  W/cm<sup>2</sup>, c)  $2.0 \times 10^{12}$  W/cm<sup>2</sup>, d)  $3.0 \times 10^{12}$  W/cm<sup>2</sup>.

### 6.3.2 Molecular asymmetry

As stated the iodobenzene molecule is a near-prolate. To further investigate the revival spectra of asymmetric top molecules we performed the same experiment on the iodopentafluorobenzene molecule ( $C_6F_5I$ ), which is much more asymmetric than iodobenzene. There are no values for the rotational constants of this molecule in the literature but assuming some standard bond lengths the rotational constants can be estimated (see appendix A). The asymmetry parameter is  $\kappa = -0.742$ , far from the prolate limit. The polarizability of this molecule is approximately as asymmetric

as the polarizability of iodobenzene, C-type revivals are therefore expected with intervals of  $1/(4C) \approx 921.8$  ps. Ion images were recorded close to the expected revival times and  $\langle \cos^2 \theta_{2D} \rangle$  extracted. At the local maxima and minima high statistic ion images were recorded, from which  $\langle \cos^2 \theta \rangle$  was extracted. The results are shown in fig. 6.10.

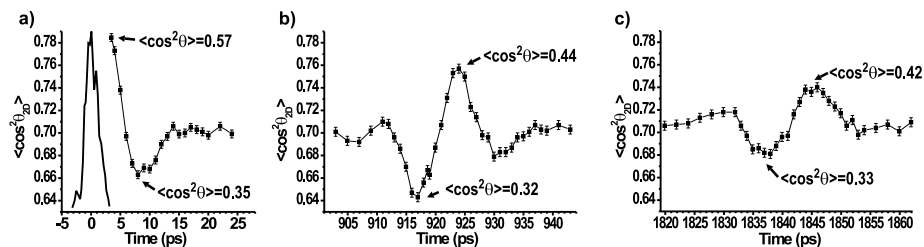


Figure 6.10:  $\langle \cos^2 \theta_{2D} \rangle$  calculated from ion images of iodopentafluorobenzene at different delays (without alignment pulse  $\langle \cos^2 \theta_{2D} \rangle = 0.65$ ). a) Right after the pulse b)-c) At the C-type revival times. In a) is also shown the shape of the alignment pulse ( $\tau_{FWHM} = 2.5$  ps,  $I_0 = 5 \times 10^{12}$  W/cm $^2$ ) in arbitrary units on the ordinate axis. At local minima and maxima  $\langle \cos^2 \theta \rangle$  values have been determined from high statistic images.

From fig. 6.10 it is seen that this molecule also exhibit strong C-type revivals. The delay between the two C-type revivals is  $921.1 \pm 0.5$  ps from which we obtain a rotational constant  $C = 271.4 \pm 0.2$  MHz, in perfect agreement with the estimated value ( $C = 271.2$  MHz). A possible J-type revival should appear close to  $1/(B + C) = 1563$  ps. However, since iodopentafluorobenzene is far from near-prolate a J-type revival is not expected for this molecule. We examined the interval 1547–1579 ps without finding any significant transient, consistent with expectation.

The quantum mechanical calculation shown in fig. 6.11 illustrate how the revival spectrum changes with increasing molecular asymmetry. The

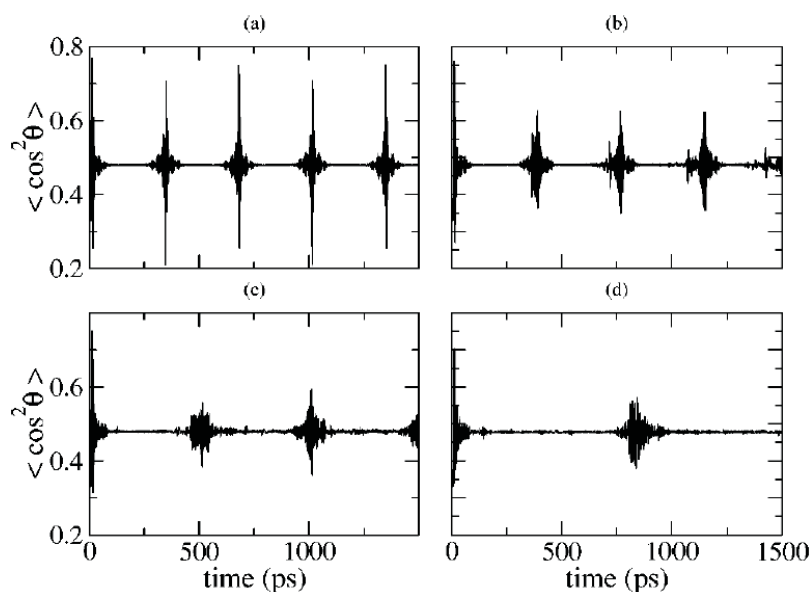


Figure 6.11: Quantum mechanical calculation of  $\langle \cos^2 \theta \rangle$  of an iodobenzene-like molecule initially at 0.4 K subject to a 2.6 ps alignment pulse ( $I_0 = 2.0 \times 10^{12}$  W/cm<sup>2</sup>) for different values of the  $C$  rotational constant: a) symmetric top limit,  $C = B$  ( $\kappa = -1$ ), b) iodobenzene value ( $\kappa = -0.965$ ), c)  $C = 500$  MHz ( $\kappa = -0.90$ ), d)  $C = 300$  MHz ( $\kappa = -0.83$ ). The  $A$  and  $B$  rotational constants were kept constant at the iodobenzene values.

calculation was done on an iodobenzene-like molecule with different values for the  $C$  rotational constants. In the prolate symmetric top limit (fig. 6.11 a) the spectrum is like the methyl iodide spectrum shown in fig. 6.2 with full recurrences of the alignment at intervals of  $1/(2B)$ . When the asymmetry increases (fig. 6.11 b) the revivals separate into J- and C-type revivals. With increasing asymmetry (fig. 6.11 c-d) the amplitude of the J-type becomes rapidly weaker compared to the C-type revivals. The

C-type revivals drop in amplitude and become broader.

The calculation confirms and generalizes our experimental results. The alignment on the revivals is strongest in the symmetric top limit but also very asymmetric molecules like iodopentafluorobenzene have significant rotational revivals.

## 6.4 Asymmetric top molecules of general type

The principal axes of polarizability and inertia of the asymmetric top molecules of the previous section coincided due to symmetry. However, for most asymmetric top molecules that is not the case. To investigate the revival spectrum of asymmetric top molecules belonging to this more general class we chose to perform alignment experiments on ethyl iodide and propyl iodide (fig. 6.12).

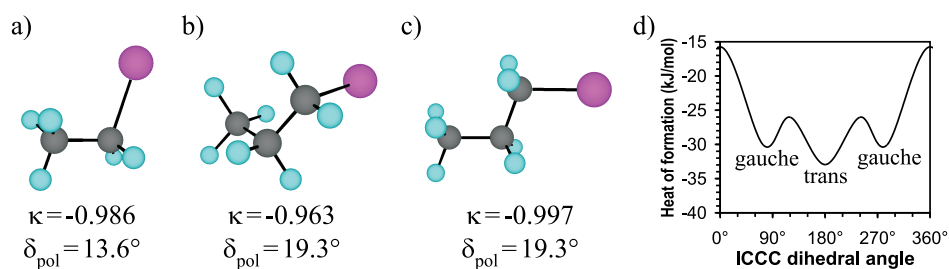


Figure 6.12: a–c) Structure, asymmetry of the inertia tensor,  $\kappa$ , and angle between the major axis of polarizability and the C–I bond axis,  $\delta_{pol}$  for a) ethyl iodide, b) gauche propyl iodide, c) trans propyl iodide. d) MOPAC molecular mechanics energy optimization of the conformers and transition states of propyl iodide (the curve is an interpolation of these points).

At room temperature the propyl iodide molecule exists in two different

conformers. The trans conformer (fig. 6.12 c) where the iodine and carbon atoms are located in a plane is thermodynamically the most stable. The gauche conformer is obtained from the trans by rotating the end-methyl group  $126.3^\circ$  around the C1–C2 axis<sup>[76]</sup><sup>3</sup>. Figure 6.12 d) shows a MOPAC molecular mechanics energy optimization of the conformers and transition states. The method of calculation is very simple, so the calculated values are only crude estimates. The energy barrier between the conformers is low ( $\sim 4$  kJ/mole) and the conformers can therefore rapidly interconvert at room temperature (where  $kT = 2.5$  kJ/mole). A Boltzmann distribution at room temperature has  $\sim 40\%$  of the molecules in the gauche conformer<sup>4</sup>.

### 6.4.1 Angle of detection

For these molecules the detection axis, the C–I bond axis, is not coinciding with the major axis of polarizability but located at an angle,  $\delta_{pol}$  (fig. 6.13 a). The detection axis is thus different from the molecular axis that is aligned.

To see how this would affect the experiment a calculation was made, in which experimentally obtained distributions or orientation of aligned methyl iodide molecules,  $f_{mol}(\theta)$ , were used to calculate the distribution of a detection axis,  $f_{mol}(\theta^{CI})$ , for a given  $\delta_{pol}$ .  $\langle \cos^2 \theta^{CI} \rangle$  was then calculated from  $f_{mol}(\theta^{CI})$  (fig. 6.13 b). In the calculation it was assumed that for a given angle of the major axis of polarizability,  $\theta$ , the detection axis could be located with equal probability anywhere on the circle described by  $\delta_{pol}$ .

---

<sup>3</sup>The two conformers differ not only in the ICCC dihedral angle, the other internal coordinates are slightly different

<sup>4</sup>The MOPAC molecular mechanics calculation estimate the energy difference between the conformers to 2.84 kJ/mole. Accounting for the two-fold degeneracy of the gauche conformer this corresponds to 39% of the total population being in the gauche conformer for molecules in thermal equilibrium at 298 K.

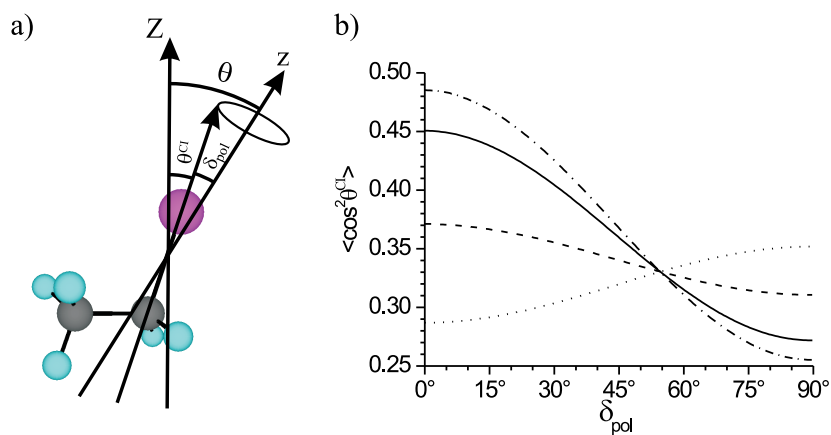


Figure 6.13: a) Ethyl iodide axes and angles: alignment pulse polarization (Z-axis), major axis of polarizability (z-axis), and C–I bond axis. Angle between C–I bond axis and Z-axis ( $\theta^{CI}$ ), Angle between C–I bond axis and z-axis ( $\delta_{pol}$ ), and angle between Z- and z-axes ( $\theta$ ). b) Calculation of  $\langle \cos^2 \theta^{CI} \rangle$  as a function of  $\delta_{pol}$  for distributions of aligned molecules,  $f_{mol}(\theta)$ , extracted from methyl iodide ion images recorded at different delays corresponding to different degrees of alignment (when  $\delta_{pol} = 0$   $\langle \cos^2 \theta^{CI} \rangle = \langle \cos^2 \theta \rangle$ ).

This assumption requires the polarizability perpendicular to the major axis to be equal in all directions (symmetric top polarizability). For all three molecules studied,  $\alpha_{xx} \approx \alpha_{yy}$  (appendix A), i.e. almost symmetric top polarizability.

From the calculation it is seen that alignment can be detected at all angles,  $\delta_{pol}$ , away from the “magic angle”,  $\arccos(\sqrt{\frac{1}{3}}) = 54.7^\circ$ . The studied molecules have small  $\delta_{pol} < 20^\circ$ , for which the detection angle only result in a slightly lower degree of observed alignment.

### 6.4.2 Ion images

Figure 6.14 shows ion images of I photofragments from ethyl iodide and propyl iodide seeded in helium. Focusing first on the images without alignment pulse (fig. 6.14 a and c), these images are similar to the methyl iodide image (fig. 6.1 a) except that no sharp rings are observed. The kinetic energy distributions of the I fragment from these molecules are broad because the ethyl and propyl fragments can be left in a very broad range of rotational and vibrational states. Figures 6.14 b) and d) show images recorded 1 ps after the peak of the alignment pulse ( $\tau_{FWHM} = 1.0$  ps,  $I_0 = 9 \times 10^{12}$  W/cm<sup>2</sup>). As in our previous alignment experiments a confinement along the vertical axis is observed, which we interpret as molecular alignment. As for methyl iodide an extra ring of low kinetic energy fragments appears in the aligned images due to an ionization channel involving the alignment pulse (the alignment pulse is not completely off at  $t = 1$  ps).

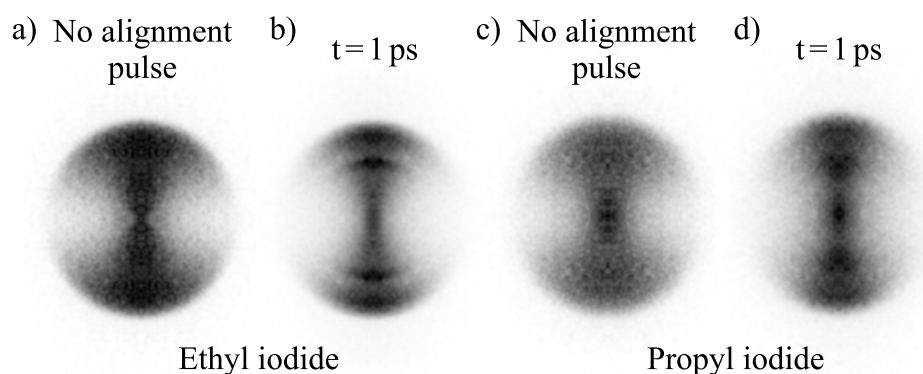


Figure 6.14: Ion images of I photofragments from ethyl iodide and propyl iodide. a+b) Ethyl iodide, c+d) propyl iodide. a+c) Without alignment pulse, b+d) 1 ps after the peak of the alignment pulse.

From the ion images  $\langle \cos^2 \theta^{CI} \rangle$  can be extracted,  $\theta^{CI}$  being the detected angle. We obtain  $\langle \cos^2 \theta^{CI} \rangle = 0.48$  for ethyl iodide and  $\langle \cos^2 \theta^{CI} \rangle = 0.40$  for propyl iodide. The ion images thus confirm that a significant degree of alignment can be obtained even though the molecular axes do not coincide.

### 6.4.3 Revival spectra

As for the other molecules the alignment is measured directly on the 2-D ion images as  $\langle \cos^2 \theta_{2D}^{CI} \rangle$ .

#### Ethyl iodide

Figure 6.15 shows the alignment dynamics of ethyl iodide immediately after the pulse and at rotational revivals. All the rotational revivals are weak. Local minima appear at the predicted half J-type revival times<sup>5</sup> (fig. 6.15 b and d) and local maxima appear at the predicted full J-type revival times (fig. 6.15 c and e). At the predicted C-type revival times a complicated pattern of weak oscillations is observed.

We believe the weakness of the revivals is at least partly due to the  $6^\circ$  angle between the major axes of polarizability and inertia. Since both inertia and polarizability of ethyl iodide are very near-prolate the J-type revivals are expected to be stronger than the C-type revivals as observed in fig. 6.15. Since the two different revival types are very close in time interference between them is expected. We believe this is the cause of the oscillating patterns at the expected C-revival times. Interference might also partly be the cause of the low amplitude of the revivals. Oscillations due to interference depend strongly on the intensity of the alignment field.

---

<sup>5</sup>We assume the first alignment peak occurs  $\sim 1$  ps after the peak of the alignment pulse.

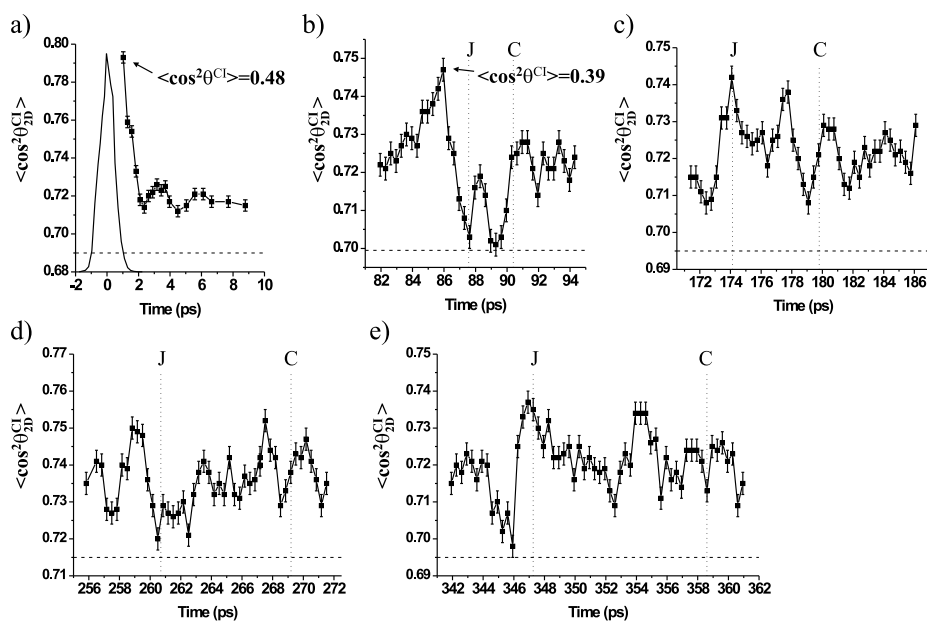


Figure 6.15: Alignment dynamics of ethyl iodide seeded in helium immediately after the alignment pulse and at rotational revivals measured as  $\langle \cos^2 \theta_{2D}^{CI} \rangle$ . The dashed horizontal lines indicate  $\langle \cos^2 \theta_{2D}^{CI} \rangle$  without the alignment pulse. The dotted vertical lines indicate expected half and full J-type revivals ( $t = n \frac{1}{2(B+C)} + 1$  ps) and expected C-type revivals ( $t = n \frac{1}{4C} + 1$  ps). a) Alignment dynamics immediately after the pulse, b) first half J-type revival, c) first full J-type revival, d) second half J-type revival, e) second full J-type revival.

Averaging over different intensities in the focus of the probe pulse will therefore reduce the amplitude of the oscillations. A way to reduce the range of intensities in the probed volume would be to use the Coulomb explosion probe pulse (sect. 7.1), which probes a smaller volume.

## Propyl iodide

Figure 6.16 shows the alignment dynamics of propyl iodide immediately after the pulse (fig. 6.16 a) and in the interval 140–206 ps (fig. 6.16 b).

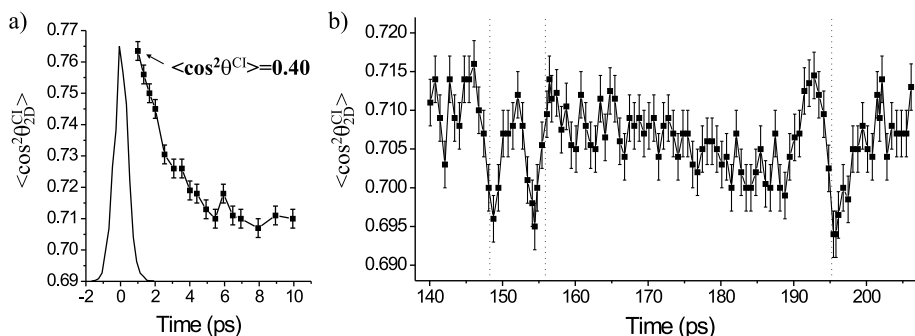


Figure 6.16: Alignment dynamics of propyl iodide seeded in helium measured as  $\langle \cos^2 \theta_{2D}^{CI} \rangle$ . a) Immediately after the alignment pulse, b) The time interval 140–206 ps. The dotted vertical lines are the expected times for: the first half J-type revival ( $t = \frac{1}{2(B+C)} + 1$  ps) of gauche propyl iodide (148 ps), first C-type revival ( $t = \frac{1}{4C} + 1$  ps) of gauche propyl iodide (156 ps), and first half J-type revival ( $t = \frac{1}{2(B+C)} + 1$  ps) of trans propyl iodide (195 ps).

The alignment dynamic immediately after the pulse is slower and the degree of alignment lower for this molecule compared to ethyl iodide. We believe the lower degree of alignment is partly due to a larger angle between C–I bond axis and major axis of polarizability,  $\delta_{pol}$ , compared to ethyl iodide. Furthermore, the two propyl iodide conformers have different anisotropy of polarizability. As a consequence the trans conformer is expected to align slightly earlier than the gauche conformer. The presence of both conformers should thus result in a broader alignment peak as

observed.

The alignment spectrum in the interval 140–206 ps reveals three weak transients. The first transient has a local minimum at 148.5 ps, very close to the expected time for the first half J-type revival of the gauche conformer,  $\frac{1}{2(B+C)} + 1$  ps. The second transient has a local minimum at 154.5 ps and a very weak local maximum at 157 ps, close to the expected time for the first C-type revival of the gauche conformer,  $\frac{1}{4C} + 1$  ps. The last transient has a local minimum at 195.5 ps, very close to the expected time for the first half J-type revival of the trans conformer. The trans conformer is very close to a symmetric top,  $\kappa = -0.997$ , and any possible C-type revival coincide with the J-type revival.

The revival spectrum proves that both conformers are present in the molecular beam. The revivals are weak for the same reasons the ethyl iodide revivals were weak. Furthermore, since only one conformer contribute to the alignment the amplitude is lower.

The presence of both conformers indicate that the supersonic expansion does not convert the gauche conformer to the thermodynamically more stable trans conformer. The cooling of the internal motion of the molecules and the lack of collisions mean that the molecules in the molecular beam do not spontaneously convert from one conformer to the other.

Since the conformers are stable the rotational revivals may be used to select one over the other. At the rotational revivals one conformer is better aligned than the other. This could be exploited to favor the unwanted conformer in a photodissociation the same way alignment was used to control the photodissociation of iodobenzene (sect. 4.5). Another way of selecting one conformer is to use two pulses with wavelengths tuned to make a Raman transition between the conformers. This process also depend on the relative orientation of molecule and laser polarization and the rotational

revivals can therefore be used as a control tool as in the photodissociation scheme.

As seen in fig. 6.16 b) the revivals are very weak. We therefore suggest to enhance the alignment of one conformer by firing a second alignment pulse when the alignment of this conformer peaks. For example one could fire a second pulse at  $t = 193.5$  ps when the alignment of the trans conformer peaks. The result should be an enhancement of the alignment of the trans compared to the gauche conformer.

## 6.5 Conclusion

We have shown that rotational revivals of alignment occur for all types of molecules. In the case of linear and symmetric top molecules the alignment at the rotational revivals is as strong as the alignment immediately after the peak of the alignment pulse (in the rigid rotor limit). For these molecules the rotational revivals are thus a suitable source of field free aligned molecules. For asymmetric top molecules the revivals are not full recurrences and the alignment here is weaker than immediately after the pulse. Applications requiring strong alignment should therefore employ the alignment obtained immediately after the pulse.

Since the revival times are determined by the rotational constants the spectrum of rotational revivals can be used for time resolved rotational spectroscopy as it has been done with weak field induced alignment in RCS. As seen in sect. 6.3 the revival spectrum changes dramatically with increasing intensity of the alignment pulse. The C-type revivals, which are very weak in typical weak field RCS-spectra of near-prolate molecules, are very strong. It would therefore in many cases be advantageous to supplement a weak field RCS-spectrum with a strong field spectrum.

Our method of recording revival spectra is not the most suitable for spectroscopic purposes. Due to the 20 Hz repetition rate of the molecular beam and the need for  $\sim 2000$  laser shots to obtain a reliable  $\langle \cos^2 \theta_{2D} \rangle$  value  $\sim 2$  minutes of data recording time is needed at each delay. From the ion images detailed information about the molecular distribution can be obtained ( $f_{mol}(\theta)$ ). However, for rotational spectroscopy the relevant information is the timing and shape of the revivals. This information can be gained faster and with more accuracy using other techniques such as degenerate four-wave mixing[65] or time resolved birefringence measurements[72, 30].

Weak field spectra are well simulated with simple perturbative expressions[18] resulting in very precise determinations of the rotational constants. Strong field spectra can be simulated with *ab initio* methods[5, 6]. However at rotational temperatures and intensities typically employed in the experiments the computational time for such calculations is many orders of magnitude too long for practical purposes. In order to obtain rotational constants from strong field spectra with the same precision as weak field spectra an approximative method of simulating these spectra would be appreciated.

For mixed samples consisting of different molecules, conformers, or isotopes the rotational revivals present intriguing perspectives for selecting one species because the different species have rotational revivals at different times. With a proper method of simulation the revival spectrum could also be used analytically to find the composition of the sample.

## Chapter 7

# Combining adiabatic and non-adiabatic alignment

The results presented in the previous chapters have shown adiabatic alignment induced by a long pulse (chapter 4) and non-adiabatic alignment induced by a short pulse (chapters 5 and 6). In this chapter, the alignment obtainable in the two regimes is compared and it is shown that the alignment is significantly enhanced when the two laser fields are combined.

### 7.1 Coulomb explosion probe

To make a direct comparison and to be able to combine adiabatic and non-adiabatic laser fields a probe is needed, which can be used in both types of experiments. This probe pulse must be short enough ( $\leq 0.5$  ps) to provide adequate time-resolution in the non-adiabatic alignment experiment. For the adiabatic alignment experiments presented in chapter 4 it was necessary to stretch the dissociation pulse to 1.5 ps to avoid direct ionization from the

combined 266 nm and 1064 nm fields. Dissociation at 266 nm can therefore not be used as a probe of alignment in this combination experiment.

Instead we chose to use a very short ( $\sim 20$  fs), intense ( $I_0 \approx 2 \times 10^{14}$  W/cm<sup>2</sup>) 800 nm pulse to probe the alignment. This very intense pulse strips one or more electrons of the molecule. The electronic repulsion between positive charges then causes the molecule to fragment. This process is known as a Coulomb explosion. The I<sup>+</sup> ion is a common fragment when Coulomb exploding molecules containing a C–I bond. The velocity vector of the I<sup>+</sup> ion indicate the position of the C–I bond prior to the Coulomb explosion. It is thus possible to gain information about the distribution of molecular orientations by making ion images of I<sup>+</sup> ions as for the dissociation probe scheme.

The two different probe schemes we have employed each have their advantages and disadvantages. The Coulomb explosion probe is in principle applicable to all molecules, not just molecules with C–I bonds. Furthermore, since the intensity of the Coulomb probe is so much higher than that of the alignment pulse the probe process is usually not affected by the presence of an alignment field<sup>1</sup>.

The Coulomb explosion is highly non-linear, which means that the probability of the process scales with a high order of the intensity. This has several effects. The effective volume probed by this pulse is much smaller than that of the dissociation pulse, because only the molecules experiencing the highest intensities in the focal volume are affected. Another effect of

---

<sup>1</sup>If the alignment and Coulomb explosion fields have different wavelengths an accidental resonance might change the Coulomb ionization process. We have observed this phenomena on methyl iodide when trying to use an 800 nm Coulomb probe in the presence of a 1064 nm adiabatic alignment field. We could therefore not use the Coulomb explosion pulse to probe adiabatic alignment of methyl iodide. No such accidental resonances were observed for iodobenzene.

the high non-linearity is that this probe has a very strong preference for molecules at small  $\theta$  angles. As a result the intensity of the probe has to be reduced dramatically to avoid ‘saturation’ effects, i.e. the intensity is too high for the probability of ionization to be the product of the photon flux and an angle dependent cross section, as it was assumed for the dissociation probe (sect. 4.4.4). It is therefore not possible to divide by the selectivity of the probe to obtain the distribution of molecules prior to the probe pulse. The alignment was therefore measured directly on the 2-D ion images using  $\langle \cos^2 \theta_{2D} \rangle$  as a qualitative measure as in chapter 6. The standard deviation of the measured  $\langle \cos^2 \theta_{2D} \rangle$  values is  $\sim 0.006$ . The uncertainty is higher for the Coulomb probe compared to the dissociation probe because the high non-linearity makes it more vulnerable to intensity fluctuations.

Since Abel inversion was not relevant, the polarization of the Coulomb probe pulse was chosen to be circular. The difference between ion images recorded with and without alignment pulse is greatest when the probe polarization is circular. When the probe polarization is linear the ion image without the alignment is already very confined along the vertical axis.

## 7.2 Experiment

We chose to use the iodobenzene molecule for this experiment for two reasons. The first reason is that we have extensive data on our “favorite molecule”, iodobenzene, to compare our results to. The second reason is that the presence of the 1064 nm adiabatic field does not affect the Coulomb explosion of this molecule (except through alignment).

The experiments are similar to those presented in chapters 4 and 5 except that the dissociation and ionization pulses are replaced by the circularly polarized Coulomb explosion probe pulse. The polarizations of both

alignment pulses are linear and parallel.

### 7.3 Comparing adiabatic and non-adiabatic alignment

Since the obtained degree of alignment was quantified as  $\langle \cos^2 \theta \rangle$  in chapters 4 and 5 a comparison of adiabatic and non-adiabatic alignment can already be made from those results even though the dissociation probe pulse is different in the experiments. We found that the highest degree of alignment obtained with an adiabatic pulse ( $\langle \cos^2 \theta \rangle = 0.68$ ) was significantly higher than the highest degree of alignment obtained with one non-adiabatic pulse ( $\langle \cos^2 \theta \rangle \approx 0.62$ ). To confirm that this result was not due to other experimental differences such as rotational temperature, the experiments were redone with the Coulomb explosion probe.

#### 7.3.1 Ion images

Figure 7.1 a) shows a 2-D  $I^+$  ion image obtained with only the circular polarized Coulomb explosion probe. Two rings are observed in the image corresponding to two different ionizations channels yielding  $I^+$  with different kinetic energies. In both rings an angular confinement along the vertical axis is observed. This confinement is due to the selectivity of the probe, molecules with the C-I bond axis located close to the (vertical) polarization plane of the circular polarized probe pulse have a higher chance of ionization. When the molecules are aligned with either a non-adiabatic pulse (fig. 7.1 b) or an adiabatic pulse (fig. 7.1 c) the usual confinement along the vertical axis is observed.

The images shown in fig. 7.1 b) and c) correspond to the strongest

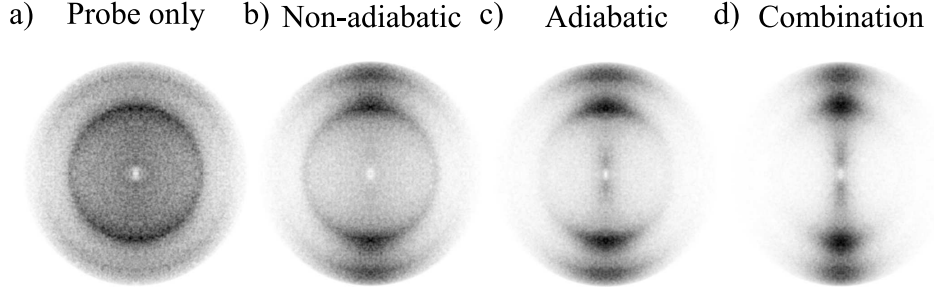


Figure 7.1: 2-D ion images of  $I^+$  ions originating from Coulomb explosion of iodobenzene. a) Circular polarized Coulomb explosion probe alone, b) Strongest alignment with a 2.1 ps non-adiabatic alignment pulse ( $I_0 = 5.8 \times 10^{12} \text{ W/cm}^2$ ), c) Strongest alignment with an adiabatic alignment pulse ( $I_0 = 7.8 \times 10^{11} \text{ W/cm}^2$ ), d) Strongest alignment with both adiabatic and non-adiabatic alignment pulses.

alignment obtained in either regime. From these images it is already evident that the strongest alignment (narrowest confinement) is obtained in the adiabatic regime. The ion image recorded with both alignment pulses present (fig. 7.1 d) reveal that the alignment can be significantly enhanced by including both pulses.

$\langle \cos^2 \theta_{2D} \rangle$  calculated on either of the two rings can be used as a qualitative measure of alignment. The results presented in this thesis are measurements on the outer ring but equivalent results are obtained if a measurement of the inner ring is used.

### 7.3.2 $\langle \cos^2 \theta_{2D} \rangle$ measurements

Figure 7.2 a) shows  $\langle \cos^2 \theta_{2D} \rangle$  calculated from ion images recorded at different intensities of the adiabatic alignment pulse. The figure is in qualitative agreement with fig. 4.7. The alignment improves with increasing intensity. At high intensities saturation is observed so that the alignment is only

weakly enhanced with increasing intensity.

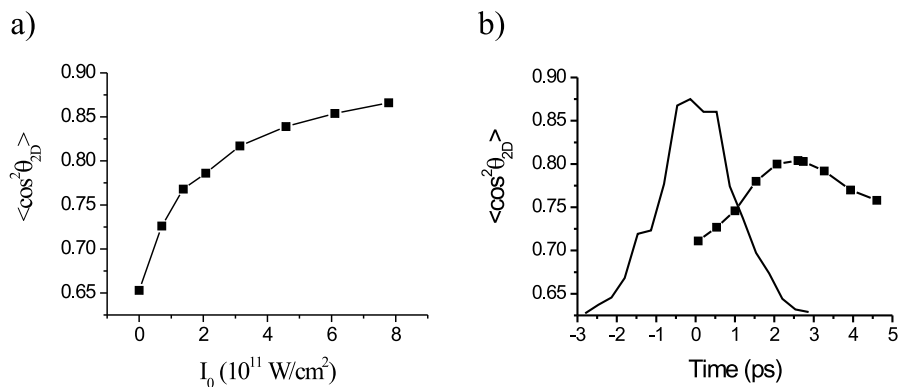


Figure 7.2:  $\langle \cos^2 \theta_{2D} \rangle$  calculated on the outer ring of  $\text{I}^+$  ion images. a) Adiabatic alignment at different intensities,  $I_0$ , of the alignment pulse. b) Non-adiabatic alignment at different delays with respect to the peak of the 2.1 ps alignment pulse ( $I_0 = 5.8 \times 10^{12} \text{ W/cm}^2$ ), also shown is the cross correlation trace of the alignment pulse (solid line). Lines between points included to guide the eye.

Figure 7.2 b) shows alignment measured as  $\langle \cos^2 \theta_{2D} \rangle$  following a 2.1 ps non-adiabatic alignment pulse. This pulse duration was chosen because the alignment then peaks under field free conditions (cf. sect. 5.1.4). The intensity of the alignment pulse was the maximum tolerable by the molecules. The figure is identical to fig. 5.7 c).

These  $\langle \cos^2 \theta_{2D} \rangle$  measurements confirm that a stronger alignment is obtained with an adiabatic alignment pulse compared to one non-adiabatic alignment pulse, as it was already evident in the ion images (fig. 7.1).

## 7.4 Combining adiabatic and non-adiabatic alignment

### 7.4.1 Short time dynamics

For this combined fields experiment the dynamics at short delays are most interesting because that is where an enhancement of the alignment is observed.

In sect. 5.2 it was shown that non-adiabatic alignment could be significantly enhanced by using a weak pulse to prealign the molecules. With this scheme the obtained degree of alignment approached that obtained with an adiabatic pulse. The basic idea of the combination experiment is essentially the same as the two-pulse non-adiabatic alignment experiment. Now it is just an adiabatic alignment pulse that is used to prealign the molecules and thus enhance the alignment induced by the short non-adiabatic pulse.

Figure 7.3 shows measured  $\langle \cos^2 \theta_{2D} \rangle$  values of molecules aligned with the non-adiabatic pulse alone or combined with an adiabatic pulse. In fig. 7.3 a) the intensities of both alignment pulses are relatively low. With the non-adiabatic pulse alone, the alignment maximum is  $\langle \cos^2 \theta_{2D} \rangle = 0.81$  occurs under field free conditions at  $t \approx 2.2$  ps. When the adiabatic alignment pulse is included the alignment is dramatically enhanced to  $\langle \cos^2 \theta_{2D} \rangle = 0.87$  and peaks earlier at  $t \approx 1.6$  ps. Note that the alignment is enhanced beyond the level obtained with the adiabatic pulse alone ( $\langle \cos^2 \theta_{2D} \rangle = 0.82$ ). After the peak the alignment in the combined fields experiment drops off and remain below the level obtained with the adiabatic pulse alone.

Going from fig. 7.3 a) to b) the intensity of the adiabatic alignment pulse is increased. This increase enhances the alignment of the combined fields to  $\langle \cos^2 \theta_{2D} \rangle = 0.89$  and causes a slightly earlier alignment peak

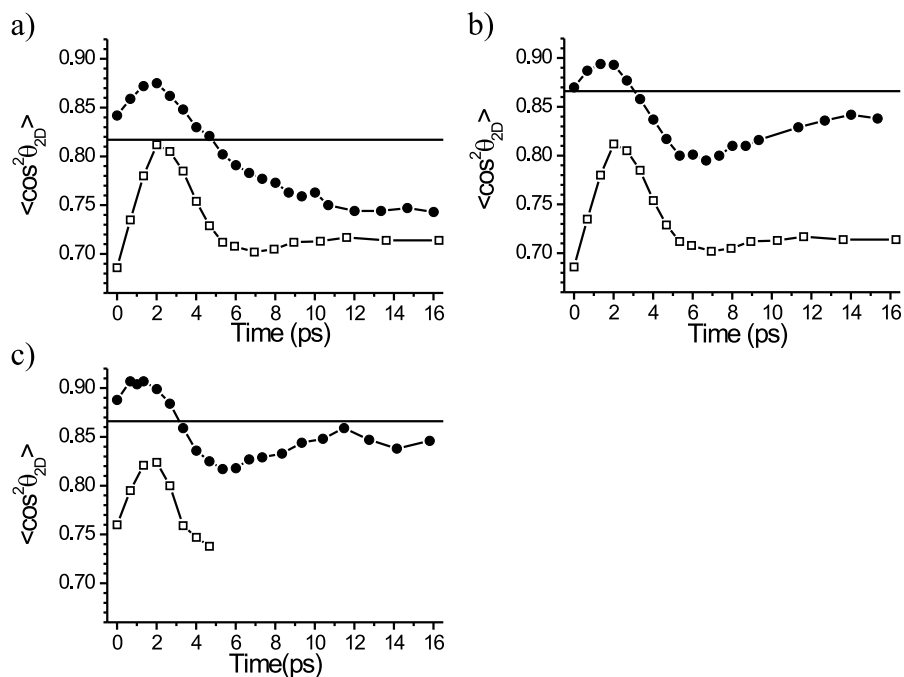


Figure 7.3:  $\langle \cos^2 \theta_{2D} \rangle$  calculated from ion images of iodobenzene subject to: a 2.1 ps non-adiabatic alignment pulse centered at  $t = 0$  (squares), an adiabatic alignment pulse (solid line), or both pulses (circles). Lines between points included to guide the eye. The peak intensities were:

- a)  $I_0(\text{non-adiabatic}) = 3.5 \times 10^{12} \text{ W/cm}^2$ ,  $I_0(\text{adiabatic}) = 3.1 \times 10^{11} \text{ W/cm}^2$ ,
- b)  $I_0(\text{non-adiabatic}) = 3.5 \times 10^{12} \text{ W/cm}^2$ ,  $I_0(\text{adiabatic}) = 7.8 \times 10^{11} \text{ W/cm}^2$ ,
- c)  $I_0(\text{non-adiabatic}) = 5.8 \times 10^{12} \text{ W/cm}^2$ ,  $I_0(\text{adiabatic}) = 7.8 \times 10^{11} \text{ W/cm}^2$ .

( $t \approx 1.4$  ps). Going from fig. 7.3 b) to c) the intensity of the non-adiabatic alignment pulse is increased. This increase enhance the combined fields alignment even further to  $\langle \cos^2 \theta_{2D} \rangle = 0.91$  and causes an even earlier peak of the alignment at  $t \approx 1.0$  ps. Note that in all cases the combined fields

alignment after the peak drops off and remains below the level obtained with the adiabatic pulse alone.

We can thus conclude that by combining the fields the maximum alignment is enhanced beyond the level obtained with either pulse alone. An increase of the intensity of either alignment pulse causes an enhancement of the combined fields alignment and displaces the alignment peak to an earlier time. After the peak the combined fields alignment drops and stabilize below the level obtained with the adiabatic pulse alone. The alignment at long delays is governed by the presence of the adiabatic alignment field (which can be viewed as constant in time on this picosecond timescale). At these long delays the effect of the non-adiabatic pulse is just an increase of the average value of  $J$ ,  $\langle J \rangle$ , similar to an increase of rotational temperature.

The quantum mechanical calculation on tert-butyl iodide shown in fig. 7.4 confirms our experimental results. The calculation is done for another molecule and at a lower rotational temperature than the experiment, nonetheless the same features are observed. The combined fields alignment is stronger than that obtained with either field. Furthermore, the effect of an increase of the intensity of either alignment pulse is an enhancement of the maximum alignment and an earlier alignment peak, as observed in the experiment. At longer delays the combined fields alignment remain below the level of the alignment obtained with the adiabatic pulse alone, as was also observed in the experiment.

The enhanced alignment observed in this experiment is by no means obtained under field free conditions. Not only is the weak adiabatic field present but the alignment peaks so fast that a substantial part of the non-adiabatic field is also present. As commented earlier pulse shaping[67, 68] can be employed to change the temporal profile of the non-adiabatic alignment pulse so that the decline of the pulse is fast enough that the non-

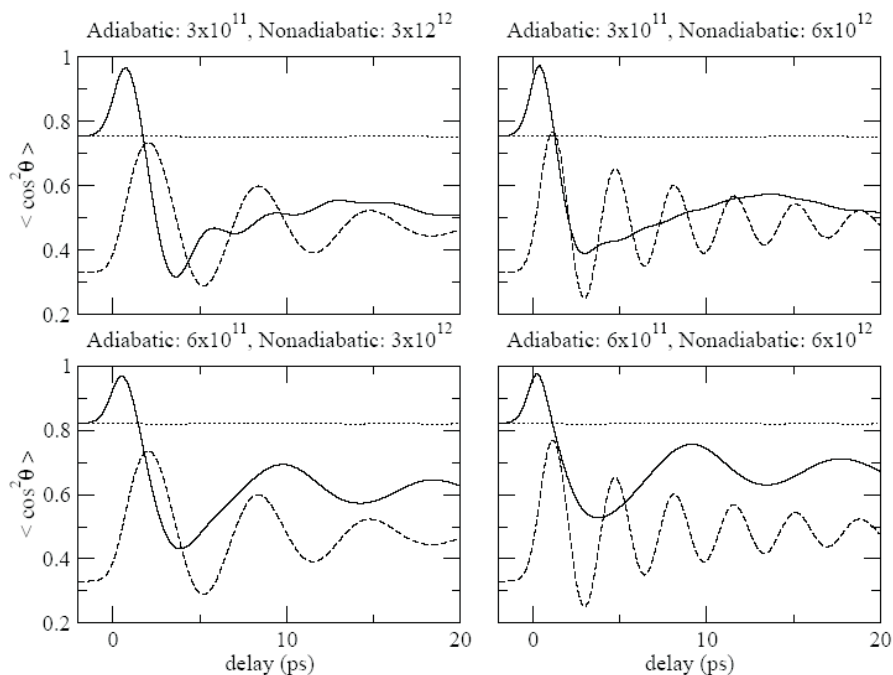


Figure 7.4: Alignment dynamics ( $\langle \cos^2 \theta \rangle$ ) of tert-butyl iodide initially at  $T = 1$  K subject to a 1.7 ps non-adiabatic pulse (dashed curve), an adiabatic pulse (dotted line), or both (solid curve). The intensities of the alignment pulses are quoted above the panels. Calculation by E. Hamilton and T. Seideman appearing in [7].

adiabatic alignment field is off when the alignment peaks. Underwood et al. [36] demonstrated that also a long (125 ps) pulse could be truncated very fast (within  $\sim 100$  fs). Such a truncated adiabatic alignment pulse together with a properly shaped non-adiabatic alignment pulse would thus be ideal for obtaining very well aligned molecules under field free conditions. Note that this scheme produces a stronger field free alignment than that achieved with two-pulse non-adiabatic alignment.

### 7.4.2 Rotational revivals

We have so far not done more than preliminary investigations regarding rotational revivals in the combined fields experiment. The C-type rotational revivals observed in non-adiabatic alignment experiments are still observable when a weak ( $\sim 1 \times 10^{11}$  W/cm<sup>2</sup>) adiabatic field is included. However, the revivals are weaker than without the adiabatic field. When the intensity of the adiabatic field is increased to  $5 \times 10^{11}$  W/cm<sup>2</sup> the rotational revivals are no longer experimentally observable.

If the eigenstates in the presence of the adiabatic field (pendular states) have a regular energy spacing new types of revivals may appear in the presence of the adiabatic field. That is the case for linear molecules in a strong adiabatic field[29]. Pendular revivals are thus expected in a combined fields experiment on a linear molecule provided a sufficiently intense adiabatic pulse is used. Since asymmetric top molecules do not gain such a regular spacing of the energy levels, no pendular revivals are expected for the asymmetric top iodobenzene molecule.

We plan to investigate the rotational revivals of a planar asymmetric top molecule in another type of combined fields experiment involving adiabatic and non-adiabatic pulses with orthogonal (linear) polarizations. The idea is to use a strong adiabatic field to ‘lock’ the major axis of polarizability and then align the molecular plane with the non-adiabatic pulse. After the short pulse we expect to observe rotational revivals corresponding to the molecule spinning about the major axis.

## 7.5 Conclusion

We have shown that a higher degree of alignment can be obtained with a long adiabatic pulse compared to one short non-adiabatic pulse. By com-

---

binning an adiabatic pulse with a non-adiabatic pulse the induced alignment can be enhanced beyond the level obtained with either pulse alone. When the intensity of either alignment pulse is increased the combined field alignment is improved and the alignment peak occur at an earlier time compared to the peak of the non-adiabatic pulse. After the initial peak the combined fields alignment drops and stabilize at a degree of alignment below that obtained with the adiabatic pulse alone. The strongly enhanced alignment obtained by this combination of laser pulses can be made field free with an appropriate shaping (sharp cut-off) of the temporal profiles of both alignment pulses.

## Chapter 8

# Outlook

The results presented in this thesis represent our contribution to the development of the field of laser induced alignment of molecules in the past four years. In the future we wish to continue the development of alignment techniques, to combine laser induced alignment with other methods of molecular control, and explore some of the many possible applications of alignment.

This chapter deals with some of the ideas we have for future experiments. Many of our future experiments are facilitated by a major upgrade of the experimental apparatus that is ongoing at the moment. The first section of this chapter deals with the improvements of this upgrade and the new possibilities they enable. In the next section possible future experiments are discussed.

## 8.1 Experimental improvements

A new vacuum chamber is currently being installed. This new vacuum chamber contains many upgrades compared to the old. Furthermore, the optical setup is expected to be upgraded with a programmable pulse shaper in the near future (provided sufficient funds). These upgrades will improve the quality of our experimental data and facilitate experiments, which so far have not been possible for us to perform.

### 8.1.1 New pulsed valve

The new vacuum chamber will be equipped with a pulsed supersonic valve of the Even-Lavie type[77, 78]. This new valve has several advantages compared to the Jordan valve we have used so far. It can be run with a repetition rate of 40 Hz, twice as fast as the Jordan valve. The Even-Lavie valve has a conical nozzle design, which gives a more efficient cooling and thus a lower rotational temperature of the sample. Furthermore, it can withstand a very high backing pressure (100 bar). An increase of the backing pressure results in a more efficient cooling.

The nozzle design also provides a higher sample density because the molecules will be ejected in a very narrow cone. A detail in the design of the new vacuum chamber will also increase the sample density: In our old vacuum chamber the molecules travel  $\sim 70$  cm from the nozzle to the laser focus, in the new chamber this distance is reduced to  $\sim 40$  cm resulting in a higher sample density.

### 8.1.2 Velocity mapping using slice imaging

All the 2-D ion images presented in this thesis are made with the velocity imaging setup of Eppink and Parker[46]. In the new vacuum chamber this

setup will be replaced by the slice imaging setup of Gebhardt *et al.*[79] (fig. 8.1).

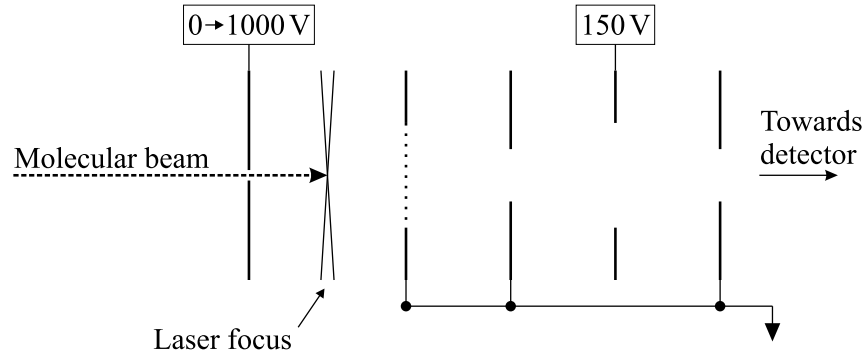


Figure 8.1: Schematic diagram of the slice imaging setup of Gebhardt *et al.*[79].

In this setup, the molecular beam is crossed with the laser beams midway between a repeller plate and a fine grid. The voltage of the repeller plate can be gated very fast from 0 to 1000 V. When the repeller plate is charged the ions experience a uniform electric field (between the repeller plate and grid) that pushes them towards the detector. On the way to the detector the ions pass through three plates with circular apertures. These three plates act as a lens (an Einzel lens) and make a velocity mapping of the ions on the detector like the three plates of the Eppink and Parker setup.

The idea of slice imaging is to use the time of flight as a measure of the velocity perpendicular to the detector. In order to increase the difference in time of flight between ions moving towards the detector and ions moving away from the detector the ions are allowed to propagate in a field free environment for a time until the repeller is quickly gated to 1 kV. With this broader range of ion flight times it is possible to time-gate the detector

so that only ions with a specific time of flight, corresponding to a specific velocity perpendicular to the detector, are detected. The ion image thus correspond to a slice through the 3-D ion velocity distribution.

If the ion velocity distribution has cylindrical symmetry (as in our linear alignment experiments) the 3-D ion velocity distribution can be obtained directly as the central slice (zero velocity perpendicular to the detector). The Abel inversion and the problem of the inherent center-line noise can thus be avoided. If the ion velocity distribution does *not* have cylindrical symmetry (as in 3-D alignment experiments) the 3-D ion velocity distribution is not obtainable with the Eppink and Parker setup. With slice imaging the 3-D ion velocity distribution can be obtained by recording slices corresponding to different velocities perpendicular to the detector.

### 8.1.3 Crossed laser beams

So far we have used colinear laser beams in our experiments. The polarizations of the involved beams are therefore restricted to the plane perpendicular to beam propagation axis. The new vacuum chamber has two orthogonal entrance windows and it is therefore possible to cross two laser beams in a  $90^\circ$  angle. With such crossed laser beam it will be possible to perform new experiments. An example is the control experiment discussed in sect. 4.5.2, in which the molecular plane of the iodobenzene molecule is aligned with a circular polarized alignment pulse and dissociated by a pulse with a polarization perpendicular to the molecular plane.

### 8.1.4 Programmable pulse shaper

With the current grating stretcher mounted in the non-adiabatic alignment pulse beamline, the pulses are stretched to a longer duration but retain

an approximately gaussian temporal profile. With the purchase of an extra grating and a liquid crystal spatial light modulator (SLM) the grating stretcher can be rebuilt as a programmable pulse shaper[68]. With a pulse shaper it is possible to shape the alignment pulses to have a sharp cut-off, so that the resulting molecular alignment is always reached under field free conditions. Furthermore, the results regarding alignment pulse duration (sect. 5.1.4 and 6.2.3) and the enhancement obtained by splitting the alignment pulse in two subpulses (sect. 5.2) can be generalized to experiments regarding the optimal pulse shape for obtaining the strongest alignment.

In principle the optimal pulse shape may be found with an evolutionary learning algorithm using a feed back from the alignment experiment[80]. However, this solution requires a very fast way of measuring alignment, especially because the exact timing of the alignment peak depends on the shape of the alignment pulse.

## 8.2 New experiments

There are many interesting aspects and applications of alignment we wish to investigate in the future.

### 8.2.1 Improving alignment

Results presented in this thesis show how linear alignment can be enhanced by using two short pulses (sect. 5.2) or by combining short and long pulses (sect. 7.4). We have shown that a high degree of alignment is obtainable with these relatively simple pulse sequences. With more elaborate pulse sequences and general pulse shapes it may be possible to enhance the alignment even more. Our most immediate efforts are however concerned with 3-D alignment.

Direct experimental evidence of 3-D alignment has only been presented in the adiabatic limit[32]. The improved control of the photodissociation of iodobenzene obtained with a short elliptically polarized alignment pulse presented in this thesis (sect. 4.5.2) is indirect evidence of 3-D alignment in the non-adiabatic regime. In the near future we wish to demonstrate direct evidence of 3-D alignment obtained with two orthogonal linearly polarized alignment pulses. Either two short non-adiabatic pulses as suggested by Underwood *et al.*[33] or a long and a short pulse as the experiment described in sect.7.4.2. The calculations by Underwood *et al.* show that a higher degree of alignment is obtained with two orthogonal linearly polarized pulses compared to one elliptically polarized alignment pulse.

### 8.2.2 Combining alignment and orientation

Although alignment of molecular axes is sufficient for many applications, heads vs tails orientation is needed in some applications.

Different schemes have been suggested for obtaining net orientation with laser fields alone. Sakai and Larsen[40] have suggested to use two laser fields with frequencies  $\omega$  and  $2\omega$ . Averaging over an optical period of such a combined field will average out interaction with the permanent dipole moment but not the third order interaction with the hyperpolarizability. Unfortunately, this interaction is for most molecules very weak at laser intensities below the threshold for multi photon ionization. Theoretical studies by Machholm and Henriksen[81] showed that orientation could be induced with a half-cycle pulse. The effect is however weak at feasible intensities. Spanner *et al.*[82] showed that the orientational effect of the half cycle pulse was greatly enhanced when it was fired at a fractional revival of a rotational wave packet induced by a short non-adiabatic alignment pulse. Laser induced orientation has yet to be demonstrated experimentally.

Another option for obtaining molecular orientation is a static electric field, either a uniform field or a hexapole (sect. 1.2.1). As stated in sect. 1.3 the axial confinement (alignment) obtained with static fields is weak compared to laser induced alignment. The idea of combining the orientation obtained with a static field with the strong alignment obtained with a laser field was proposed by Friedrich and co-workers. They calculated how an adiabatic[83, 84] or non-adiabatic[85] laser field affects molecules oriented by a static field.

How much the laser field enhance the orientation induced by the static field strongly depends on which measure of orientation is used. The conventional measure of orientation is the average value of  $\cos \theta$ ,  $\langle \cos \theta \rangle$ . Friedrich and co-workers show that  $\langle \cos \theta \rangle$  obtained with a weak static field will be strongly enhanced by a laser alignment field. However, a large part of this enhancement is simply due to the much stronger angular confinement.  $\langle \cos \theta \rangle$  can be increased without changing the fraction of molecules that “point in the right direction”, are within  $90^\circ$  of the field axis,  $P_{field}$ . However, if the rotational temperature is very low  $P_{field}$  can also be significantly enhanced by a strong laser field. This was demonstrated by Sakai *et al.*[86], who used a strong adiabatic alignment pulse to enhance the very weak orientation induced by the weak static extraction field (of the Eppink and Parker velocity mapping setup (sect. 3.3.1)) to  $P_{field} \approx 60\%$ .

In the near future we wish to combine a strong uniform static field and a strong laser field to obtain molecules that are both strongly aligned (high  $\langle \cos^2 \theta \rangle$ ) and mainly “point in the right direction” (high  $P_{field}$ ). This can be achieved simply by placing highly charged electrodes above and below the point where the molecular beam is crossed with the laser beams. However, there are some experimental difficulties that have to be overcome. The electrodes must be time-gated, so that the static field is on until the molecules

are dissociated but turned off before any ions are created. Furthermore, the extraction field will be affected by the presence of the electrode plates even when they are not charged. The velocity mapping of the ions will therefore be distorted.

### 8.2.3 Applications of alignment

As the work in the field of laser induced alignment has grown so has the number of applications of alignment. The applications fall in two categories: Those that take advantage of alignment as a tool for controlling molecular orientation and those that use the rotational wave packet created by a short non-adiabatic alignment pulse for other purposes.

Among the applications of the latter category is the use of the revivals for time resolved rotational spectroscopy as discussed in chapter 6. The revivals can also be used to manipulate the phase and spectral content of ultrashort light pulses[87] because the index of refraction of the sample changes rapidly at the very narrow revivals. Use of the rotational wave packet as a quantum logic system has also been demonstrated[88].

Alignment can be used as a control tool for all processes depending on the specific orientation of molecules compared to lab-fixed coordinates, except for the applications where head vs tail orientation is needed. In this thesis the use of alignment as a control tool for photodissociation was demonstrated (sect. 4.5). Just as weak-field photoabsorption depends on the relative orientation of molecule and electric field so does strong-field ionization[89]. The molecular symmetry play an important role in strong-field ionization[90]. In the near future we plan to use alignment as a control tool to demonstrate the role of symmetry experimentally as it has been recently done for a diatomic molecule[91]. Another application we wish to explore in the near future is the use of alignment as a control tool for angle

resolved photoelectron spectroscopy. Photoelectron angular distributions provide information on molecular structure, rotational perturbations, and potentially on radiationless transitions[92]. Other applications of alignment include the use in electron diffraction experiments[93] and enhancement of high-order harmonic generation[94].

In the slightly more distant future we would also like to use alignment at rotational revivals to control and select molecular conformers as discussed in sect. 6.4.3. If the alignment field is combined with a static field we may potentially be able to separate enantiomers<sup>1</sup> of chiral molecules.

### 8.2.4 Alignment in the liquid phase

So far all our studies of laser induced alignment has taken place in the gas phase. From a chemical point of view the liquid phase is more interesting than the gas phase, since most chemical reactions in both nature and laboratories take place in the liquid phase. It is well known that a strong polarized non-resonant laser field will also align molecules in the liquid phase. An effect of the alignment is an induced birefringence in the liquid, known as the optical Kerr effect (sect. 1.2.1). The optical Kerr effect has been used to study molecular dynamics in liquids and solutions for many years.

The degree of anisotropy needed to induce birefringence is very small. The main hindrance for obtaining a high degree of alignment in the liquid phase is that a liquid cannot be cooled without phase change (freezing). As a result the “rotational temperature” is high and not really well defined due to the constant collisions between molecules. In the case of adiabatic alignment of a pure liquid, the molecules can be assumed to have a Boltz-

---

<sup>1</sup>Enantiomers are molecules that are mirror images of each other.

mann distribution (sect. 2.3.1). From fig. 2.7 it is seen that the alignment of CS<sub>2</sub> molecules is modest ( $\langle \cos^2 \theta \rangle < 0.38$ ) at feasible alignment pulse intensities ( $I_0 < 10^{12}$  W/cm<sup>2</sup>).

However, sometimes it takes only a small change in the distribution of orientations to make an big effect. An example of this was recently given by Garetz *et al.*[95]. They showed that alignment can induce nucleation in a supersaturated solution. Even though the the liquid was only affected by the pulsed laser for a very short time (600 pulses of 6 ns each) and with relatively low intensity ( $7 \times 10^{11}$  W/cm<sup>2</sup>) crystals appeared after 30 minutes in solutions which had been left for days without spontaneous nucleation. The structure of the appearing crystals could even be controlled by using either linear or circular polarization of the alignment pulse. Thus even small changes in the relative orientation of molecules can make big changes in chemical reactivity.

Since polarizability scales with the size of the molecule, a higher degree of alignment is expected for larger molecules in solution. As discussed in sect. 1.2.1 static fields are already being employed to control very large (DNA) molecules in solution. A potentially much stronger optical field is thus expected to induce strong alignment of large molecules in solution. The first very preliminary steps towards laser induced alignment in the liquid phase is currently being taken in our lab. We have great expectations to these experiments and expect a whole new range of applications of alignment to arise.

### 8.3 Final words

It has been fascinating to contribute to the development of the field of laser induced alignment for the past five years. In that time both the field itself

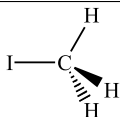
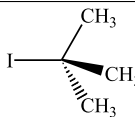
and the number of applications have grown rapidly. With the many new possibilities emerging, I am confident that the field will continue to grow in the future and alignment will be applied in many new and unforeseen contexts.



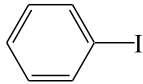
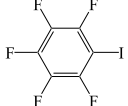
## Appendix A

# Molecular data

### A.1 Symmetric top molecules

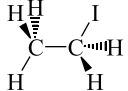
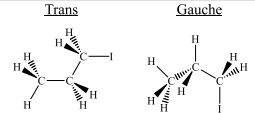
| Names  | Methyl iodide<br>Iodomethane   | Tert-butyl iodide<br>2-iodo-2-methylpropane  |
|--|--|--|
| Molecular formula  | CH <sub>3</sub> I  | C <sub>4</sub> H <sub>9</sub> I  |
| Molecular weight (g/mole)                                | 141.94   | 184.02   |
| Structure  |    |    |
| Bond lengths (Å)<br>and angles                           | r(CI)=2.139, r(CH)=1.11,<br>∠(ICH)=107.5°[96]  | r(CH)=1.093, r(CC)=1.54,<br>r(CI)=2.19, ∠(ICC)=107.4°,<br>∠(HCH)=arccos(-1/3)[97]  |
| Boiling temperature <sup>1</sup>                         | 42.5°C[98]   | 100°C[99]  |
| Seed temperature   | -40°C  | -30°C  |
| Vapor pressure <sup>2</sup> (mbar)                       | 22   | 2  |
| Gas phase absorption<br>cross section (Å <sup>2</sup> )  | 266 nm: 1.0×10 <sup>-2</sup><br>304 nm: 1×10 <sup>-4</sup> [100]   | 266 nm: 2.2×10 <sup>-2</sup><br>304 nm: 2×10 <sup>-3</sup> [101]   |
| Rotational constants (MHz)                               | A=150262, B=7501.30[102]   | A=2950.2, B=1563.7[97]   |
| Revival time <sup>3</sup> (ps)                           | t <sub>J</sub> =66.655   | t <sub>J</sub> =319.8  |
| Polarizability<br>volumes <sup>4</sup> (Å <sup>3</sup> ) | static: α <sub>  </sub> =9.0, α <sub>⊥</sub> =6.4<br>1064 nm: α <sub>  </sub> =9.1, α <sub>⊥</sub> =6.5<br>800 nm: α <sub>  </sub> =9.2, α <sub>⊥</sub> =6.6 | static: α <sub>  </sub> =15.0, α <sub>⊥</sub> =11.3<br>1064 nm: α <sub>  </sub> =15.1, α <sub>⊥</sub> =11.3<br>800 nm: α <sub>  </sub> =15.3, α <sub>⊥</sub> =11.4 |

A.2 Asymmetric top molecules of  $C_{2v}$ -type

| Name  | Iodobenzen   | Iodopentafluorbenzene   |
|---|--|---|
| Molecular formula   | $C_6H_5I$  | $C_6F_5I$   |
| Molecular weight (g/mole)                                   | 204.01   | 293.96  |
| Structure   |   |   |
| Bond lengths (Å) and angles                                 | $r(CI)=2.08$ , $r(CH)=1.101$ ,<br>$r(CC)=1.399$ , $\angle=120^\circ$ [96] <sup>5,6</sup>   | $r(CI)=2.08$ , $r(CF)=1.32$ ,<br>$r(CC)=1.399$ , $\angle=120^\circ$ [96] <sup>5</sup>   |
| Boiling temperature <sup>1</sup>                            | 188°C[98]  | 161°C[98]   |
| Seed temperature  | 23°C   | 23°C  |
| Vapor pressure <sup>2</sup> (mbar)                          | 1.1  | 0.7   |
| Gas phase absorption cross section (Å <sup>2</sup> )        | 266 nm: $2.3 \times 10^{-2}$<br>304 nm: $1 \times 10^{-3}$ [103]   |   |
| Rotational constants (MHz) asymmetry parameter <sup>7</sup> | $A=5671.89$ , $B=750.416$ ,<br>$C=662.627$ , $\kappa=-0.965$ [104]   | $A=1027.5$ , $B=368.8$ ,<br>$C=271.4$ , $\kappa=-0.742$   |
| Revival times <sup>8</sup> (ps)                             | $t_C=377.3$ , $t_J=707.7$  | $t_C=921.2$ , $t_J=1562.0$  |
| Polarizability volumes <sup>4</sup> (Å <sup>3</sup> )       | static: $\alpha_{aa}=20.9$ , $\alpha_{bb}=15.0$ ,<br>$\alpha_{cc}=10.1$<br>1064 nm: $\alpha_{aa}=21.3$ , $\alpha_{bb}=15.2$ ,<br>$\alpha_{cc}=10.2$<br>800 nm: $\alpha_{aa}=21.5$ , $\alpha_{bb}=15.3$ ,<br>$\alpha_{cc}=10.2$ | static: $\alpha_{aa}=20.6$ , $\alpha_{bb}=14.8$ ,<br>$\alpha_{cc}=9.6$<br>1064 nm: $\alpha_{aa}=20.9$ , $\alpha_{bb}=15.0$ ,<br>$\alpha_{cc}=9.6$<br>800 nm: $\alpha_{aa}=21.1$ , $\alpha_{bb}=15.1$ ,<br>$\alpha_{cc}=9.7$ |

<sup>1</sup>At atmospheric pressure.<sup>2</sup>at seed temperature, calculated using the Clausius-Clayperon equation[105], $P(T) = P_{atm} \exp(-\Delta_{vap}H/R * (\frac{1}{T} - \frac{1}{T_{boil}}))$ , vaporization enthalpies obtained from [99].<sup>3</sup> $t_J = (2B)^{-1}$ <sup>4</sup>The polarizability volume  $\alpha'$  relates to the polarizability  $\alpha$  as:  $\alpha' = \alpha/(4\pi\epsilon_0)$ . The values are obtained using an ab-initio linear response calculation on a HF wavefunction in the Sadlej basiset using the Dalton Quantum Chemistry Program: [www.kjemi.uio.no/software/dalton](http://www.kjemi.uio.no/software/dalton). The molecular geometry was not optimized. For all the molecules the near-infrared wavelengths are far off resonance and the polarizabilities close to the static values.<sup>5</sup>Characteristic (not molecule specific) bondlengths<sup>6</sup>C-I bondlength chosen to fit rotational constants.<sup>7</sup> $\kappa = \frac{2B-A-C}{A-C}$ ,  $\kappa = -1$  for a prolate and  $\kappa = 1$  for an oblate symmetric top.<sup>8</sup> $t_C = (4C)^{-1}$ ,  $t_J = (B + C)^{-1}$

## A.3 Asymmetric top molecules of general type

| Names   | Ethyl iodide<br>Iodoethane   | Propyl iodide<br>1-iodopropane   |
|---|--|--|
| Molecular formula   | C <sub>2</sub> H <sub>5</sub> I  | C <sub>3</sub> H <sub>7</sub> I  |
| Molecular weight (g/mole)   | 155.97   | 169.99   |
| Structure   |   |   |
| Bond lengths and angles   | [106]  | [76] <sup>9</sup>  |
| Boiling temperature <sup>1</sup>  | 73°C[98]   | 102°C[98]  |
| Seed temperature  | -25°C  | 0°C  |
| Vapor pressure <sup>2</sup> (mbar)  | 13   | 13   |
| Gas phase absorption cross section (Å <sup>2</sup> )                                    | 266 nm: 1.4×10 <sup>-2</sup><br>304 nm: 4×10 <sup>-4</sup> [101]   | 266 nm: 1.8×10 <sup>-2</sup><br>305 nm: 7×10 <sup>-4</sup> [101] <sup>10</sup>   |
| Rotational constants (MHz)<br>asymmetry parameter <sup>7</sup><br>δ angle <sup>11</sup> | A=29116.33, B=2979.566,<br>C=2796.451, κ=-0.986<br>δ=19.7°[106]  | trans: A=24710.74, B=1305.204,<br>C=1269.366, κ=-0.997, δ=19.4°<br>gauche: A=10595.35, B=1781.651,<br>C=1614.186, κ=-0.963, δ=32.6°<br>[107, 76]   |
| Revival times (ps) <sup>8</sup>   | t <sub>C</sub> =89.40, t <sub>J</sub> =173.13  | trans: t <sub>C</sub> =196.95, t <sub>J</sub> =388.41<br>gauche: t <sub>C</sub> =154.88, t <sub>J</sub> =294.48  |
| Polarizability volumes <sup>4,12</sup> (Å <sup>3</sup> )                                | static:<br>α <sub>zz</sub> =11.2, α <sub>yy</sub> =8.0,<br>α <sub>xx</sub> =7.7, δ <sub>pol</sub> =13.6°<br>800 nm:<br>α <sub>zz</sub> =11.5, α <sub>yy</sub> =8.2,<br>α <sub>xx</sub> =7.8, δ <sub>pol</sub> =13.6° | <u>trans</u> : <u>gauche</u> :<br>static: α <sub>zz</sub> =14.3,    α <sub>zz</sub> =13.2,<br>α <sub>yy</sub> =9.5,    α <sub>yy</sub> =9.8,<br>α <sub>xx</sub> =9.1,    α <sub>xx</sub> =9.2,<br>δ <sub>pol</sub> =19.3°    δ <sub>pol</sub> =19.3°<br>800nm: α <sub>zz</sub> =14.6,    α <sub>zz</sub> =13.8,<br>α <sub>yy</sub> =9.6,    α <sub>yy</sub> =10.2,<br>α <sub>xx</sub> =9.3,    α <sub>xx</sub> =9.6,<br>δ <sub>pol</sub> =19.3°    δ <sub>pol</sub> =19.3° |

<sup>9</sup>Ref. [76] only report 23 out of the necessary 27 internal coordinates for gauche-propyl iodide. Assumptions were made for the remaining four that fit with the reported rotational constants.

<sup>10</sup>Values for isopropyl iodide

<sup>11</sup>δ is the angle between the principal axis of inertia (a-axis) and the C-I bond axis.

<sup>12</sup>The principal axes of polarizability are located so that the x-axis is perpendicular to the I-C1-C2 plane and the z-axis is the axis closest to the C-I bond axis. δ<sub>pol</sub> is the angle between the z-axis and the C-I bond axis.

# Appendix B

## Laser beam parameters

This appendix contains a description of how we obtain the different parameters characterizing the laser beams. I have used the definitions of [108].

### **Pulse Energy, $E_{pulse}$**

The pulse energy,  $E_{pulse}$ , is measured with a standard laser powermeter. The measured power is divided by the repetition rate of the laser to obtain the pulse energy.

### **Focal spot size, $\omega_0$**

We have measured the focal spot sizes of the laser beams by inserting a broadband mirror before the chamber window and placing a 10  $\mu\text{m}$  pinhole at the focus of the beams. A photo diode is placed after the pinhole. By measuring the photo diode signal as a function of the pinhole position the focal spot size can be measured.

This method depends on the pinhole being smaller than the focal spot size of the laser beams. Figure B.1 shows the relation between measured

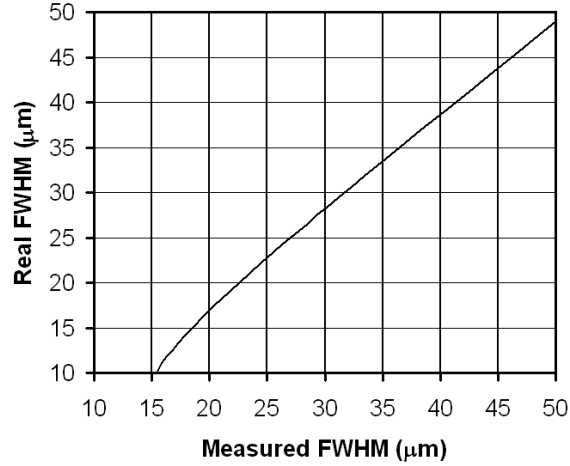


Figure B.1: Relation between the measured and real focal spot size (FWHM<sup>1</sup>) for a 10  $\mu\text{m}$  pinhole. The beam profile was assumed gaussian and it was assumed that all light passing through the pinhole meets the photo diode.

and real spot size for a 10  $\mu\text{m}$  pinhole. We have used the measured spot size directly rather than using fig. B.1 to correct for the finite size of the pinhole. The reason is that the photo diode is only 0.5 mm wide and mounted 2 cm after the pinhole. We are therefore not certain all the light transmitted (and diffracted) through the pinhole meets the photodiode. As a result the effective size of the pinhole may be smaller than 10  $\mu\text{m}$ .

Assuming a gaussian beam profile,  $I(r) = I_0 \exp(-2r^2/\omega_0^2)$ ,  $r$  being the distance from the center of the beam,  $\omega_0$  can be calculated from the FWHM<sup>1</sup> as

$$\omega_0 = \frac{\text{FWHM}}{\sqrt{2 \ln 2}}. \quad (\text{B.1})$$

<sup>1</sup>FWHM is the Full Width at Half Maximum of the signal.

Since the molecular beam is only 1 mm across spot sizes can with a good approximation be assumed constant through the molecular beam.

### Fluence, $\phi_0$

Assuming a gaussian beam profile we can calculate the peak fluence integrated over time (energy per unit area) as

$$\phi_0 = \frac{E_{pulse}}{\frac{\pi}{2}\omega_0^2}. \quad (\text{B.2})$$

The focal averaged fluence is  $\frac{1}{2}$  of the peak fluence.

### Photon flux, $\Phi_0$

All the laser beams have sufficiently narrow spectra to calculate the photon flux integrated over time (photons per unit area) from the fluence as

$$\Phi_0 = \frac{\phi_0}{h\nu_{laser}}. \quad (\text{B.3})$$

### Pulse duration, $\tau$

The pulse durations of the nanosecond pulses are measured with a fast photodiode. If the response time of the photodiode is much faster than the duration of the laser pulse, the time evolution of the photo diode signal reflects the time evolution of the intensity envelope of the pulse.

The pulse durations of the femto- and picosecond pulses are measured by making 400 nm light in a BBO crystal. Either through difference frequency mixing (800 nm and 266 nm) or sum frequency mixing (two 800 nm beams). The generated 400 nm light pass through a bandpass filter and is measured by a photo diode. The photo diode signal as a function of the delay between

the two involved pulses is the cross correlation signal. Assuming gaussian pulse envelope,  $I(t) = I_0 \exp(-2t^2/\tau^2)$ , the width of the cross correlation signal is related to the duration of the pulses as

$$\tau_{measured}^2 = \tau_1^2 + \tau_2^2. \quad (\text{B.4})$$

Assuming a gaussian pulse envelope the relation between  $\tau$  and  $\tau_{FWHM}$  is

$$\tau = \frac{\tau_{FWHM}}{\sqrt{2 \ln 2}}. \quad (\text{B.5})$$

### Peak intensity, $I_0$

The peak intensity can be calculated from the peak fluence and the pulse duration (assuming gaussian pulse envelope),

$$I_0 = \frac{\phi_0}{\sqrt{\frac{\pi}{2}} \tau} = \frac{\phi_0}{\sqrt{\frac{\pi}{4 \ln 2}} \tau_{FWHM}}. \quad (\text{B.6})$$

The main source of uncertainty in the peak intensities quoted in our work is in the determination of the focal spot size, which has an uncertainty of  $\sim 10\%$  corresponding to an uncertainty of  $\sim 20\%$  on the peak intensity.

## Appendix C

# Dissociation probabilities of iodobenzene

In this appendix the expressions for the dissociation probabilities of iodobenzene are derived. The derivation is general and the expressions can be used for all molecules with the same dissociation channels.

### C.1 Dissociation probability and the Beer-Lambert law

The absorption cross section,  $\sigma$ , is defined so that the probability that a molecule absorbs a photon,  $P_{abs}$ , in the low field limit (no saturation) is

$$P_{abs} = \sigma\Phi_0, \tag{C.1}$$

where  $\Phi_0$  is the photon flux (photons per unit area). A consequence of eq. C.1 is the well known Beer-Lambert law<sup>[105]</sup> for absorption in a ran-

domly distributed sample of molecules,

$$\frac{I}{I_0} = \exp(-\sigma x \frac{N}{V}) = \exp(-\frac{\sigma N}{\mathcal{A}}). \quad (\text{C.2})$$

In eq. C.2  $I_0$  and  $I$  are the intensity (energy per unit area and time) of the light before and after passing through the sample,  $x$  is the length of the sample, and  $N/V$  is the sample density (molecules per unit volume).  $V/x = \mathcal{A}$ , where  $\mathcal{A}$  is the considered area perpendicular to the beam direction. Replacing the exponential of the Beer-Lambert law with its first order expansion eq. C.1 is obtained.

So far a uniform distribution of the molecules have been assumed. To account for the dependence of absorption on molecular orientation the angular dependence function,  $N(\theta, \phi, \chi)$ , is introduced.  $N(\theta, \phi, \chi)$  is the transition dipole moment in lab-fixed coordinates normalized to 1 for a uniform distribution.

Taking the angular dependence into account eq. C.1 becomes

$$P_{abs}(\theta, \phi, \chi) = \sigma \Phi_0 N(\theta, \phi, \chi). \quad (\text{C.3})$$

As discussed in sect. 4.3 the photo dissociation of iodobenzene at 266 nm can go through two different channels, the  $n \rightarrow \sigma^*$  and  $\pi \rightarrow \pi^*$  channels. The angular dependence function for these two pathways is different and it is therefore useful to recast eq. C.3 as

$$P_{diss} = \sigma_{n \rightarrow \sigma^*} \Phi_0 N(\theta, \phi, \chi)^{n \rightarrow \sigma^*} + \sigma_{\pi \rightarrow \pi^*} \Phi_0 N(\theta, \phi, \chi)^{\pi \rightarrow \pi^*}. \quad (\text{C.4})$$

In eq. C.4  $P_{abs}$  is replaced by  $P_{diss}$  since the transition of interest, the absorption of a 266 nm photon always lead to dissociation of iodobenzene.

## C.2 Angular dependence of the dissociation

To find expressions for  $N(\theta, \phi, \chi)$  expressions for the molecular axes in space-fixed coordinates are needed. The direction vector of the C-I bond axis,  $\vec{a}$ , of the molecule (the z-axis) is

$$\vec{a} = \Phi^{-1} \begin{pmatrix} 0 \\ 0 \\ 1 \end{pmatrix} = \begin{pmatrix} \sin \theta \cos \phi \\ \sin \theta \sin \phi \\ \cos \theta \end{pmatrix}. \quad (\text{C.5})$$

The other molecular axis needed is the direction vector perpendicular to the molecular plane,  $\vec{n}$ ,

$$\vec{n} = \Phi^{-1} \begin{pmatrix} 1 \\ 0 \\ 0 \end{pmatrix} = \begin{pmatrix} \cos \theta \cos \phi \sin \chi - \sin \phi \cos \chi \\ \cos \theta \sin \phi \sin \chi + \cos \phi \cos \chi \\ -\sin \theta \sin \chi \end{pmatrix}. \quad (\text{C.6})$$

The direction vector of the dissociation pulse polarization is named  $\vec{d}$ . The polarization of the dissociation pulse is either parallel or perpendicular to the lab-fixed Z-axis, the (major) alignment axis,

$$\text{Parallel: } \vec{d} = \begin{pmatrix} 0 \\ 0 \\ 1 \end{pmatrix} \quad \text{Perpendicular: } \vec{d} = \begin{pmatrix} 1 \\ 0 \\ 0 \end{pmatrix}. \quad (\text{C.7})$$

The transitions depend either on  $\alpha$ , the angle between  $\vec{a}$  and  $\vec{d}$  or  $\gamma$ , the angle between  $\vec{n}$  and  $\vec{d}$ ,

$$\cos \alpha = \vec{a} \cdot \vec{d} \quad \cos \gamma = \vec{n} \cdot \vec{d} \quad (\text{C.8})$$

### C.2.1 The $n \rightarrow \sigma^*$ channel

Direct excitation of the C-I bond, the  $n \rightarrow \sigma^*$  channel, is predominantly parallel with a minor perpendicular component. The angular dependence of the parallel part is  $\cos^2 \alpha$  and the dependence of the perpendicular part is  $\sin^2 \alpha$ ,

$$N(\theta, \phi, \chi)^{n \rightarrow \sigma^*} = \frac{3}{2-A} \left( \cos^2 \alpha + (1-A) \sin^2 \alpha \right). \quad (\text{C.9})$$

In eq. C.9 the  $A$  parameter is 1 for a pure parallel transition and 0 for a pure perpendicular transition. The prefactor  $\frac{3}{2-A}$  normalize the expression.

When the dissociation pulse is polarized parallel to the Z-axis (using eq. C.8)

$$N(\theta, \phi, \chi)_{para}^{n \rightarrow \sigma^*} = \frac{3}{2-A} \left( \cos^2 \theta + (1-A) \sin^2 \theta \right). \quad (\text{C.10})$$

It is worth noting that eq. C.10 is equivalent to the commonly used expression[28]

$$N(\theta, \phi, \chi)_{para}^{n \rightarrow \sigma^*} = 1 + \beta P_2(\cos \theta) = 1 + \beta \left( \frac{3}{2} \cos^2 \theta - \frac{1}{2} \right). \quad (\text{C.11})$$

In eq. C.11  $\beta$  is 2 for a pure parallel transition and -1 for a pure perpendicular transition. The relation between  $A$  and  $\beta$  parameters is

$$\beta = \frac{4A-2}{2-A} \Leftrightarrow A = \frac{2+2\beta}{4+\beta}. \quad (\text{C.12})$$

For dissociation pulse polarization perpendicular to the Z-axis the angular dependence function is

$$N(\theta, \phi, \chi)_{perp}^{n \rightarrow \sigma^*} = \frac{3}{2-A} \left( A \sin^2 \theta \cos^2 \phi + (1-A)(1 - \sin^2 \theta \cos^2 \phi) \right). \quad (\text{C.13})$$

Assuming a uniform distribution of  $\phi$  for all  $\theta$ , eq.C.13 becomes

$$N(\theta)_{perp}^{n \rightarrow \sigma^*} = \frac{3}{2-A} \left( \frac{1}{2} A \sin^2 \theta + (1-A) \left(1 - \frac{1}{2} \sin^2 \theta\right) \right). \quad (C.14)$$

### C.2.2 The $\pi \rightarrow \pi^*$ channel

The excitation of the aromatic ring, the  $\pi \rightarrow \pi^*$  channel, is a planar transition. The angular dependence is therefore proportional to  $\sin^2 \gamma$ , which means

$$N(\theta, \phi, \chi)^{\pi \rightarrow \pi^*} = \frac{3}{2} (1 - \cos^2 \gamma). \quad (C.15)$$

For dissociation pulse polarization parallel to the Z-axis (using eq. C.8)

$$N(\theta, \phi, \chi)_{para}^{\pi \rightarrow \pi^*} = \frac{3}{2} (1 - \sin^2 \theta \sin^2 \chi). \quad (C.16)$$

Assuming a uniform distribution of  $\chi$  for all  $\theta$  eq. C.16 becomes

$$N(\theta)_{para}^{\pi \rightarrow \pi^*} = \frac{3}{2} \left(1 - \frac{1}{2} \sin^2 \theta\right). \quad (C.17)$$

For dissociation pulse polarization perpendicular to the Z-axis the angular dependence function is

$$N(\theta, \phi, \chi)_{perp}^{\pi \rightarrow \pi^*} = \frac{3}{2} \left( 1 - \cos^2 \theta \cos^2 \phi \sin^2 \chi - \sin^2 \phi \cos^2 \chi + \frac{1}{2} \cos \theta \sin(2\phi) \sin(2\chi) \right). \quad (C.18)$$

The last term in eq. C.18 is always averaged to zero. Since the molecules are aligned and not oriented,  $f_{mol}(\theta, \phi, \chi) = f_{mol}(\pi - \theta, \phi, \chi)$ . The  $\cos \theta$  factor is therefore averaged to zero.

Assuming a uniform distribution of  $\phi$  for all  $\theta$  and  $\chi$ , eq. C.18 becomes

$$N(\theta, \chi)_{\text{perp}}^{\pi \rightarrow \pi^*} = \frac{3}{4}(1 + \sin^2 \theta \sin^2 \chi). \quad (\text{C.19})$$

Furthermore assuming a uniform distribution of  $\chi$  for all  $\theta$ , eq. C.19 becomes

$$N(\theta)_{\text{perp}}^{\pi \rightarrow \pi^*} = \frac{3}{4}\left(1 + \frac{1}{2} \sin^2 \theta\right). \quad (\text{C.20})$$

# Summary

The orientation of molecules with respect to space fixed axes play a central role in chemistry and spectroscopy. This thesis deals with an effective method of controlling the rotational motion of gas-phase molecules, laser induced alignment. When a molecule is subject to a strong nonresonant polarized laser field, the rotational state of the molecule is changed so that its principal axes of polarization are confined along the polarization of the laser field – the molecule has become aligned.

Laser induced alignment is a very general method that can be applied to almost all molecules and the molecular axes can become very well confined. The method does not distinguish between ‘head’ and ‘tail’ of the molecules, which is why the term ‘alignment’ rather than ‘orientation’ is used.

The duration of the alignment laser pulse is determining how the molecular alignment progress. If the alignment pulse is long compared to molecular rotation the alignment evolves adiabatically. In that case, the degree of molecular alignment follows the intensity profile of the alignment pulse. If the alignment pulse is short compared molecular rotation the molecules can be aligned under field-free conditions after the alignment pulse. Furthermore, the rotational wave packet created by a short (non-adiabatic) alignment pulse exhibits narrow revivals of alignment at regular intervals

long after the alignment pulse. The timing of these revivals is determined by the rotational constants of the molecule. The work presented in this thesis deals with both adiabatic and non-adiabatic laser induced alignment. Moreover, the effect of combining long and short pulses is treated.

### **Adiabatic alignment**

Adiabatic alignment of the asymmetric top iodobenzene molecule was demonstrated. A method of obtaining the distribution of molecules prior to the probe pulse and a quantitative measure of alignment was demonstrated. The degree of alignment increases with increasing laser pulse intensity and with a decrease of the rotational temperature.

Alignment was used to control photodissociation pathways. The two dissociation channels of iodobenzene at 266 nm depend differently on the relative orientation of molecule and dissociation pulse polarizability. Control of the molecular orientation therefore allows control of the photodissociation.

### **Non-adiabatic alignment**

Non-adiabatic alignment was demonstrated for several molecules. Field-free alignment was obtained both immediately after the alignment pulse and at rotational revivals. The degree of alignment increases with increasing laser pulse intensity and with a decrease of the rotational temperature. A significant enhancement of alignment was obtained by using a sequence of two pulses rather than a single alignment pulse.

Spectra of rotational revivals were recorded for both symmetric and asymmetric top molecules. The effects of molecular asymmetry and laser intensity were investigated. The rotational revivals of non-adiabatic align-

ment are useful for time resolved rotational spectroscopy and supplement other such techniques. Furthermore, rotational revivals of individual conformers of the propyl iodide molecule were observed. These revivals can be used to separate conformers.

### **Combining adiabatic and non-adiabatic alignment**

It was demonstrated that molecular alignment is significantly enhanced when long and short alignment pulses are combined. The combined fields alignment was much stronger than that obtained by either field alone. The degree of combined fields alignment is increased with an increase of the intensity of either pulse.

# Bibliography

- [1] M. D. Poulsen, E. Skovsen, and H. Stapelfeldt, *Photodissociation of laser aligned iodobenzene: Towards selective photoexcitation*, J. Chem. Phys. **117** (2002), 2097–2102.
- [2] E. Péronne, M. D. Poulsen, C. Z. Bisgaard, H. Stapelfeldt, and T. Seideman, *Nonadiabatic alignment of asymmetric top molecules: Field-free alignment of iodobenzene*, Phys. Rev. Lett. **91** (2003), 043003.
- [3] E. Péronne, M. D. Poulsen, H. Stapelfeldt, C. Z. Bisgaard, E. Hamilton, and T. Seideman, *Nonadiabatic laser-induced alignment of iodobenzene molecules*, Phys. Rev. A **70** (2004), 063410.
- [4] C. Z. Bisgaard, M. D. Poulsen, E. Péronne, S. S. Viftrup, and H. Stapelfeldt, *Observation of enhanced field-free molecular alignment by two laser pulses*, Phys. Rev. Lett. **92** (2004), 173004.
- [5] M. D. Poulsen, E. Péronne, H. Stapelfeldt, C. Z. Bisgaard, S. S. Viftrup, E. Hamilton, and T. Seideman, *Nonadiabatic alignment of asymmetric top molecules: Rotational revivals*, J. Chem. Phys. **121** (2004), 783–791.

- [6] T. Ejdrup, M. D. Poulsen, C. Z. Bisgaard, S. S. Viftrup, H. Stapelfeldt, E. Hamilton, and T. Seideman, *Laser induced alignment of symmetric top molecules* (Manuscript in preparation).
- [7] M. D. Poulsen, T. Ejdrup, H. Stapelfeldt, E. Hamilton, and T. Seideman, *Alignment of molecules by a long and a short laser pulse* (Manuscript in preparation).
- [8] J. McMurry, *Fundamentals of organic chemistry*, 3rd edition, Brooks/Cole Publishing Company, 1994.
- [9] H. J. Loesch, J. Bulthuis, S. Stolte, A. Durand, J. C. Loison, and J. Vigué, *Molecules oriented by brute force*, *Europhys. News* **27** (1996), 12–15.
- [10] H. L. Bethlem and G. Meijer, *Production and application of translationally cold molecules*, *Int. Rev. Phys. Chem.* **22** (2003), 73–128.
- [11] K. J. Franks, H. Li, R. J. Hanson, and W. Kong, *Selective excitation of ICN achieved via brute force orientation*, *J. Phys. Chem. A* **102** (1998), 7881–7884.
- [12] W. Kong, *Studies of electronic properties of medium and large molecules oriented in a strong uniform electric field*, *Int. J. Mod. Phys. B* **15** (2001), 3471–3502.
- [13] J. E. Abbott, X. Peng, and W. Kong, *Symmetry properties of electronically excited states of nitroaromatic compounds*, *J. Chem. Phys.* **117** (2002), 8670–8675.
- [14] D. H. Parker and R. B. Bernstein, *Oriented molecule beams via the electrostatic hexapole: Preparation, characterization, and reactive scattering*, *Annu. Rev. Phys. Chem.* **40** (1989), 561–595.

- [15] P. W. Harland and P. R. Brooks, *Dramatic steric behavior in electron transfer from various donors to CF<sub>3</sub>Br*, *J. Am. Chem. Soc.* **125** (2003), 13191–13197.
- [16] M. P. Hughes, *AC electrokinetics: applications for nanotechnology*, *Nanotechnology* **11** (2000), 124–132.
- [17] W. A. Germishuizen, C. Wälti, R. Wirtz, M. B. Johnston, M. Pepper, A. G. Davies, and A. P. J. Middelberg, *Selective dielectrophoretic manipulation of surface-immobilized DNA molecules*, *Nanotechnology* **14** (2003), 896–902.
- [18] P. M. Felker and A. H. Zewail, *Molecular structures from ultrafast coherence spectroscopy*, in *Femtosecond Chemistry*, (J. Manz and L. Woeste, eds.), VCH Weinheim, 1995, pp. 193–260.
- [19] C. Riehn, *High-resolution pump-probe rotational coherence spectroscopy – rotational constants and structure of ground and electronically excited states of large molecular systems*, *Chem. Phys.* **283** (2002), 297–329.
- [20] Y. R. Shen, *The Principles of Nonlinear Optics*, John Wiley & Sons, Inc., 1984.
- [21] R. Righini, *Ultrafast optical kerr effect in liquids and solids*, *Science* **262** (1993), 1386–1390.
- [22] A. Idrissi, M. Ricci, P. Bartolini, and R. Righini, *Optical Kerr-effect investigation of the reorientational dynamics of CS<sub>2</sub> in CCl<sub>4</sub> solutions*, *J. Chem. Phys.* **111** (1999), 4148–4152.

- [23] K. Visscher, M. J. Schnitzer, and S. M. Block, *Single kinesin molecules studied with a molecular force clamp*, Nature **400** (1999), 184–189.
- [24] M. Irving and Y. E. Goldman, *Motor proteins - another step ahead for myosin*, Nature **398** (1999), 463.
- [25] N. B. Simpson, K. Dholakia, L. Allen, and M. J. Padgett, *Mechanical equivalence of spin and orbital angular momentum of light: an optical spanner*, Optics Lett. **22** (1997), 52–54.
- [26] M. P. Sinha, C. D. Caldwell, and R. N. Zare, *Alignment of molecules in gaseous transport: Alkali dimers in supersonic nozzle beams*, J. Chem. Phys. **61** (1974), 491–503.
- [27] F. Pirani, D. Cappalletti, M. Bartolomei, V. Aquilanti, M. Scotoni, M. Vescovi, D. Ascenzi, and D. Bassi, *Orientation of benzene in supersonic expansions, probed by IR-laser absorption and by molecular beam scattering*, Phys. Rev. Lett. **86** (2001), 5035–5038.
- [28] R. N. Zare, *Angular Momentum*, John Wiley & Sons, 1988.
- [29] B. Friedrich and D. Herschbach, *Alignment and trapping of molecules in intense laser fields*, Phys. Rev. Lett. **74** (1995), 4623–4626.
- [30] V. Renard, M. Renard, S. Guérin, Y. T. Pashayan, B. Lavorel, O. Faucher, and H. R. Jauslin, *Postpulse molecular alignment measured by a weak field polarization technique*, Phys. Rev. Lett. **90** (2003), 153601.
- [31] P. W. Dooley, I. V. Litvinyuk, K. F. Lee, D. M. Rayner, M. Spanner, D. M. Villeneuve, and P. B. Corkum, *Direct imaging of rotational*

- wave-packet dynamics of diatomic molecules*, Phys. Rev. A **68** (2003), 023406.
- [32] J. J. Larsen, K. Hald, N. Bjerre, H. Stapelfeldt, and T. Seideman, *Three dimensional alignment of molecules using elliptically polarized laser fields*, Phys. Rev. Lett. **85** (2000), 2470–2473.
- [33] J. G. Underwood, B. J. Sussman, and A. Stolow *Approaches to field-free three dimensional molecular axis alignment*, 2005 (Preprint, to appear in Phys. Rev. Lett.).
- [34] P. W. Atkins and R. S. Friedman, *Molecular Quantum Mechanics*, 3rd edition, Oxford University Press, 1997.
- [35] T. Seideman, *On the dynamics of rotationally broad, spatially aligned wave packets*, J. Chem. Phys. **115** (2001), 5965–5973.
- [36] J. G. Underwood, M. Spanner, M. Y. Ivanov, J. Mottershead, B. J. Sussman, and A. Stolow, *Switched wave packets: A route to nonperturbative quantum control*, Phys. Rev. Lett. **90** (2003), 223001.
- [37] J. Ortigoso, M. Rodríguez, M. Gupta, and B. Friedrich, *Time evolution of pendular states created by the intereaction of molecular polarizability with a pulsed nonresonant laser field*, J. Chem. Phys. **110** (1999), 3870–3875.
- [38] H. Stapelfeldt and T. Seideman, *Aligning molecules with strong laser pulses*, Rev. Mod. Phys. **75** (2003), 543–557.
- [39] M. Machholm, *Postpulse alignment of molecules robust to thermal averaging*, J. Chem. Phys. **115** (2001), 10724–10730.

- 
- [40] J. J. Larsen, *Laser Induced Alignment of Neutral Molecules*, PhD thesis, Institute of Physics and Astronomy, University of Aarhus, Denmark, 2000.
- [41] M. Leibscher, I. S. Averbukh, and H. Rabitz, *Molecular alignment by trains of short laser pulses*, Phys. Rev. Lett. **90** (2003), 213001.
- [42] M. Leibscher, I. S. Averbukh, and H. Rabitz, *Enhanced molecular alignment by short laser pulses*, Phys. Rev. A **69** (2004), 013402.
- [43] W. R. Gentry and C. F. Giese, *Ten-microsecond pulsed molecular beam source and a fast ionization detector*, Rev. Sci. Instrum. **49** (1978), 595–600.
- [44] M. D. Poulsen *Guide to operation of the vacuum chamber*, June 2003 (Private circulation, Femtolab, University of Aarhus).
- [45] J. Olsen *Generation of sub 20 femtosecond laser pulses and coulomb explosion studies of D<sub>2</sub>* Master's thesis, Department of Chemistry, University of Aarhus, 1999.
- [46] A. T. J. B. Eppink and D. H. Parker, *Velocity map imaging of ions and electrons using electrostatic lenses: Application in photoelectron and photofragment ion imaging of molecular oxygen*, Rev. Sci. Instrum. **68** (1997), 3477–3484.
- [47] M. D. Poulsen *User's guide to data processing of ion images v3.1*, August 2004 (Private circulation, Femtolab, University of Aarhus).
- [48] V. Dribinski, A. Ossadtchi, V. A. Mandelshtam, and H. Reisler, *Reconstruction of Abel-transformable images: The basis-set expansion Abel transform method*, Rev. Sci. Instrum. **73** (2002), 2634–2642.

- [49] M. J. J. Vrakking, *An iterative procedure for the inversion of two-dimensional ion/photoelectron imaging experiments*, Rev. Sci. Instrum. **72** (2001), 4084–4089.
- [50] B. A. Zon and B. G. Katsnel'son, *Nonresonant scattering of intense light by a molecule*, Soviet Phys. JETP **42** (1976), 595–599.
- [51] W. Kim and P. M. Felker, *Spectroscopy of pendular states in optical-field-aligned species*, J. Chem. Phys. **104** (1996), 1147–1150.
- [52] H. Sakai, C. P. Safvan, J. J. Larsen, K. M. Hillingsøe, K. Hald, and H. Stapelfeldt, *Controlling the alignment of neutral molecules by a strong laser field*, J. Chem. Phys. **110** (1999), 10235–10238.
- [53] J. J. Larsen, H. Sakai, C. P. Safvan, I. Wendt-Larsen, and H. Stapelfeldt, *Aligning molecules with intense nonresonant laser fields*, J. Chem. Phys. **111** (1999), 7774–7781.
- [54] J. J. Larsen, I. Wendt-Larsen, and H. Stapelfeldt, *Controlling the branching ratio of photodissociation using aligned molecules*, Phys. Rev. Lett. **83** (1999), 1123–1126.
- [55] A. T. J. B. Eppink and D. H. Parker, *Methyl iodide A-band decomposition study by photofragment velocity imaging*, J. Chem. Phys. **109** (1998), 4758–4767.
- [56] J. R. Nestor, *Optogalvanic spectra of neon and argon in glow discharge lamps*, Appl. Optics **21** (1982), 4154–4157.
- [57] J. A. Griffiths, K.-W. Jung, and M. A. El-Sayed, *Fluorine substitution effects on the photodissociation dynamics of iodobenzene at 304 nm*, J. Phys. Chem. **100** (1996), 7989–7996.

- [58] J. E. Freitas, H. J. Hwang, and M. A. El-Sayed, *Molecular rotation clocking of the subpicosecond energy redistribution in molecules falling apart. 2. Excess energy dependence of the rates of energy redistribution in the two photodissociation channels of iodobenzene*, J. Phys. Chem. **97** (1993), 12481–12484.
- [59] A. T. J. B. Eppink and D. H. Parker, *Energy partitioning following photodissociation of methyl iodide in the A band: A velocity mapping study*, J. Chem. Phys. **110** (1999), 832–844.
- [60] P. Y. Cheng, D. Zhong, and A. H. Zewail, *Kinetic-energy, femtosecond resolved reaction dynamics. modes of dissociation (in iodobenzene) from time-velocity correlations*, Chem. Phys. Lett. **237** (1995), 399–405.
- [61] T. Seideman, *Rotational excitation and molecular alignment in intense laser fields*, J. Chem. Phys. **103** (1995), 7887–7896.
- [62] F. Rosca-Pruna and M. J. J. Vrakking, *Experimental observation of revival structures in picosecond laser-induced alignment of I<sub>2</sub>*, Phys. Rev. Lett. **87** (2001), 153902.
- [63] F. Rosca-Pruna and M. J. J. Vrakking, *Revival structures in picosecond laser-induced alignment of I<sub>2</sub> molecules. I. Experimental results*, J. Chem. Phys. **116** (2002), 6567–6578.
- [64] F. Rosca-Pruna and M. J. J. Vrakking, *Revival structures in picosecond laser-induced alignment of I<sub>2</sub> molecules. II. Numerical modelling*, J. Chem. Phys. **116** (2002), 6579–6588.
- [65] H. M. Frey, P. Beaud, T. Gerber, B. Mischler, P. P. Radi, and A. P. Tzannis, *Femtosecond nonresonant degenerate four-wave mixing at*

- atmospheric pressure and in a free jet*, Appl. Phys. B **68** (1999), 735–739.
- [66] H. M. Frey, P. Beaud, T. Gerber, B. Mischler, P. P. Radi, and A. P. Tzannis, *Determination of rotational constants in a molecule by femtosecond four-wave mixing*, J. Raman Spectrosc. **31** (2000), 71–76.
- [67] M. M. Wefers and K. A. Nelson, *Programmable phase and amplitude femtosecond pulse shaping*, Optics Lett. **18** (1993), 2032–2034.
- [68] A. M. Weiner, *Femtosecond pulse shaping using spatial light modulators*, Rev. Sci. Instrum. **71** (2000), 1929–1960.
- [69] I. S. Averbukh and R. Arvieu, *Angular focusing, squeezing, and rainbow formation in a strongly driven quantum rotor*, Phys. Rev. Lett. **87** (2001), 163601.
- [70] K. F. Lee, I. V. Litvinyuk, P. W. Dooley, M. Spanner, D. M. Villeneuve, and P. B. Corkum, *Two-pulse alignment of molecules*, J. Phys. B **37** (2004), L43–L48.
- [71] C. H. Lin, J. P. Heritage, and T. K. Gustafson, *Susceptibility echos in linear molecular gases*, Appl. Phys. Lett. **19** (1971), 397–400.
- [72] J. P. Heritage, T. K. Gustafson, and C. H. Lin, *Observation of coherent transient birefringence in CS<sub>2</sub> vapor*, Phys. Rev. Lett. **34** (1975), 1299–1302.
- [73] P. M. Felker, *Rotational coherence spectroscopy: Studies of the geometries of large gas-phase species by picosecond time-domain methods*, J. Phys. Chem. **96** (1992), 7844–7857.

- [74] V. V. Matylitsky, W. Jarzęba, C. Riehn, and B. Brutschy, *Femtosecond degenerate four-wave mixing study of benzene in the gas phase*, J. Raman Spec. **33** (2002), 877–883.
- [75] W. Jarzęba, V. V. Matylitsky, C. Riehn, and B. Brutschy, *Rotational coherence spectroscopy of jet-cooled molecules by femtosecond degenerate four-wave mixing: non-rigid symmetric and asymmetric tops*, Chem. Phys. Lett. **368** (2003), 680–689.
- [76] Y. Niide, I. Ohkoshi, and M. Takano, *Microwave spectrum, conformation, and quadrupole coupling constants of 1-iodopropane*, J. Mol. Spec. **122** (1987), 113–129.
- [77] U. Even, J. Jortner, D. Noy, N. Lavie, and C. Cossart-Magos, *Cooling of large molecules below 1 K and He clusters formation*, J. Chem. Phys. **112** (2000), 8068–8071.
- [78] M. Hillenkamp, S. Keinan, and U. Even, *Condensation limited cooling in supersonic expansions*, J. Chem. Phys. **118** (2003), 8699–8705.
- [79] C. R. Gebhardt, T. P. Rakitzis, P. C. Samartzis, V. Ladopoulos, and T. N. Kitsopoulos, *Slice imaging: A new approach to ion imaging and velocity mapping*, Rev. Sci. Instrum. **72** (2001), 3848–3853.
- [80] R. S. Judson and H. Rabitz, *Teaching laser to control molecules*, Phys. Rev. Lett. **68** (1992), 1500–1503.
- [81] M. Machholm and N. E. Henriksen, *Field-free orientation of molecules*, Phys. Rev. Lett. **87** (2001), 193001.
- [82] M. Spanner, E. A. Shapiro, and M. Ivanov, *Cohesrent control of rotational wave-packet dynamics via fractional revivals*, Phys. Rev. Lett. **92** (2004), 093001.

- [83] B. Friedrich and D. Herschbach, *Manipulating molecules via combined static and laser fields*, J. Phys. Chem. A **103** (1999), 10280–10288.
- [84] B. Friedrich and D. Herschbach, *Enhanced orientation of polar molecules by combined electrostatic and nonresonant induced dipole forces*, J. Chem. Phys. **111** (1999), 6157–6160.
- [85] L. Cai, J. Marango, and B. Friedrich, *Time-dependent alignment and orientation of molecules in combined electrostatic and pulsed nonresonant laser fields*, Phys. Rev. Lett. **86** (2001), 775–778.
- [86] H. Sakai, S. Minemoto, H. Nanjo, H. Tanji, and T. Suzuki, *Controlling the orientation of polar molecules with combined electrostatic and pulsed, nonresonant laser fields*, Phys. Rev. Lett. **90** (2003), 083001.
- [87] R. A. Bartels, T. C. Weinacht, N. Wagner, M. Baertschy, C. H. Greene, M. M. Murnane, and H. C. Kapteyn, *Phase modulation of ultrashort light pulses using molecular rotational wave packets*, Phys. Rev. Lett. **88** (2002), 013903.
- [88] K. F. Lee, D. M. Villeneuve, P. B. Corkum, and E. A. Shapiro, *Phase control of rotational wave packets and quantum information*, Phys. Rev. Lett. **93** (2004), 233601.
- [89] T. Seideman, M. Y. Ivanov, and P. B. Corkum, *Role of electron localization in intense-field molecular ionization*, Phys. Rev. Lett. **75** (1995), 2819–2822.
- [90] T. K. Kjeldsen, C. Z. Bisgaard, L. B. Madsen, and H. Stapelfeldt, *Role of symmetry in strong-field ionization of molecules*, Phys. Rev. A **68** (2003), 063407.

- [91] I. V. Litvinyuk, K. F. Lee, P. W. Dooley, D. M. Rayner, D. M. Villeneuve, and P. B. Corkum, *Alignment-dependent strong field ionization of molecules*, Phys. Rev. Lett. **90** (2003), 233003.
- [92] T. Seideman, *Time-resolved photoelectron angular distributions: Concepts, applications, and directions*, Annu. Rev. Phys. Chem. **53** (2002), 41–65.
- [93] K. Hoshina, K. Yamanouchi, T. Ohshima, Y. Ose, and H. Todokoro, *Alignment of CS<sub>2</sub> in intense nanosecond laser fields probed by pulsed gas electron diffraction*, J. Chem. Phys. **118** (2003), 6211–6221.
- [94] R. Velotta, N. Hay, M. B. Mason, M. Castillejo, and J. P. Marangos, *High-order harmonic generation in aligned molecules*, Phys. Rev. Lett. **87** (2001), 183901.
- [95] B. A. Garetz, J. Matic, and A. S. Myerson, *Polarization switching of crystal structure in the nonphotochemical light-induced nucleation of supersaturated aqueous glycine solutions*, Phys. Rev. Lett. **89** (2002), 175501.
- [96] (D. R. Lide, ed.), *Handbook of Chemistry and Physics*, 85th edition, CRC Press, 2004-2005.
- [97] J. Q. Williams and W. Gordy, *Microwave spectra and molecular constants of tertiary butyl chloride, bromide, and iodide*, J. Chem. Phys. **18** (1950), 994–995.
- [98] *Aldrich Catalogue*, Sigma-Aldrich Chemical Company, 2001.
- [99] *NIST Chemistry WebBook* [webbook.nist.gov/chemistry](http://webbook.nist.gov/chemistry).

- [100] A. Gedanken and M. D. Rowe, *Magnetic circular dichroism spectra of the methyl halides. Resolution of the  $n \rightarrow \sigma^*$  continuum*, Chem. Phys. Lett. **34** (1975), 39–43.
- [101] D. L. Philips, A. B. Myers, and J. J. Valentini, *Investigation of solvation effects on short-time photodissociation dynamics of alkyl iodides*, J. Phys. Chem. **96** (1992), 2039–2044.
- [102] W. J. O. Thomas, J. T. Cox, and W. Gordy, *Millimeter wave spectra and centrifugal stretching constants of the methyl halides*, J. Chem. Phys. **22** (1954), 1718–1722.
- [103] J. E. Freitas, M. El-Sayed, and H. J. Hwang, *The wavelength dependence of the rates of internal energy redistribution during the photodissociation of 3-iodopyridine*, J. Phys. Chem. **99** (1995), 7395–7406.
- [104] A. M. Mirri and W. Caminati, *Quadrupole hyperfine structure in the rotational spectrum of iodobenzene*, Chem. Phys. Lett. **8** (1971), 409–412.
- [105] P. Atkins and J. de Paula, *Atkins' Physical Chemistry*, 7th edition, Oxford University Press, 2002.
- [106] T. Inagusa, M. Fujitake, and M. Hayashi, *Microwave spectrum,  $r_s$  structure, dipole moment, and nuclear quadrupole coupling constant tensor of ethyl iodide*, J. Mol. Spec. **128** (1988), 456–468.
- [107] M. Fujitake and M. Hayashi, *Microwave spectrum of 1-iodopropane: The observation of the forbidden transitions*, J. Mol. Spec. **127** (1988), 112–124.

- [108] P. W. Milonni and J. H. Eberly, *Lasers*, John Wiley & Sons, Inc., 1988.